MAGNETIC ANISOTROPIES AND DAMPING IN MULTILAYERED THIN FILMS

by

ANISH RAI

TIM MEWES, COMMITTEE CHAIR
ADAM J. HAUSER
CLAUDIA C. K. MEWES
ARUNAVA GUPTA
DEAN TOWNSLEY

A DISSERTATION

Submitted in partial fulfillment of the requirements
for the degree of Doctor of Philosophy
in the Department of Physics and Astronomy
in the Graduate School of
The University of Alabama

TUSCALOOSA, ALABAMA

2021

ABSTRACT

Magnetic materials not only create a substantial area for fundamental scientific discovery but also provide the possibility for smaller, faster, cheaper and more energy-efficient technologies. Magnetic anisotropy and damping play crucial roles for the characteristics of perpendicular magnetic recording (PMR), heat assisted magnetic recording (HAMR), read heads of hard disk drives (HDDs), and magnetic tunnel junctions (MTJs). The intrinsic Gilbert damping plays an important role for the dynamic response of magnetic materials. This dissertation discusses the fundamentals of magnetization dynamics and how broadband ferromagnetic resonance (FMR) spectroscopy can be used to probe the dynamics of magnetic thin films and multilayers. In paricular it shows how the effective Gilbert damping can be extracted from frequency dependent data and how this data can be utilized to determine the anisotropies involved in magnetic thin films and multilayers.

In the first study presented in this dissertation, unidirectional anisotropy, relaxation, and interfacial perpendicular magnetic anisotropy (PMA) of CoFeB/MnN exchange bias system are discussed and investigated using the broadband FMR technique. In the second study presented, higher order contribution to PMA and interfacial damping in Co/Ni multilayers are studied. Polar angle dependent measurements reveal a strong fourth-order contribution to the magnetic anisotropy. However, the macropsin model fails to explain the polar angle dependent measurement for canted states. In the third study presented in this dissertation, conductivity-like Gilbert damping at low temperature is discussed for epitaxially grown iron(Fe) on $MgAl_2O_4$(MAO) and MgO substrates. Low temperature FMR studies confirms iron grown on MgO exhibits lower Gilbert damping than iron grown on MAO and suggests that optimal structural or chemical disorder may be useful for cryogenic spintronic applications.

DEDICATION

To

My beloved parents, Nirmala Rai and Anand Rai

My brother, Late Manish Rai

My wife, Sanju Lopchan

My son, Bryan Lopchan Rai

LIST OF ABBREVIATIONS AND SYMBOLS

LLG	Landau-Lifshitz-Gilbert
α	Damping parameter
θ	Polar angle
ϕ	Azimuthal angle
H_{res}	Resonance field
M_{eff}	Effective magnetization
K_i	Anisotropy constants
$\mathcal{N}$	Demagnetizing tensor
FM	Ferromagnetic
AFM	Antiferromagnetic
ΔH_{pp}	Peak to peak linewidth
$\vec{H}_{eff}$	Effective magnetic field
CPW	Coplanar waveguide
ω	Angular frequency
$\chi(\omega)$	Dynamic susceptibility
$\vec{H}_{mod}$	Modulation field
STT	Spin transfer torque
MTJ	Magnetic tunnel junction
HAMR	Heat assisted magnetic recording
VBL	Vertical Bloch wall
DMI	Dzyaloshinskii-Moriya interaction
TEM	Transmission electron microscope
γ	Gyromagnetic ratio

VSM	Vibrating sample magnetometry
PMA	Perpendicular Magnetic Anisotropy
K_4	Fourth-order magnetocrystalline anisotropy
$\gamma^{'}$	Reduced Gyromagnetic ratio
M	Magnetization
M_s	Saturation magnetization
FMR	Ferromagnetic resonance
A	Exchange stiffness constant
K_u	Uniaxial anisotropy energy density
$K_{2,\mathrm{eff}}$	Second order magnetocrystalline anisotropy

ACKNOWLEDGMENTS

I would like to take the opportunity to express my sincere gratitude to my PhD advisor Dr. Tim Mewes for all his support during the past seven years at the University of Alabama. I will forever cherish his mentorship and friendship. I would also like to express my sincere gratitude to Dr. Claudia C. K. Mewes for all the support and guidance. Financial support was provided by the Defense Advanced Research Project Agency (DARPA) program on Topological Excitations in Electronics (TEE) under grant number D18AP00011 and the Department of Physics and Astronomy.

I would like to thank my other committee members, Prof. Adam J. Hauser, Prof. Arunava Gupta, and Prof. Dean Townsley for their valuable inputs during my PhD years. I would also like to appreciate the help and support from collaborators at Carniege Mellon University, Dr. Vincent Sokalski, Dr. Derek Lau, Dr. Marc De Graef, and Dr. Maxwell Li. I am grateful to Dr. Satoru Emori and David A. Smith from Virginia Tech for the collaboration in various projects.

I would also like to appreciate the interesting discussions and support from my colleagues Dr. Behrouz Khodadadi, Dr. Jamileh Beik Mohammadi, Dr. Somalya Paul, Dr. Shuang Wu, Dr. Abhishek Srivastava, Dr. Digesh Raut, Dr. Keshav Sharma, Dr. Arjun Sapkota, Dr. Sujan Budhathoki, Ashok Pokhrel, Bhuwan Nepal, Prabandha Nakarmi, Upama Karki, Kayla Cole-Piepke, and Shambhu KC.

My sincere thanks to Dr. Patrick LeClair, Dr. Dean Townsley and administrative staff, Nancy Lynn, Karen Pekera, and Lisa Brown. Special thanks goes to the technical support provided by the machine shop staff and electronic technicians: Joe Howell, David

Key, Danny Whitcomb and Jason Kuykendall. I would like to thank Dr. Michael Buettner and Johnny Goodwin for all the training on instruments.

CONTENTS

LIST OF TABLES

LIST OF FIGURES

1 INTRODUCTION

"Perserverance is not a long race;
it is many short races one after the other"

-Walter Elliot

Magnetic materials are ubiqutous in technology that we use on a daily basis. They are used as storage medium in hard drives, to read out the information with the hard drive read head, and to design sensors used in cars and cell phones to only name a few examples. The dynamic response of magnetic materials to an excitation is a crucial aspect of many of these applications and devices.

In the following section a short introduction to the magnetization dynamics will be given with a special emphasis on ferromagnetic resonance phenomena. The concept of magnetic anisotropies and the importance of magnetic relaxation is also discussed in this section. This is followed by a detailed description of the experimental technique of broadband ferromagnetic resonance spectroscopy that is used throughout this dissertation.

The last section of this chapter discusses and summarizes the magnetic anisotropy and relaxation studies carried out as part of this dissertation.

1.1 Magnetization dynamics

Magnetization dynamics in ferromagnetic systems investigates the time-dependent motion of the magnetization vector about an effective magnetic field $\vec{H}_{\text{eff}}$ when it is perturbed from its equilibrium state. Within the continuum limit, the dynamics of the

magnetization vector in ferromagnetic systems is described by the Landau-Lifshitz-Gilbert (LLG) equation [1, 2]:

$$\frac{d\vec{M}}{dt} = \gamma\vec{M} \times \vec{H}_{\text{eff}} - \frac{\alpha}{M_{\text{s}}}\left(\vec{M} \times \frac{d\vec{M}}{dt}\right), \tag{1.1}$$

where $\vec{M}$ is the magnetization vector, M_{s} is the saturation magnetization, $\vec{H}_{\text{eff}}$ is the effective magnetic field, γ is the gyromagnetic ratio and α is the Gilbert damping parameter. The effective magnetic field contains all internal and external fields. It typically includes the demagnetization field, the exchange field, the anisotropy field, as well as static and microwave fields. The gyromagnetic ratio can be written as

$$\gamma = \frac{g\mu_{\text{B}}}{\hbar}, \tag{1.2}$$

where g is the Landé g-factor, μ_{B} is Bohr magneton and $\hbar$ is the reduced Planck constant. The first term in Eqn. (1.1) represents the presessional motion. The second term describes the dissipation or damping of the precessional motion. A schematic for the precession of the magnetization vector about the effective field and the damping is shown in Fig. 1.1.

1.1.1 Ferromagnetic Resonance

One of the important and interesting experimental techniques to study the dynamic response of ferromagnetic materials is ferromagnetic resonance (FMR). It has been used to accurately measure magnetic anisotropy, the gyromagnetic ratio γ, and the damping in thin magnetic film structures. FMR spectra are typically measured by driving the magnetization using a homogeneous microwave field of fixed frequency while varying the applied magnetic field. As a consequence the spins of the specimen precesses about the direction of the effective magnetic field $\vec{H}_{\text{eff}}$ at the driving frequency f. The energy absorbed by the specimen from the transverse microwave field is maximized if the frequency of the microwave field is equal to the resonance frequency. FMR was first

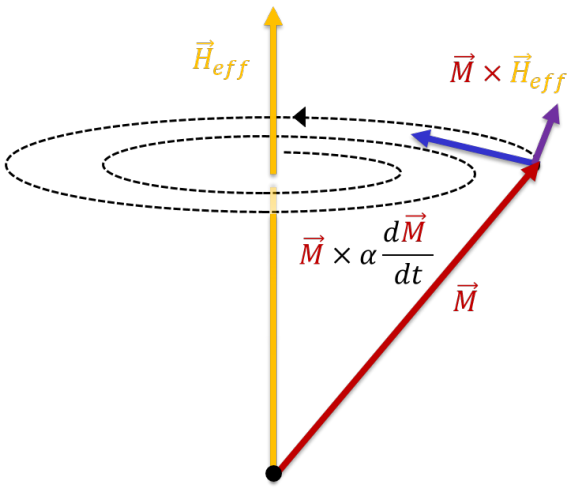

Figure 1.1: Precession of the magnetization vector $\vec{M}$ about the effective magnetic field $\vec{H}_{\text{eff}}$. The first term of the LLG equation is a vector perpendicular to the plane spanned by the magnetization vector and the effective field. It is responsible for the precessional motion. The damping term pulls the magnetization in the direction of the effective field.

observed by Griffiths [3] in 1946. Griffiths observed a resonance frequency different than the Larmor frequency for the electron spin and could not explain the results successfully. The first theoretical explanation of FMR was given by Kittel [4] in 1947.

In the limit that the sample dimensions are small compared to the exchange length [5, 6] the system can be approximately viewed as having a single macrospin moment. The exchange length can be approximated by $\lambda \sim \sqrt{A/K_u}$, where A is the exchange stiffness constant and K_u is the anisotropy constant, assuming a uniaxial symmetry. With this macrospin approximation and neglecting the damping term in Eqn. (1.1), the standard resonance condition can be expressed using the Smit-Beljers relation [7, 8]:

$$\left(\frac{2\pi f}{\gamma}\right)^2 = \frac{1}{M_s^2 \sin^2\theta}\left[\frac{\partial^2 E}{\partial\theta^2}\frac{\partial^2 E}{\partial\phi^2} - \left(\frac{\partial^2 E}{\partial\theta\partial\phi}\right)^2\right], \tag{1.3}$$

where f is the microwave frequency, θ is the polar angle of the magnetization with respect to the film normal, ϕ is the azimuth angle of the magnetization, and E is the magnetic free

energy density. The above equation is evaluated at the equilibrium (θ_0, ϕ_0) of the magnetization for which

$$\left.\frac{\partial E}{\partial \theta}\right|_{\theta_0} = 0, \text{ and } \left.\frac{\partial E}{\partial \phi}\right|_{\phi_0} = 0. \tag{1.4}$$

For high symmetry orientations one can derive analytic solutions, also known as Kittel equations [9]. For cases in which the external magnetic field is applied in the film plane or out of the film plane, the relationship between the microwave frequency f and the resonance field H_{res} at which one observes resonance is respectively given by

$$f = \gamma' \sqrt{(H_{\text{res}})\,(H_{\text{res}} + 4\pi M_{\text{eff}})}, \tag{1.5}$$

$$f = \gamma' (H_{\text{res}} - 4\pi M_{\text{eff}}). \tag{1.6}$$

Here $\gamma' = \gamma/(2\pi)$ is the reduced gyromagnetic ratio and $4\pi M_{\text{eff}}$ is the effective magnetization. When we talk about the FMR signal, we refer to the uniform excitation of the ferromagnetic moments. Eqns. (1.5) and (1.6) assume a uniform precessional motion of all spins in the ferromagnetic sample. However, a microwave field can also excite magnetostatic and exchange spin waves in the ferromagnetic layer [10, 11]. The surfaces of a ferromagnetic layer have different anisotropies compared to the bulk. Therefore, the spins near the surfaces can behave as if they are pinned and not allowed to precess. This situation is illustrated in Fig. 1.2. If the thickness is equal to an integer number of half wavelengths, reflections from both surfaces will produce standing spin waves. As discussed in chapter three, these standing spin waves modes can be used to determine the exchange stiffness A of a magnetic material.

1.1.2 Magnetic Anisotropies

The directional dependence of a material's magnetic moment or magnetization can be best described by magnetic anisotropies. This preferred direction of the magnetization has many applications, for example, magnetic recording heads, magnetic sensors, transformers, and permanent magnets. If the anisotropy originates from the crystal structure of the

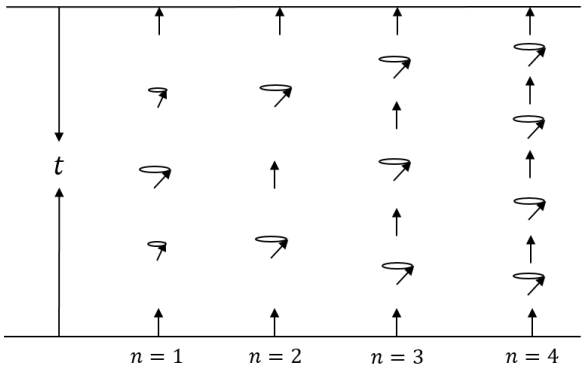

Figure 1.2: Schematic of an exchange-dominated standing spin wave resonance in a magnetic film of thickness t. The spins at the interface are assumed to be pinned, i.e. they are nodes of the precession amplitude at the interface. The lowest order mode ($n = 1$) has a maximum of the precession amplitude at the center of the film and the next higher order mode ($n = 2$) has a node at this location. The higher modes ($n = 3$ and $n = 4$ have) maximum of the precession and a node at the center repsectively.

magnetic material, it is called magneto-crystalline anisotropy. This anisotropy is intrinsic to the magnetic material and is a direct consequence of spin-orbit interactions. The magneto-crystalline anisotropy can be best described by a phenomenological expression, which is a Taylor series expansion of direction cosines of magnetization relative to the crystal axes. For example, the magneto-crystalline anisotropy density for the cubic crystal is

$$E_{\text{aniso}} = K_1 \left(\alpha_1^2\alpha_2^2 + \alpha_2^2\alpha_3^2 + \alpha_3^2\alpha_1^2\right) + K_2 \left(\alpha_1^2\alpha_2^2\alpha_3^2\right) + \ldots, \tag{1.7}$$

where α_1, α_2, α_3 are the direction cosines and K_1 and K_2 are anisotropy constants expressed in erg/cm^3 (cgs) or J/m^3 (SI) of first and second order, respectively. These anisotropy constants are temperature dependent [12] and higher order terms are often ignored.

The other source of magnetic anisotropy comes from the long range magnetic dipolar interaction and is called shape anisotropy. The shape effect of the dipolar interaction in an ellipsoidal ferromagnet can be best described by a demagnetizing field $\vec{H}_{\text{d}}$ which is given by:

$$\vec{H}_{\mathrm{d}} = -\mathcal{N}\vec{M}, \tag{1.8}$$

where $\mathcal{N}$ is the shape dependent demagnetizing tensor. This tensor is a second rank tensor and is expressed by a 3×3 matrix. For an infinitely extended thin film, all the tensor elements are zero except for the direction perpendicular to the film plane ($\mathcal{N}^{\perp} = 1$). This leads to the magnetostatic energy density of the form:

$$E_{\mathrm{d}} = \frac{1}{2}\mu_0 M_{\mathrm{s}}^2 \cos^2\theta, \tag{1.9}$$

where M_{s} is the saturation magnetization, and θ is the angle of the magnetization vector with respect to the film normal. According to this expression, the contribution favours an in-plane orientation of the magnetization. For a uniaxial anisotropy one can write the anisotropy density in the form:

$$E_{\mathrm{aniso}} = \left(\frac{\mu_0 M_s^2}{2} + K_u\right)\cos^2\theta, \tag{1.10}$$

where the first term represents the shape anisotropy and K_u is the unaxial anisotropy.

The broken symmetry at surfaces and interfaces may also induce a uniaxial anisotropy [13]. Therefore the total uniaxial anisotropy of a thin film of thickness t can be written as a sum of volume contribution K_{V} (which could be from shape, magnetocrystalline anisotropy and magnetoelastic energy) and surface contribution K_{S}:

$$K_{\mathrm{eff}} = K_{\mathrm{V}} + \frac{2K_{\mathrm{S}}}{t}. \tag{1.11}$$

The competition between these contributions can create a dependency of the easy axis of magnetization on the film thickness.

Coupling between a ferromagnetic (FM) layer and an antiferromagnetic (AFM) layer in an exchange bias system creates an anisotropy commonly known as exchange bias anisotropy or unidirectional anisotropy [14–16].

1.1.3 Magnetization relaxation

The peak-to-peak FMR linewidth $\Delta H_{\rm pp}$ is an important parameter in measuring the relaxation rate of the magnetization. There are two factors that determine the FMR linewidth. The first one is the Gilbert damping described by the second term of Eqn. (1.1). The second one is the broadening, which corresponds to magnetic inhomogeneities in the ferromagnetic film. According to Suhl [17], the Gilbert damping contribution to the FMR linewidth can be written in the following form

$$\Delta H_{\rm hom} = \frac{1}{\sqrt{3}} \frac{\alpha}{|\partial f/\partial H|} \frac{\gamma'}{M_{\rm s}} \left(\frac{\partial^2 E}{\partial \theta^2} + \frac{1}{sin^2\theta} \frac{\partial^2 E}{\partial \phi^2} \right) \approx \frac{2}{\sqrt{3}} \frac{\alpha}{\gamma'} \frac{f}{cos(\theta - \theta_{\rm H})}. \tag{1.12}$$

If the applied magnetic field is strong enough to allign the magnetization parallel to the external field, then $(\theta - \theta_{\rm H})$ becomes zero. To incorporate the effect of inhomogeneities in the linewidth, a constant term ΔH_0 is added to Eqn. (1.12). The final expression for the FMR linewidth takes the form of

$$\Delta H_{\rm pp} = \Delta H_0 + \frac{2}{\sqrt{3}} \frac{\alpha_{\rm eff}}{\gamma'} f. \tag{1.13}$$

$\alpha_{\rm eff}$ in Eqn. (3.12) contains both intrinsic and extrinsic contributions. The intrinsic contributions are also called Gilbert-like damping. Extrinsic contributions can include eddy-current damping [18, 19], two-magnon scattering [20, 21], spin pumping [22], and radiative damping [19, 23].

1.1.4 Broadband Ferromagnetic Resonance Spectroscopy

When carrying out broadband ferromagnetic resonance spectroscopy a microwave field generated by a microwave source of fixed frequency and fixed power is transmitted through

a coplanar waveguide (CPW). The CPW allows broadband frequency FMR measurements in contrast to using a cavity resonator or shorted waveguide. The schematic of a CPW is shown in Fig. 1.3. The center conductor of width s is separated from the ground planes by a gap w. The center conductor carries a radio frequency current which produces an Oersted field surrounding the conductor. The substrate of thickness h with relative permittivity ϵ_r seperates top and bottom ground planes. A sample is mounted face down, as shown in Fig. 1.3 on the CPW at a height d above the CPW. Fig. 1.4 shows a schematic diagram of the FMR setup.

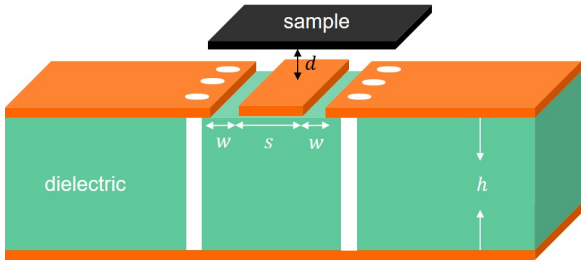

Figure 1.3: Schematic of grounded coplanar waveguide.

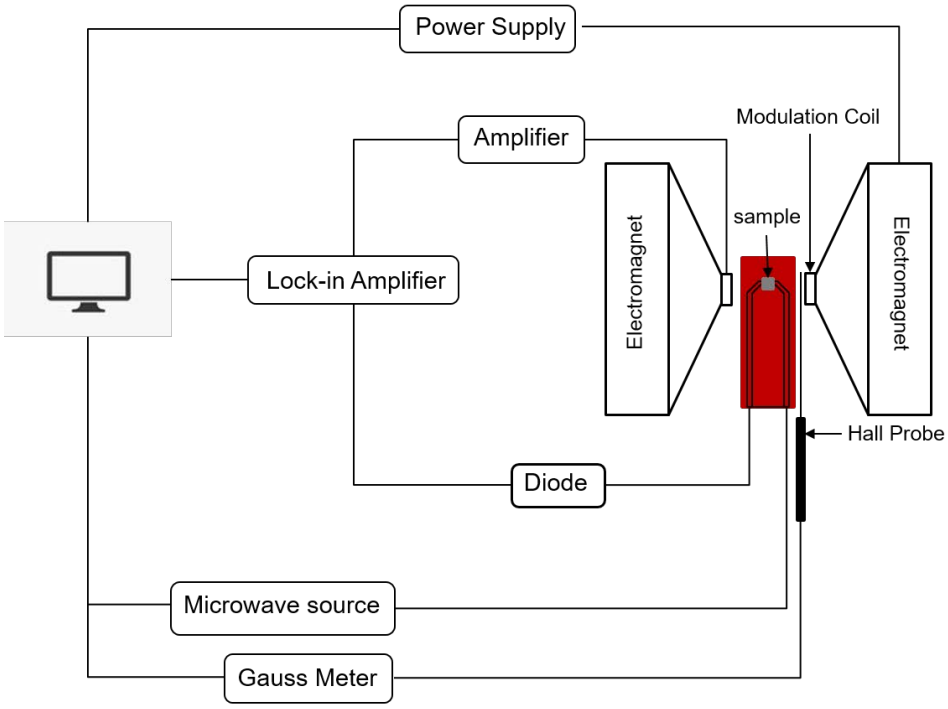

Figure 1.4: Schematic diagram of FMR setup.

A typical FMR spectrum is shown in the Fig. 1.5. The raw data is fitted with the derivative of a Lorentzian using the following expression [24, 25]:

$$y = \frac{a\left(\frac{H_{\rm res}-H}{\Delta H_{\rm pp}}\right) + 9b - 3\left(\frac{H_{\rm res}-H}{\Delta H_{\rm pp}}\right)^2}{\left[\left(\frac{H_{\rm res}-H}{\Delta H_{\rm pp}}\right)^2 + 3\right]^2}, \tag{1.14}$$

where y is the FMR signal, H is the quasi-static applied magnetic field, $H_{\rm res}$ is the resonance field, $\Delta H_{\rm pp}$ is the peak-to-peak linewidth, and a and b are respectively the amplitudes of the absorption and dispersion signals. In order to precisely determine the resonance field the dispersive part of the signal should be added, which is mainly due to conductive and dielectric losses in the measurement.

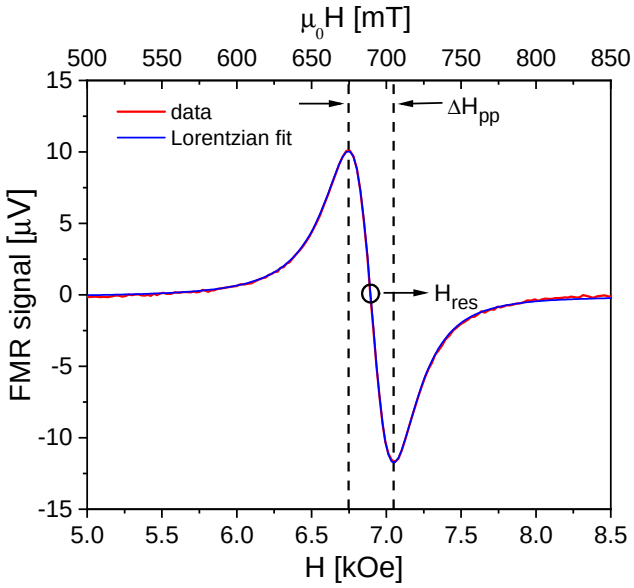

Figure 1.5: A typical FMR spectra measured at 35 GHz.The red line represents the raw data and the blue line represents the fit using Eqn. (1.6).

In dealing with high-frequency measurements one has to consider the dynamic susceptibility:

$$\chi(\omega) = \chi'(\omega) + i\chi''(\omega), \tag{1.15}$$

where $\chi^{'}$ and $\chi^{''}$ are the real and imaginary part of the dynamic susceptibility. The time averaged power P absorbed by the ferromagnetic sample from the spatially homogeneous microwave field of amplitude h_0 and angular frequency ω is proportional to the imaginary part $\chi^{''}(\omega)$ of the high-frequency dynamic susceptibility [26, 27]:

$$P \propto \omega\chi^{''}(\omega, H)h_0^2. \tag{1.16}$$

At the resonance field the precession amplitude and the microwave power absorbed by the sample are at a maximum. Through the different damping mechanisms the energy then dissipates to the lattice, heating the sample. The Schottky-diode detector output voltage V is proportional to the time-averaged power transmitted through the CPW. Therefore it can detect the power absorbed by the sample. In a typical FMR experiment, the frequency of the microwave field is kept constant, and the static magnetic field amplitude H is varied. Therefore, one has to consider the absorbed power as a function of H. The field derivative of the absorbed power dP/dH is proportional to $d\chi^{''}/dH$. The resonance field H_{res} corresponds to the zero crossing of $d\chi^{''}/dH$, and the FMR linewidth ΔH_{pp} is given by the field interval between the extrema of $d\chi^{''}/dH$. In order to detect the small change in transmitted power, a modulation field H_{mod} given by Eqn. (1.17) is added to H:

$$H_{\mathrm{mod}} = \Delta H_{\mathrm{mod}} \sin(2\pi f_{\mathrm{mod}} t). \tag{1.17}$$

This leads to a signal at the detector that is modulated at the modulation frequency f_{mod}. The lock-in amplifier then measures the modulated power. The amplifier responds only to the portion of the input signal that occurs at the modulation frequency. With this set up it is possible to detect and measure small signals [28–31]. The working principle of a lock-in amplifier can be summarized as:

The magnetic field with the influence of modulation takes the following form:

$$H(t) = H_0 + \Delta H_{\mathrm{mod}} \sin(2\pi f_{\mathrm{mod}} t). \tag{1.18}$$

The detector output becomes:

$$V(t) = V(H_0 + \Delta H_{\mathrm{mod}} \sin(2\pi f_{\mathrm{mod}} t)). \tag{1.19}$$

If the modulation amplitude is suitably small, we can approximate the right hand side of Eqn. (1.19) by a Taylor expansion about H_0. The equation becomes

$$V(t) = V(H_0) + \left.\frac{\partial V}{\partial H}\right|_{H=H_0} \Delta H_{\mathrm{mod}} \sin(2\pi f_{\mathrm{mod}} t) + \mathcal{O}({\Delta H_{\mathrm{mod}}}^2). \tag{1.20}$$

A multiplication of $V(t)$ with the reference signal $V_{\mathrm{ref}} = V_0 \sin(2\pi f_{\mathrm{mod}} t + \phi)$ takes place in the lock-in amplifier. Using a low pass filter the output becomes

$$V_{\mathrm{out}} \propto \frac{V_0}{2} \left.\frac{\partial V}{\partial H}\right|_{H=H_0} \Delta H_{\mathrm{mod}} \cos(\phi). \tag{1.21}$$

The output voltage is maximal if ϕ is equal to zero. It is clear that the output voltage also depends on the modulation amplitude. Having a higher modulation amplitude may help to get a better signal strength to some extend. However, one has to be careful as an over-modulated signal does not provide a reliable estimate of ΔH_{pp}. If the modulation field is too large the FMR spectra become broadened and distorted as shown in Fig. 1.6. It is important to employ a modulation amplitude which is much smaller than the intrinsic FMR linewidth, i.e $\Delta H_{\mathrm{mod}} \ll \Delta H_{\mathrm{pp}}$. A practical criterion is to keep $\Delta H_{\mathrm{mod}} \leq \Delta H_{\mathrm{pp}}/5$ [25]. Keeping track of the power of the microwave source is also very important. High microwave power can decrease and distort the FMR signal amplitude [32, 33].

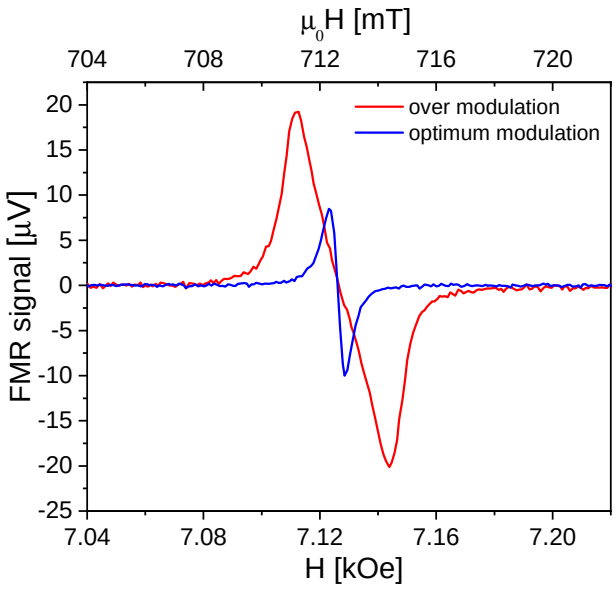

Figure 1.6: FMR spectra at 20 GHz for over and optimum amplitude of modulation fields. The modulation field for the red curve is 13.8 Oe and for the blue curve is 1.0 Oe. The modulation frequency for both cases is 800 GHz.

1.1.5 Magnetic anisotropy and relaxation studies

The study, manipulation, and tuning of the magnetic anisotropy and damping are very crucial in designing magnetic materials to be used in spintronic devices. For example, magnetic thin films showing perpendicular magnetic anisotropy (PMA) and low intrinsic damping are of great importance for applications utilizing the spin transfer torque (STT) effect [34–37]. In this dissertation FMR techniques from low temperature (10K) to room temperature covering a frequency range from 1GHz to 64GHz and from 75GHz to 110GHz, are used to study the magnetic anisotropy and magnetic damping in CoFeB/MnN exchange bias system [22], Co/Ni multilayers [38] and epitaxial iron [39].

In chapter two, exchange bias, unidirectional anisotropy, and magnetic relaxation are discussed for a CoFeB/MnN exchange bias system [22]. Broadband FMR studies reveal an additional uniaxial anisotropy and the magnetic relaxation mechanisms. Thickness dependent measurements indicate that two-magnon scattering is a major source of the relaxation in this multilayer system. However, in addition to an inverse thickness-square

dependence expected for interfacial two-magnon scattering there is another unidirectional relaxation mechanism that scales with the inverse layer thickness of the ferromagnet. Thickness dependent measurements also show the presence of an interfacial perpendicular anisotropy (PMA). This work also hints towards an anisotropic nature of the damping. I have carried out the FMR measurements and the data analysis related to this work. The presented study was done in collaboration with the group of Prof. Markus Meinert, Mareike Dunz, and Philipp Zilske at Bielefed University in Germany. It was aimed at understanding the influence on the magnetization dynamics of MnN as an antiferromagnetic layer coupled to the ferromagnetic layer CoFeB. The motivation for this project came from a previous experiment [40], where a large exchange bias of about 1500 Oe was observed for MnN/CoFe exchange bias system at room temperature. CoFeB is a very popular ferromagnetic material for magnetic tunnel junctions (MTJs) and heat assisted magnetic recording (HAMR).

The need to search for materials to enhance PMA is increasing because of its application in many spintronics devices. It is very challenging as the origin of PMA is still not well understood [41]. In chapter three, higher order contributions to PMA and interfacial damping are discussed in Co/Ni multilayers [38]. The presence of higher-order magnetic anisotropy is of great interest in the field of magnetic random access memory (MRAM) [42]. Data analysis based on the macrospin model and polar angle dependent FMR measurements reveal a strong higher-order contribution to PMA. The systematic deviations of the fit for the canted state suggest that the macrospin model is not sufficient to explain the underlying physics of higher-order contributions. Thickness dependent linewidth measurements show the interfacial contribution to the damping as one would expect for spin pumping. I have carried out the FMR measurements and the data analysis related to it. The present study was part of the Defense Advanced Research Project Agency (DARPA) program on Topological Excitations in Electronics (TEE). Along with the results shown in chapter three, I was also involved in a project that investigted the

limitations of the macrospin model in materials with inhomogeneous perpendicular anisotropy using micromagnetic modelling. [43].

In chapter four, the presence of conductivity-like Gilbert damping at low temperature is discussed for epitaxially grown iron on MgO and $MgAl_2O_4$ (MAO) substrates [39]. To better estimate the Gilbert damping and to rule out contributions from two-magnon scattering W-band FMR was performed in the out-of-plane configuration at room temperature. I have carried out the low temperature and room temperature FMR measurements from 2GHz to 64GHz and from 75GHz to 120GHz. I was also in charge of the data analysis. I have also trained fellow graduate students for measurements and data analysis related to this project. The presented study was done in collaboration with the group of Prof. Satoru Emori at Virginia Tech. It was aimed at understanding the intrinsic damping in pure ferromagnetic materials like iron. In chapter five the supplemental material belonging to the work presented in chapter four and published as a part of reference [39] is presented.

In addition to the work mentioned in this dissertation, I was involved in a number of collaborative projects. In one collaborative research project with the group led by Prof. Satoru Emori from Virginia Tech , we investigated whether the average atomic number or the density of states at the Fermi level is responsible for lowering the damping. The conclusion of this work was that reducing the density of states at the Fermi level is instrumental in reducing damping in these types of materials. Details of the study can be found in reference [44]. In another collaborative project, we investigated the magnetic relaxation in polycrystalline Fe films. Regardless of the microstructure of polycrystalline Fe films with thicknesses ranging from 4 to 25 nm, the Gilbert damping parameter from out-of-plane FMR measurement was ≈ 0.0024. This led to the conclusion that damping in polycrystalline Fe films is a local property and film roughness and grain boundaries have little to no impact on the damping. In-plane FMR measurement suggests a strong two-magnon scattering contribution to the linewidth. Available grain-to-grain two-magnon

scattering models fail to explain the experimental results and suggest that further examination of the influence of the microstructure on extrinsic damping is required. This work has been submitted to Physical Review B and details of the work can be found in reference [45].

In a collaborative work with Prof. Vincent Sokalski, Prof. Marc De Graef, and Prof. Di Xiao from Carnegie Mellon University, we used analytical and micromagnetic calculations to describe a new type of topologically protected magnetic excitation called domain wall skyrmion. We showed that Vertical Bloch Lines (VBL) will transition to DW skyrmions in the presence of Dzyaloshinskii-Moriya interaction (DMI). These topological excitations could open the door to new memory and computing schemes based on topological charge. Details of the study can be found in reference [46]. We also observed the proposed DW skyrmions experimentally in $[Co/Ni]_N$ multilayers using Fresnel-mode Lorentz transmission electron microscopy (TEM). The manuscript has just been accepted in Journal of Applied Physics. In addition, we observed metastable Néel-type skyrmion-arrays in Pt/Co/Ni/Ir multilayers after the *ex situ* application of a large in-plane magnetic field, see reference [47] for details. This offers a means of investigating skyrmions out of equilibrium for future developments of spintronic devices.

In a collaborative work with Prof. Yuping Bao in the department of Chemical and Biological Engineering at the University of Alabama, I used vibrating sample magnetometry (VSM) to characterize iron oxide superparticles with various polymers. Iron oxide superparticles are of great interest in magnetic separation, and targeted drug delivery applications. The details of this work can be found in reference [48].

I have also collaborated with Prof. Adam J. Hauser and his student Dr. Sujan Bhudathoki regarding the investigations of the dynamic properties of epitaxial Heusler $Co_2FeTi_{0.5}Al_{0.5}$ (CFTA) alloy thin films with thicknesses varying from 5 nm to 70 nm grown by sputter beam epitaxy on cubic MgO(100), MAO(100), and Al_2O_3(110) substrates. The manuscript of this work is in the final stage. In a collaborative effort with

Prof. Patrick LeClair and his student Shambhu KC, we investigated the influence of the substrate on the magnetic properties of $Co_{1.5}Ti_{0.5}FeGe$ thin films. The manuscript of this work is also in its final stage.

2 UNIDIRECTIONAL AND UNIAXIAL ANISOTROPIES IN THE MnN/CoFeB EXCHANGE BIAS SYSTEM

Anish Rai,[1] Mareike Dunz,[2] Arjun Sapkota,[1] Philipp Zilske,[2] Jamileh Beik Mohammadi,[3] Markus Meinert,[2] Claudia Mewes,[1] Tim Mewes[1]

[1] *Department of Physics and Astronomy, The University of Alabama, Tuscaloosa, AL 35487, USA*

[2] *Center for Spinelectronic Materials and Devices, Department of Physics, Bielefeld University, 33615 Bielefeld, GER*

[3] *Center for Quantum Phenomena, Department of Physics, New York University, New York City, NY 10003, USA*

We report on broadband and in-plane angle dependent ferromagnetic resonance measurements of MnN (30nm) / CoFeB (t_{CoFeB}) exchange bias bilayer systems with CoFeB thicknesses ranging from 5 to 20 nm. We find that the strong unidirectional anisotropy in this system is accompanied by a strong uniaxial in-plane anisotropy and a small interfacial perpendicular anisotropy ($K_{\perp,\mathrm{i}} = 0.043 \pm 0.001$ erg/cm^2). The strength of the interfacial exchange bias coupling in this system $\Delta\sigma_{\mathrm{eb}} = 0.193 \pm 0.005$ erg/cm^2 is only 2.5 times larger than the interfacial uniaxial coupling strength $\Delta\sigma_{\mathrm{u}} = 0.076 \pm 0.003$ erg/cm^2. The relaxation in this system also shows a strong unidirectional and uniaxial in-plane anisotropy. While the observed thickness dependence of the uniaxial anisotropy of the relaxation is consistent with an interfacial two-magnon scattering contribution, we find that this is not the case for the unidirectional relaxation.

*This chapter is a reformatted reprint of the paper that appeared in J. Magn. Magn. Mater. 485, 374-380 (2019).

2.1 Introduction

Exchange bias systems have been extensively studied since the discovery of the exchange bias effect by Meiklejohn and Bean in 1956 [1] because of the rich physics they offer for fundamental research but also because of their relevance for many technological applications, especially regarding information storage [2–4]. One of the striking characteristics of the exchange bias effect is the shift of the magnetization reversal curve away on the field axis or in other words the presence of a preferred direction of the magnetization, i.e. a unidirectional anisotropy in exchange bias systems. However, the unidirectional anisotropy also affects the magnetization dynamics of exchange bias systems [5–8]. In broadband ferromagnetic resonance experiments a unidirectional anisotropy of the relaxation has recently been observed in exchange biased bilayers [9, 10]. In this paper we utilize broadband ferromagnetic resonance to investigate the magnetic anisotropies of an exchange bias system consisting of CoFeB and the recently discovered antiferromagnet MnN [11]. In addition to broadband ferromagnetic resonance measurements we also use in-plane angle dependent measurements to determine the in-plane anisotropies and relaxation of the system.

2.2 Sample Preparation

Ta(10nm)/MnN(30nm)/CoFeB(t_{CoFeB})/Ta(0.5nm)/Ta_2O_5(2nm) exchange bias stacks were prepared on thermally oxidized silicon wafers via DC magnetron sputtering at room temperature. For this work, we followed the same preparation procedure as previously described in detail in reference [11]. The base pressure of the sputtering system was around 5×10^{-9} mbar prior to the deposition runs. The MnN films were reactively sputtered from an elemental Mn target using a sputtering gas ratio of 50% Ar to 50% N_2 at a working pressure of 2×10^{-3} mbar. The typical deposition rate of MnN was 0.1 nm/s at a source power of 50 W.

After preparation, the samples were post-annealed for 15 min at 600 K and field cooled in a magnetic field of $H_{\mathrm{fc}} = 6.5$ kOe parallel to the film plane in a vacuum furnace

with pressure below 5×10^{-6} mbar to initialize the exchange bias effect in the samples. X-ray diffraction shows that the samples are polycrystalline. A detailed study of identical samples using polarized neutron reflectometry, x-ray absorprion spectroscopy, and x-ray magnetic circular dichroism reveal [12] that while the interface between MnN and CoFeB remains relatively sharp when annealing at 600 K there is significant diffusion. Boron diffuses to the top of the CoFeB, iron and cobalt diffuse deeper into the sample and manganese migrates to the surface.

2.3 Experimental procedures

Broadband ferromagnetic resonance spectroscopy (FMR), which probes the magnetization dynamics, was used to determine the magnetic properties of the samples at room temperature in a frequency range from 2 to 64 GHz. The raw spectroscopy data were analyzed by fitting the derivative of a Lorentzian peak profile to extract the resonance field H_{res} and the peak-to-peak linewidth ΔH [13, 14]. For frequency dependent measurements, the external magnetic field was applied parallel and antiparallel to the exchange bias direction of the sample. In-plane angle dependent measurements were performed at selected frequencies to obtain additional information about in-plane anisotropies.

2.4 Ferromagnetic resonance

Broadband ferromagnetic resonance spectroscopy (FMR), which probes the magnetization dynamics, was used to determine the magnetic properties of the samples at room temperature in a frequency range from 2 to 64 GHz. For frequency dependent measurements, the external magnetic field was applied parallel and antiparallel to the exchange bias direction of the sample. In-plane angle dependent measurements were performed at selected frequencies to obtain additional information about in-plane anisotropies. The magnetization dynamics in ferromagnetic systems can be described by

the Landau-Lifshitz-Gilbert equation [15, 16] given by:

$$\frac{d\vec{M}}{dt} = \gamma\vec{M} \times \vec{H}_{\text{eff}} - \frac{\alpha}{M_{\text{s}}}\left(\vec{M} \times \frac{d\vec{M}}{dt}\right), \tag{2.1}$$

where $\vec{M}$ is the magnetization vector, M_{s} is the saturation magnetization, $\vec{H}_{\text{eff}}$ is the effective magnetic field containing external, anisotropy, microwave and demagnetization fields and γ is the gyromagnetic ratio. The first term on the right hand side in Eqn. (3.1) represents the precessional motion and the second term represents the damping. The gyromagnetic ratio can be written as

$$\gamma = \frac{g\mu_{\text{B}}}{\hbar}, \tag{2.2}$$

where g is the Landé g-factor, μ_{B} is Bohr magneton and $\hbar$ is the reduced Planck constant.

In FMR measurements, the resonance condition can be derived using the Smit-Beljers relation [17, 18]:

$$\left(\frac{f}{\gamma'}\right)^2 = \frac{1}{M_{\text{s}}^2 \sin^2\theta}\left[\frac{\partial^2 E}{\partial\theta^2}\frac{\partial^2 E}{\partial\phi^2} - \left(\frac{\partial^2 E}{\partial\theta\partial\phi}\right)^2\right], \tag{2.3}$$

where $\gamma' = \gamma/2\pi$ is the reduced gyromagnetic ratio, θ is the polar angle of the magnetization with respect to the film normal, ϕ is the azimuth angle of the magnetization, and E is the magnetic free energy density. A detailed description of the geometry can be found in Fig. 2.1. The above equation is evaluated at the equilibrium (θ_0, ϕ_0) of magnetization for which

$$\left.\frac{\partial E}{\partial\theta}\right|_{\theta_0} = 0, \text{ and } \left.\frac{\partial E}{\partial\phi}\right|_{\phi_0} = 0. \tag{2.4}$$

For high symmetry orientations one can derive analytic solutions, also known as Kittel equations [19]. For the cases in which the external magnetic field is applied parallel ($\phi_{\text{H}} = 0°$) and antiparallel ($\phi_{\text{H}} = 180°$) to the exchange bias direction the relationship between the microwave frequency f and the resonance field H_{res} at which one observes resonance is given by [10]:

$$f = \gamma' \sqrt{(H_{\mathrm{res}} + H_{\mathrm{u}} \pm H_{\mathrm{eb}})\,(H_{\mathrm{res}} + H_{\mathrm{u}} \pm H_{\mathrm{eb}} + 4\pi M_{\mathrm{eff}})}, \tag{2.5}$$

where the plus and minus sign are for parallel and antiparallel orientation of the magnetic field with respect to the exchange bias direction respectively, H_{u} is the uniaxial in-plane anisotropy field, H_{eb} is the exchange bias field and $4\pi M_{\mathrm{eff}}$ is the effective magnetization defined by [20, 21]:

$$4\pi M_{\mathrm{eff}} = 4\pi M_{\mathrm{s}} - \frac{2K_{\perp}}{M_{\mathrm{s}}}, \tag{2.6}$$

where $4\pi M_{\mathrm{s}}$ is the demagnetization field and $\frac{2K_{\perp}}{M_{\mathrm{s}}}$ is the perpendicular anisotropy field. They both have the same functional dependence on the orientation of magnetization with respect to the film normal and hence cannot be separated in FMR experiments. In its most general form the perpendicular anisotropy can have a bulk contribution $K_{\perp,V}$ and an interfacial contribution [22]:

$$K_{\perp} = K_{\perp,V} + \frac{K_{\perp,\mathrm{i}}}{t_{\mathrm{CoFeB}}}, \tag{2.7}$$

where the interfacial perpendicular anisotropy $K_{\perp,\mathrm{i}}$ includes contributions from both interfaces of CoFeB.

Using a least squares regression the experimental broadband FMR data can be fitted using the Kittel equation and the values for the gyromagnetic ratio, exchange bias field, uniaxial anisotropy and effective magnetization can be determined.

2.4.1 Magnetic Anisotropies

When carrying out the broadband FMR measurements the magnetic field is applied parallel and antiparallel to the exchange bias direction. As shown exemplarily in Fig. 2.2 for the 20 nm and 7 nm CoFeB films, the broadband FMR data is well described by Eqn. (2.5). For each sample the fit of the experimental data for both the parallel and antiparallel field was done simultaneously, to obtain parameters for the effective magnetization M_{eff}, the reduced gyromagnetic ratio γ', the exchange bias field H_{eb} and the

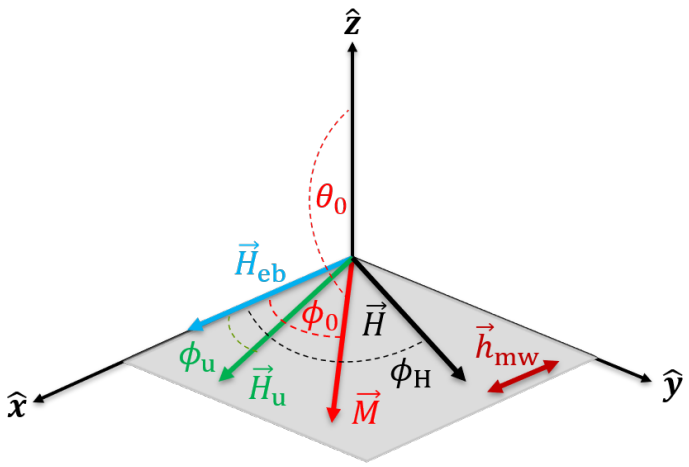

Figure 2.1: Sketch of the measurement geometry, where the reference direction $\hat{x}$ is chosen along the easy direction of the exchange bias field $\vec{H}_{\rm eb}$. The magnetization $\vec{M}$ is shown in its equilibrium orientation (θ_0, ϕ_0). The static magnetic field $\vec{H}$ is applied in the plane of the film and the microwave field $\vec{h}$ is applied perpendicular to $\vec{H}$ also in the film plane. The direction $\phi_{\rm u}$ of the easy axis of the in-plane uniaxial anisotropy $\vec{H}_{\rm u}$ in our model is allowed to deviate from the easy direction of the exchange bias.

uniaxial anisotropy field $H_{\rm u}$ that minimize the sum of the squared residuals.

We find that the reduced gyromagnetic ratio is independent of the film thickness. The average value is $\gamma' = 2.958 \pm 0.001$ GHz/kOe. In Fig. 2.3 the values of the effective magnetization $4\pi M_{\rm eff}$ are shown as a function of the inverse CoFeB film thickness $t_{\rm CoFeB}$. The dependence is clearly linear with a negative slope, indicating the presence of a small interfacial perpendicular anisotropy $K_{\perp,{\rm i}}$ with an out-of plane easy axis. If we ignore the possibility of a bulk contribution to the perpendicular anisotropy, i.e. $K_{\perp,V} = 0$, the intercept at $1/t_{\rm CoFeB} = 0$ corresponds to the saturation magnetization $4\pi M_{\rm s} = 15017 \pm 78$ G. From the slope in this figure we can determine the interfacial perpendicular anisotropy $K_{\perp,{\rm i}} = 0.043 \pm 0.001$ erg/cm^2. This value is almost 50 times smaller than the interfacial perpendicular anisotropy in CoFe/IrMn bilayers [10].

While the fit of the broadband data also provides values for the exchange bias field $H_{\rm eb}$ and the uniaxial anisotropy field $H_{\rm u}$ we note that the accuracy of the extracted values using only two field orientations is limited. In order to determine the symmetry of the

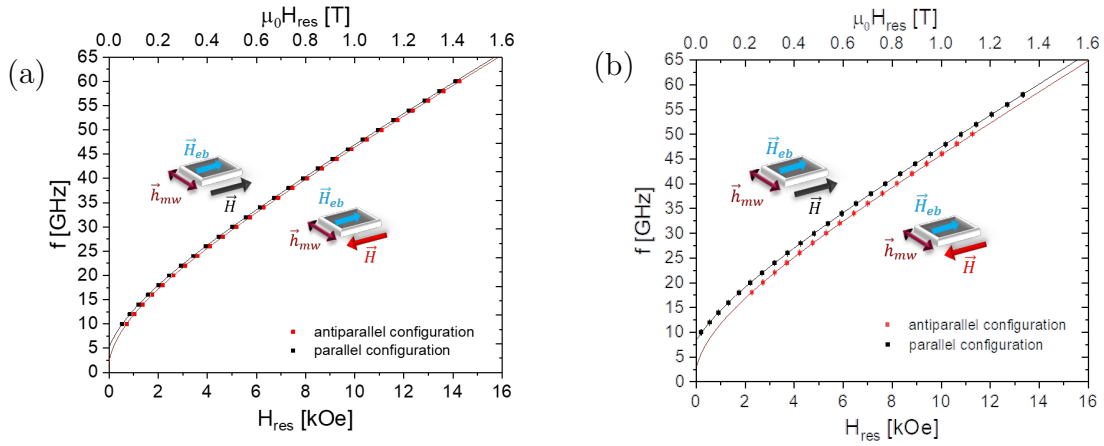

Figure 2.2: Kittel plot of the microwave frequency f as a function of the resonance field H_{res} for an MnN/CoFeB exchange bias bilayer with a CoFeB thickness of (a) $t_{\mathrm{CoFeB}} = 20$ nm and (b) $t_{\mathrm{CoFeB}} = 7$ nm. Black (red) symbols show broadband FMR data with the external magnetic field applied parallel (antiparallel) to the exchange bias direction. The corresponding solid lines are the result of a simultaneous fit of the datasets with parallel and antiparallel field alignment using the Kittel Eqn. (2.5).

anisotropies of the MnN/CoFeB bilayers and to obtain accurate values for these anisotropies we carried out FMR measurements as a function of the in-plane angle ϕ_{H} of the applied field with respect to the exchange bias direction at a fixed frequency of $f = 30$ GHz.

The in-plane angular dependence of the resonance field H_{res} is exemplary shown for samples with a 20 nm and 7 nm CoFeB layer thickness in Fig. 2.4 (a) and (b) respectively. We also show in this figure as a solid line the result of a fit using the full model based on Eqn. (2.3) and minimizing the free energy of the system to obtain the equilibrium orientation of the magnetization. By fitting the full model to the in-plane FMR data, we are able to extract the exchange bias field H_{eb} and the uniaxial anisotropy field H_{u} with high accuracy. In the full model, the angle of the easy axes of uniaxial anisotropy and the easy direction of the unidirectional anisotropy are treated as free parameters to allow for a potential misalignment between those directions. However, we found that the misalignment between the exchange bias direction and the easy axis of the uniaxial anisotropy is small for all samples and does not exceed 2.5°. Both the exchange bias field and the uniaxial

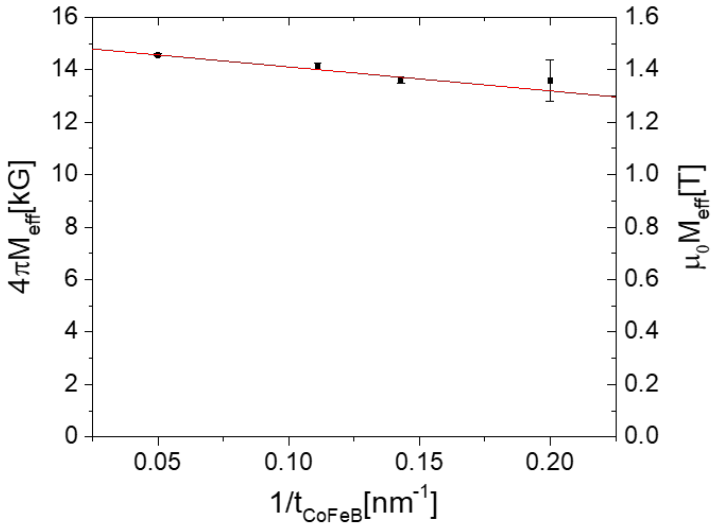

Figure 2.3: The effective magnetization M_{eff} for a MnN/CoFeB(t_{CoFeB}) as a function of the inverse CoFeB film thickness $1/t_{\text{CoFeB}}$. The red line is a linear fit to the experimental data.

anisotropy field depend inversely on the CoFeB layer thickness t_{CoFeB}, as shown in Fig. 2.4. This confirms the well known interfacial origin of the exchange bias effect [2, 8] but also suggests that the in-plane uniaxial anisotropy is interfacial in nature. Similar observations suggesting an interfacial origin of the uniaxial anisotropy in exchange bias bilayers have been previously reported in different exchange bias systems including, for example, NiFe/FeMn [23] and Fe/MnPd [24–26].

Using the saturation magnetization, one can determine the interfacial exchange bias coupling strength, $\Delta\sigma_{\text{eb}} = H_{\text{eb}} M_{\text{s}} t_{\text{CoFeB}}$. We obtain a value of $\Delta\sigma_{\text{eb}} = 0.193 \pm 0.005$ erg/cm^2, which is close to the value reported for perpendicular CoFeB/MnN bilayers [27] but smaller than the coupling found in CoFe/IrMn bilayers [10]. Similarly, the interfacial coupling strength of the uniaxial anisotropy is $\Delta\sigma_{\text{u}} = H_{\text{u}} M_{\text{s}} t_{\text{CoFeB}} = 0.076 \pm 0.003$ erg/cm^2. Thus in this exchange bias system the interfacial unidirectional coupling strength is only 2.5 times larger than the uniaxial interfacial coupling strength.

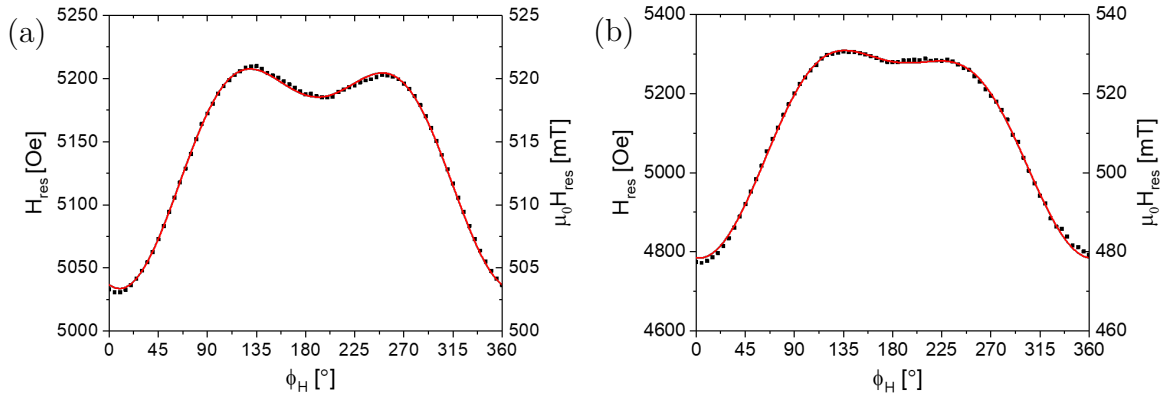

Figure 2.4: Dependence of the resonance field H_{res} on the in-plane angle ϕ_{H} of the applied field measured at a microwave frequency $f = 30\,\mathrm{GHz}$ for an MnN/CoFeB exchange bias bilayer with a CoFeB thickness of (a) $t_{\mathrm{CoFeB}} = 20\,\mathrm{nm}$ and (b) $t_{\mathrm{CoFeB}} = 7\,\mathrm{nm}$. Black symbols represent the experimental data and the red curves are fits based on the full model described by Eqn. (2.3)

2.4.2 Magnetization Relaxation

Information about the magnetization relaxation can be extracted from the linewidth ΔH of the ferromagnetic resonance. The overall peak-to-peak linewidth is the sum of different contributions [18]:

$$\Delta H = \Delta H_0 + \Delta H_{\mathrm{Gilbert}} + \Delta H_{\mathrm{2m}}, \tag{2.8}$$

where ΔH_0 is the inhomogeneous broadening, $\Delta H_{\mathrm{Gilbert}}$ summarizes the contributions from intrinsic and other Gilbert-like damping, including for example spin-pumping [18, 28], and ΔH_{2m} represents contributions from two-magnon scattering [18, 29]. For the Gilbert damping term one can use Suhl's approach [30] and in case the magnetization is aligned with the magnetic field direction, i.e. $\phi_0 = \phi_{\mathrm{H}}$, one finds a linear dependence of the linewidth on the microwave frequency [18, 31–33]:

$$\Delta H_{\mathrm{Gilbert}} = \frac{2}{\sqrt{3}} \frac{\alpha_{\mathrm{eff}}}{\gamma'} f, \tag{2.9}$$

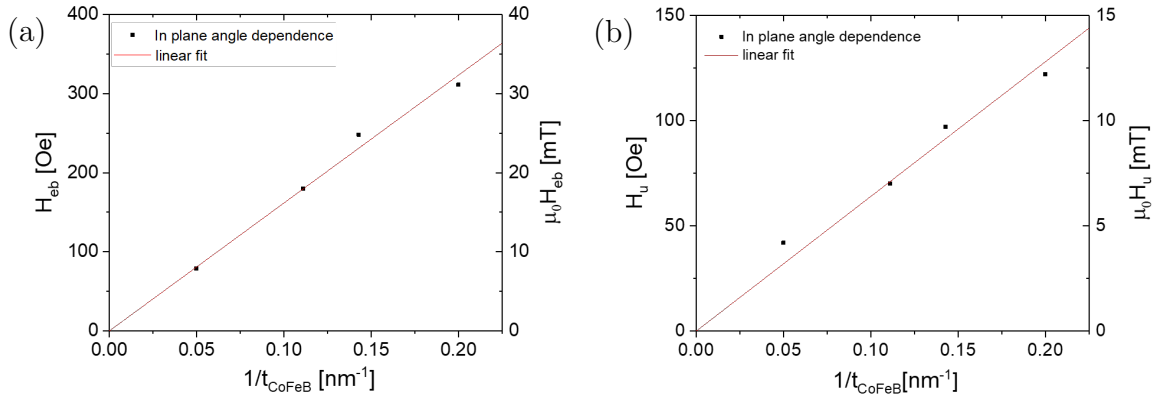

Figure 2.5: (a) Exchange bias field as a function of the inverse CoFeB thickness as extracted from the in-plane angular dependence. The red line is a linear fit to the data, (b) The in-plane uniaxial field as a function of inverse CoFeB thickness as extracted from the in-plane angular dependence. The red line is a linear fit to the data.

where α_{eff} is the effective Gilbert-type damping parameter. The frequency dependence of the linewidth is extracted from the data discussed in the previous section (cp. Fig. 2.2), i.e. from broadband ferromagnetic resonance data with the field applied parallel and antiparallel to the exchange bias direction. In these two orientations the magnetization is aligned with the field direction as long as the field strength exceeds the saturation field, i.e. the assumption that $\phi_0 = \phi_{\text{H}}$ is well justified. The two-magnon contribution to the linewidth is generally expected to be a non-linear function of the microwave frequency, but the details of this non-linear frequency dependence will depend on the model used to describe the interfacial roughness [29, 34, 35]. However, even when a significant two-magnon scattering contribution is present in ferromagnetic materials the frequency dependence of the linewidth is often found to be a linear function of the microwave frequency [10, 36, 37] to a good approximation. This is also the case for the samples investigated here, as can be seen in Fig. 2.6. Therefore, we fit the data using the following linear relationship:

$$\Delta H = \Delta H_0 + \frac{2}{\sqrt{3}} \frac{\alpha_{\text{eff}}}{\gamma'} f. \tag{2.10}$$

In this case, the effective Gilbert damping parameter α_{eff} also includes the approximately linear two-magnon scattering contribution.

As shown in Fig. 2.7, the effective Gilbert damping parameter increases with decreasing film thickness. If this film thickness dependence were caused solely by a strictly interfacial two-magnon scattering contribution, one would expect α_{eff} to scale with the inverse square of the film thickness [8, 9, 38, 39] (straight line as a guide for the eye in Fig. 2.7). While the data in this figure suggests that interfacial two-magnon scattering contributes significantly to the effective damping parameter, it also indicates that this may not be the only contribution. In order to obtain more detailed information about the

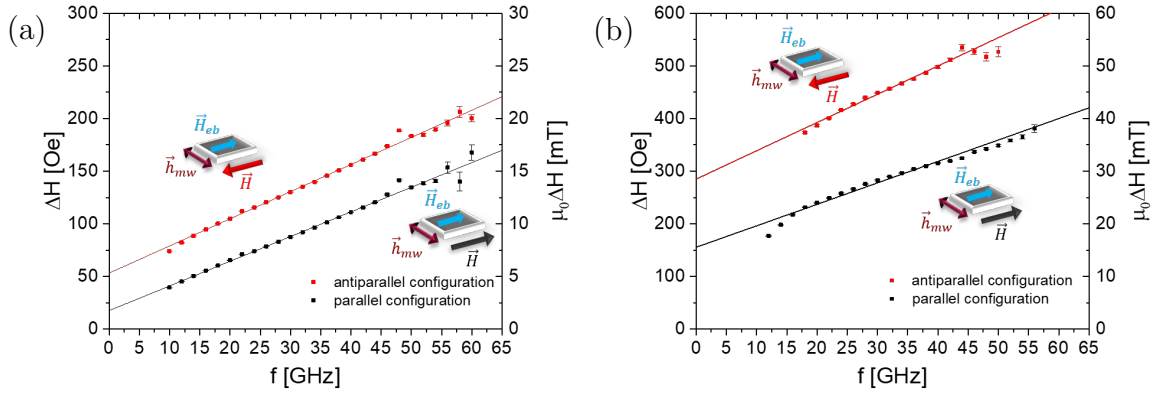

Figure 2.6: FMR linewidth as a function of microwave frequency for a MnN/CoFeB exchange bias bilayer with a CoFeB thickness of (a) $t_{\text{CoFeB}} = 20\,\text{nm}$ and (b) $t_{\text{CoFeB}} = 7\,\text{nm}$. The black (red) symbols represent broadband FMR data with the field applied parallel (antiparallel) to the exchange bias direction. The solid lines represent fits to the experimental data using Eqn. (2.10).

different contributions to the relaxation of the magnetization we have also analyzed the linewidth for the in-plane angle dependent measurements discussed previously (cp. Fig. 2.4). As noted earlier in this exchange biased sample series, the interfacial unidirectional coupling strength is comparable to the interfacial uniaxial coupling strength. As can be seen in Fig. 2.8, the angular dependence of the linewidth also contains a unidirectional and uniaxial anisotropy of comparable strength. The angular dependence of the linewidth can

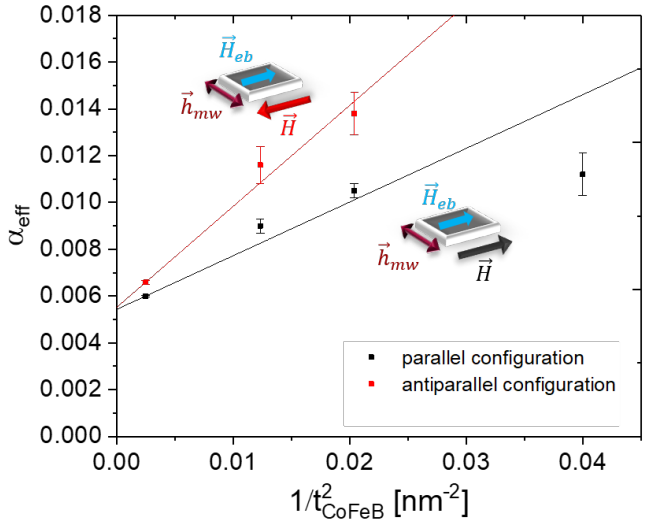

Figure 2.7: Effective Gilbert damping as a function of the square of the inverse CoFeB thickness. The black (red) symbols represent the FMR data measured parallel (antiparallel) to the exchange bias field. The solid lines are guides to the eye.

be described by the following expression:

$$\Delta H\left(\phi_{\mathrm{H}}\right)=\Delta H_{\mathrm{iso}}+\frac{\Delta H_{\mathrm{eb}}}{2}\{1-\cos(\phi_0-\phi_{\mathrm{eb}})\}+\Delta H_{\mathrm{u}}\{1-\cos^2(\phi_0-\phi_{\mathrm{u}})\}, \tag{2.11}$$

where ϕ_{H} is the direction of the magnetic field, ϕ_0 is the direction of the magnetization, ϕ_{eb} and ϕ_{u} are the easy direction of the unidirectional and the easy axis of the uniaxial anisotropies respectively. ΔH_{iso} represents all isotropic contributions to the linewidth. The unidirectional and uniaxial contribution to the linewidth are respectively measured by the parameters ΔH_{eb} and ΔH_{u}. For arbitrary in-plane angles of the applied magnetic field the direction of magnetization will not be perfectly aligned with the field direction, i.e. $\phi_0 \neq \phi_{\mathrm{H}}$. However, by using the fit parameters of the full model used to describe the angular dependence of the resonance field in Fig. 2.4, one can determine ϕ_0 for all angles ϕ_{H} of the applied field. In Fig. 2.8, the angular dependence of the linewidth together with the result of two fits of the data using Eqn. (2.11) are shown. The red curve uses both ΔH_{eb} and ΔH_{u} as fit parameters whereas for the blue curve we constrained the fit to

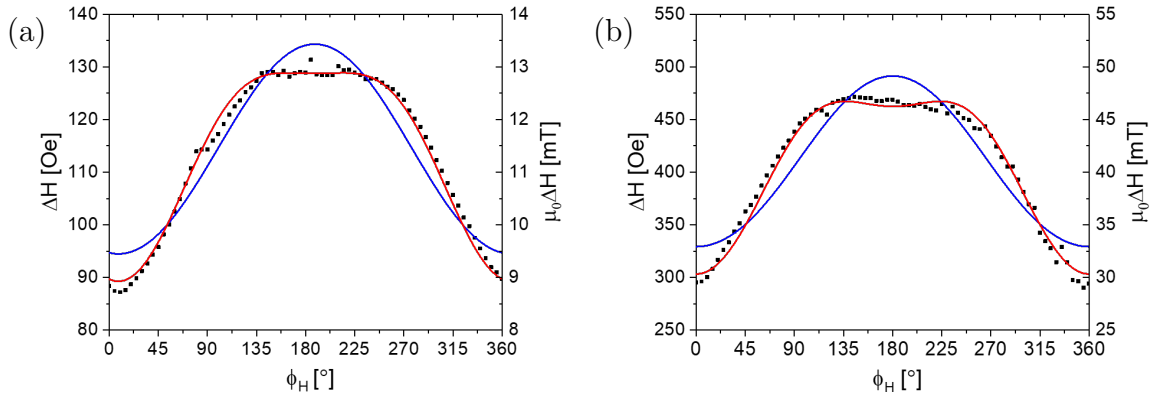

Figure 2.8: Peak-to-peak FMR linewidth ΔH as a function of the in-plane angle of the applied field ϕ_{H} measured at a frequency of $f = 30\,\mathrm{GHz}$ for an MnN/CoFeB exchange bias bilayer with a CoFeB thickness of (a) $t_{\mathrm{CoFeB}} = 20\,\mathrm{nm}$ and (b) $t_{\mathrm{CoFeB}} = 7\,\mathrm{nm}$. Black symbols represent the experimental data, blue curve is the fit assuming only the unidirectional contribution to the relaxation mechanism and red curve is the fit assuming both unidirectional and uniaxial contributions to the relaxation mechanism.

exclude a uniaxial contribution to the linewidth, i.e. $\Delta H_{\mathrm{u}} = 0$. The comparison of the two fits clearly shows that in the MnN/CoFeB exchange bias system a unidirectional anisotropy of the relaxation alone is insufficient to describe the data and an additional uniaxial contribution is clearly required. In this aspect, this exchange bias system differs from the IrMn/CoFe system for which no uniaxial contribution to the relaxation was observed. It is noteworthy that for IrMn/CoFe the interfacial uniaxial coupling strength is much smaller than the interfacial unidirectional coupling strength whereas in the current system, as discussed earlier, they are comparable.

The magnitude of the unidirectional ΔH_{eb} and uniaxial ΔH_{u} contribution to the relaxation mechanism are shown in Fig. 2.9 (a) as a function of the inverse square of the CoFeB thickness. A strictly interfacial two-magnon contribution to the linewidth is expected to scale as $1/t_{\mathrm{CoFeB}}^2$ [8, 9, 38, 39]. Here, the uniaxial linewidth contribution is indeed well described by this dependence whereas the unidirectional contribution is not. As shown in Fig. 2.9 (b) the ratio of the unidirectional and uniaxial linewidth contribution increases approximately linearly with increasing CoFeB film thickness. One notes that the

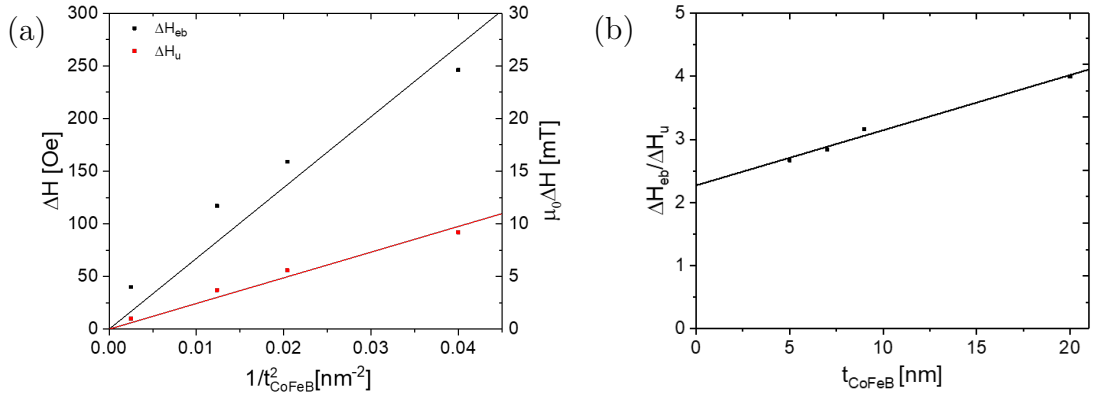

Figure 2.9: (a) Unidirectional linewidth anisotropy ΔH_{eb} (black) and uniaxial linewidth anisotropy ΔH_{u} (red) determined from in-plane-angle dependent FMR measurements as a function of the inverse square of the CoFeB thickness $1/t^2_{\mathrm{CoFeB}}$. (b) Ratio $\Delta H_{\mathrm{eb}}/\Delta H_{\mathrm{u}}$ of the two anisotropic relaxation mechanisms as a function of the CoFeB thickness t_{CoFeB}.

ratio of the anisotropy of the relaxation $\Delta H_{\mathrm{eb}}/\Delta H_{\mathrm{u}}$ in the limit of ultra-thin films is of the same order of magnitude as the ratio of the interfacial unidirectional to the uniaxial coupling strength $\Delta\sigma_{\mathrm{eb}}/\Delta\sigma_{\mathrm{u}} \approx 2.5$. As pointed out for example by Rezende et al. [8], one expects the two-magnon contribution to the linewidth to scale with the square of the local coupling energy e_{local}, i.e. $\Delta H_{\mathrm{eb}} \propto e^2_{\mathrm{eb,local}}$ and $\Delta H_{\mathrm{u}} \propto e^2_{\mathrm{u,local}}$. If the macroscopic coupling energies $\Delta\sigma_{\mathrm{eb}}$ and $\Delta\sigma_{\mathrm{u}}$ would be proportional to their local counterparts, as initial models for exchange bias assumed [1], this would lead to a significantly larger ratio of the linewidth contributions than experimentally observed. Therefore, our observations appear to be more consistent with models of exchange bias that predict that $\Delta\sigma_{\mathrm{eb}} \propto \sqrt{e_{\mathrm{eb,local}}}$, like Malozemoff's random field model [40], Mauri's domain wall model [41] and models derived from these [42]. The linear relationship observed in Fig. 2.9 (b) further suggests the presence of a unidirectional linewidth contribution that scales with $1/t_{\mathrm{CoFeB}}$ as has been previously observed for CoFe/IrMn bilayers [10]. As shown in Fig. 2.10, by including such a term in the model the experimental unidirectional anisotropy of the relaxation ΔH_{eb} is well described for the entire thickness range. For CoFeB thicknesses smaller than about 3 nm the model predicts that interfacial two magnon scattering will be the dominant

unidirectional relaxation mechanism, whereas for thicker films the contribution that scales with $1/t_{\mathrm{CoFeB}}$ dominates. These results therefore provide further evidence for an additional unidirectional relaxation mechanism that does not follow the $1/t^2_{\mathrm{CoFeB}}$ dependence predicted for strictly interfacial two magnon scattering. The possibility of such a contribution has been predicted in [9] and first experimental evidence for its existence was observed for the CoFe/IrMn bilayer system [10] where, in contrast to the current system, two magnon scattering is the dominant unidirectional relaxation mechanism for film thicknesses smaller than 5 nm. Recent polarized neutron reflectometry, x-ray absorption spectroscopy, and x-ray magnetic circular dichroism [12] studies show the importance of interdiffusion in this material system during annealing. This interdiffusion will modify the nature of the interfaces and thereby influence the magnetic properties, including the two magnon scattering. Clearly, more theoretical and experimental work is needed to identify the origin of the unidirectional relaxation mechanism that scales with the inverse of the ferromagnetic film thickness.

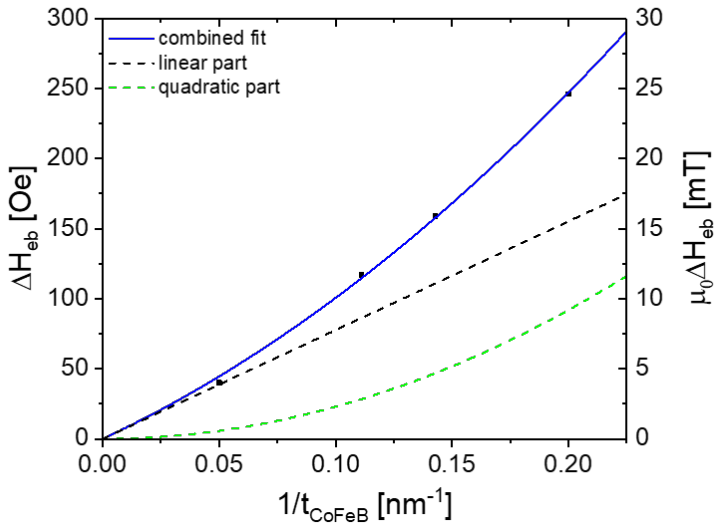

Figure 2.10: Unidirectional linewidth contribution ΔH_{eb}, determined from in-plane angle dependent FMR measurements, plotted as a function of inverse thickness $1/t_{\mathrm{CoFeB}}$. The blue line is a fit using the sum of a $1/t_{\mathrm{CoFeB}}$ contribution (dashed black line) and a $1/t^2_{\mathrm{CoFeB}}$ contribution (dashed green line) to the unidirectional linewidth.

2.5 Summary

Broadband and in-plane angle dependent ferromagnetic resonance experiments on MnN/CoFeB bilayers of different CoFeB thicknesses were carried out. In addition to a strong unidirectional anisotropy, we also found a strong uniaxial in-plane anisotropy and a small perpendicular anisotropy. The interfacial exchange bias coupling strength was 2.5 times larger than the uniaxial coupling strength. Our analysis of the in-plane angular dependence of the linewidth reveals the presence of a unidirectional and uniaxial anisotropy of the relaxation of comparable strength in this bilayer system. Given that the linewidth contribution is expected to scale with the square of the local coupling energies our results are consistent with models for exchange bias that predict a square root dependence of the macroscopic coupling energies on the local coupling energies. In the MnN/CoFeB exchange bias system we observe a contribution to the unidirectional relaxation that scales with $1/t_{\mathrm{CoFeB}}$ instead of the $1/t_{\mathrm{CoFeB}}^2$ dependence expected for a strictly interfacial two-magnon scattering contribution.

2.6 Acknowledgements

M.D. would like to acknowledge support through the MINT Center summer program, C.M., A.S and J.B.M would like to acknowledge support through NSF-CAREER Award No. 1452670.

2.7 References

[1] W. H. Meiklejohn and C. P. Bean, Phys. Rev. **102**, 1413 (1956).

[2] J. Nogués and I. K. Schuller, Journal of Magnetism and Magnetic Materials **192**, 203 (1999).

[3] R. L. Stamps, Journal of Physics D: Applied Physics **33**, R247 (2000).

[4] E. Chen, D. Apalkov, A. Driskill-Smith, A. Khvalkovskiy, D. Lottis, K. Moon, V. Nikitin, A. Ong, X. Tang, S. Watts, et al., IEEE Transactions on Magnetics **48**, 3025 (2012).

[5] J. Scott, Journal of applied physics **57**, 3681 (1985).

[6] R. D. McMichael, M. D. Stiles, P. J. Chen, and W. F. Egelhoff, Journal of Applied Physics **83**, 7037 (1998).

[7] C. Mathieu, M. Bauer, B. Hillebrands, J. Fassbender, G. Güntherodt, R. Jungblut, J. Kohlhepp, and A. Reinders, Journal of Applied Physics **83**, 2863 (1998).

[8] S. M. Rezende, M. A. Lucena, A. Azevedo, F. M. de Aguiar, J. R. Fermin, and S. S. P. Parkin, Journal of Applied Physics **93**, 7717 (2003).

[9] T. Mewes, R. Stamps, H. Lee, E. Edwards, M. Bradford, C. Mewes, Z. Tadisina, and S. Gupta, IEEE Magnetics Letters **1**, 3500204 (2010).

[10] J. B. Mohammadi, J. M. Jones, S. Paul, B. Khodadadi, C. K. Mewes, T. Mewes, and C. Kaiser, Physical Review B **95**, 064414 (2017).

[11] M. Meinert, B. Büker, D. Graulich, and M. Dunz, Phys. Rev. B **92**, 144408 (2015).

[12] P. Quarterman, I. Hallsteinsen, M. Dunz, M. Meinert, E. Arenholz, J. A. Borchers, and A. J. Grutter, Phys. Rev. Materials **3**, 064413 (2019).

[13] C. J. Oates, F. Y. Ogrin, S. L. Lee, P. C. Riedi, G. M. Smith, and T. Thomson, Journal of Applied Physics **91**, 1417 (2002).

[14] Journal of Magnetism and Magnetic Materials **417**, 137 (2016), ISSN 0304-8853.

[15] L. Landau and E. Lifshitz, Phys. Z. Sowjetunion **8**, 101 (1935).

[16] T. L. Gilbert, IEEE Transactions on Magnetics **40**, 3443 (2004).

[17] J. Smit and H. Beljers, Phillips Res. Rep **10**, 113 (1955).

[18] C. K. Mewes and T. Mewes, *Relaxation in magnetic materials for spintronics* (Pan Stanford Publishing Singapore, 2015), pp. 71–96.

[19] P. G. Barreto, M. A. Sousa, F. Pelegrini, W. Alayo, F. J. Litterst, and E. Baggio-Saitovitch, Applied Physics Letters **104**, 202403 (2014).

[20] M. Farle, Reports on Progress in Physics **61**, 755 (1998).

[21] B. Heinrich, in *Ultrathin Magnetic Structures III* (Springer, 2005), pp. 143–210.

[22] J. Beik Mohammadi, G. Mankey, C. K. A. Mewes, and T. Mewes, Journal of Applied Physics **125**, 023901 (2019).

[23] S. Riedling, M. Bauer, C. Mathieu, B. Hillebrands, R. Jungblut, J. Kohlhepp, and A. Reinders, **85**, 6648 (1999).

[24] Y. J. Tang, B. Roos, T. Mewes, S. O. Demokritov, B. Hillebrands, and Y. J. Wang, **75**, 707 (1999).

[25] Y. J. Tang, B. F. P. Roos, T. Mewes, A. R. Frank, M. Rickart, M. Bauer, S. O. Demokritov, B. Hillebrands, X. Zhou, B. Q. Liang, et al., Phys. Rev. B **62**, 8654 (2000).

[26] Y. Tang, B. Roos, T. Mewes, M. Bauer, S. Demokritov, B. Hillebrands, and W. Zhan, Materials Science and Engineering: B **76**, 59 (2000).

[27] P. Zilske, D. Graulich, M. Dunz, and M. Meinert, Applied Physics Letters **110**, 192402 (2017).

[28] Y. Tserkovnyak, A. Brataas, and G. E. Bauer, Physical review letters **88**, 117601 (2002).

[29] R. Arias and D. Mills, Journal of Applied Physics **87**, 5455 (2000).

[30] H. Suhl, Physical Review **97**, 555 (1955).

[31] T. D. Rossing, Journal of Applied Physics **34**, 995 (1963).

[32] B. Heinrich, J. Cochran, and R. Hasegawa, Journal of Applied Physics **57**, 3690 (1985).

[33] Z. Celinski and B. Heinrich, Journal of applied physics **70**, 5935 (1991).

[34] R. Arias and D. L. Mills, Phys. Rev. B **60**, 7395 (1999).

[35] D. Mills and R. Arias, Physica B: Condensed Matter **384**, 147 (2006).

[36] G. Woltersdorf and B. Heinrich, Phys. Rev. B **69**, 184417 (2004).

[37] A. Conca, S. Keller, M. R. Schweizer, E. T. Papaioannou, and B. Hillebrands, Phys. Rev. B **98**, 214439 (2018).

[38] R. D. McMichael, M. D. Stiles, P. Chen, and W. F. Egelhoff Jr, Journal of applied physics **83**, 7037 (1998).

[39] S. Rezende, A. Azevedo, M. Lucena, and F. De Aguiar, Physical Review B **63**, 214418 (2001).

[40] A. P. Malozemoff, Phys. Rev. B **35**, 3679 (1987).

[41] D. Mauri, H. C. Siegmann, P. S. Bagus, and E. Kay, Journal of Applied Physics **62**, 3047 (1987).

[42] F. Radu and H. Zabel, *Exchange Bias Effect of Ferro-/Antiferromagnetic Heterostructures* (Springer Berlin Heidelberg, 2008), pp. 97–184.

3 HIGHER-ORDER PERPENDICULAR MAGNETIC ANISOTROPY AND INTERFACIAL DAMPING IN Co/Ni MULTILAYERS

Anish Rai,[1] Arjun Sapkota,[1] Ashok Pokhrel,[1] Maxwell Li,[2] Marc De Graef,[2] Claudia Mewes,[1] Vincent Sokalski,[2] Tim Mewes[1]

[1]*Department of Physics and Astronomy, The University of Alabama, Tuscaloosa, AL 35487, USA*

[2]*Department of Materials Sciences and Engineering, Carnegie Mellon University, Pittsburgh, Pennsylvania 15213, USA*

We report on the experimental investigation of the perpendicular magnetic anisotropy in Pt/$[Co/Ni]_N$/Ir multilayers. Broadband ferromagnetic resonance (FMR) and polar angle dependent FMR measurements reveal the presence of a strong fourth-order contribution to the perpendicular anisotropy. By numerically solving the Smit-Beljers relation, we are able to fit the polar angle dependence of the resonance field and extract both the second and fourth-order anisotropy constants. While this model provides a qualitative discription for all samples, we note that for samples near or in the easy cone state of the phase diagram systematic deviations emerge in the polar angle dependent data. The exchange stiffness of the multilayers is found to be lower than the weighted average of the exchange stiffness reported for Co and Ni in the literature. We find that the effective Gilbert damping scales with the inverse multilayer thickness, indicating a significant interfacial contribution to the damping process.

*This chapter is a reformatted reprint of the paper that appeared in Phy. Rev. B 102, 174421 (2020).

3.1 Introduction

Magnetic multilayers or thin films showing perpendicular magnetic anisotropy (PMA) and low Gilbert-like damping are of great importance in spintronics and in particular for applications based on the spin transfer torque (STT) effect [1–4]. PMA has been observed in multilayers like Co/Pd [5], Co/Pt [6], Co/Au [7], Co/Ru [8], Co/Ir [9] and Co/Ni[10]. However, Co/Ni multilayers appear to be a particular good choice as they exhibit large and tunable PMA [10, 11], high spin polarization [1] and relatively low intrinsic damping [1, 12–14]. The occurance of higher-order (fourth-order) magnetic anisotropy has been of great interest in the field of magnetic random access memory (MRAM) as it decreases the switching current density using STT [15]. The fourth-order magnetic anisotropy can be induced by spatial fluctuations of magnetic or non-magnetic layers [16]. It can be introduced in PMA systems with relatively weak exchange interaction between moments of the interface and the rest of the film [17]. It is also known that lateral variations of the second-order uniaxial anisotropy can give rise to fourth-order magnetic anisotropy [18]. In this paper, we report the presence of a strong fourth-order magnetic anisotropy in Co/Ni multilayers. In addition to broadband ferromagnetic resonance characterization in the film plane and perpendicular to the film plane we show the limitations of the macrospin model to describe the polar dependence of the resonance field in these films. Those limitations are most notable for samples in or close to the canted phase of the system. In addition, we also discuss the exchange stiffness and effective Gilbert damping in these films.

The Co/Ni system has previously been investigated in references [14, 19] and a significant fourth-order magnetic anisotropy was required to describe the experimental data. However, the physical mechanisms that leads to this anisotropy contribution remain unclear. A common approach used to analyze experimental data is to use a macrospin model. In the current manuscript we show the limitations of the macrospin model to describe the polar dependence of the resonance field in these films. Those limitations are most notable for samples in or close to the canted phase of the system. In addition, we

have carried out broadband ferromagnetic resonance characterization over a wide frequency range both with the external magnetic field applied in the film plane and perpendicular to the film plane. Besides the perpendicular anisotropy the exchange stiffness is another important parameter to predict the properties of materials for example using micromagnetic modeling. The experimental methods available to determine this parameter in thin films are limited. While we are not aware of studies of the exchange stiffness in Co/Ni multilayers earlier studies of $Ni_{1-x}Co_x$ alloys have shown a large variation of both the experimental values and theoretical predictions [20]. The presence of multiple standing spin-wave modes in one of the samples in this study enables us to obtain an estimate for the exchange stiffness in this material, which will provide useful for micromagnetic studies of this system. While the effective Gilbert damping parameter has been determined previously for the Co/Ni multilayer system [11, 19, 21] so far there has been only limited information regarding the origin of the damping in this system. While the increase of damping in thin Co/Ni multilayers has previously been attributed to spin pumping [19] with only three samples investigated in this prior study no detailed quantitative analysis was possible. In this work we show that the effective damping scales inversely with the multilayer thickness, consistent with the interfacial nature of spin pumping. Furthermore, we are able to quantify the spin mixing conductance in this system.

3.2 Experimental procedures

Multi-layers of Si sub./ Ta(3 nm)/ Pt(0.5 nm)/(Co(0.2 nm)/Ni((0.6 nm))$_N$/Ir(0.5 nm)/ Ta(3 nm)/ Pt(3 nm)/ Ir(0.5 nm) were prepared via rf (Ta layers) and dc (Pt, Co, Ni, Ir layers) magnetron sputtering on Si substrates in an Ar atmosphere fixed at 2.5×10^{-3} Torr. All samples had a Ta(3 nm)/Pt(3nm) seed/adhesion layer and were capped with Ta(3 nm)/Pt(3nm)/Ir(0.5nm). Base pressure was maintained at less than 3×10^{-7} Torr. The asymmetric multilayer samples $[Pt/(Co/Ni)_N/Ir]_M$ have shown a strong interfacial Dzyaloshinskii-Moriya interaction (DMI) resulting in conventional 2D skyrmions [22, 23] and domain wall skyrmions [24, 25] while symmetric multilayer $(Co/Ni)_N$ were shown to

have negligible DMI [22]. Based on prior work on samples deposited under the same conditions the interfacial rms roughness is expected to be comparable to the thickness of the individual layers [26].

The dynamic magnetic properties of the samples were determined using broadband ferromagnetic resonance spectroscopy (FMR) at room temperature in the frequency range from 2 to 64 GHz. Our custom built broadband FMR system uses a coplanar waveguide structure with a 420 μm wide central conductor for the microwave excitation for the microwave excitation of the sample and the transmitted power is measured using a zero bias Schottky diode in combination with field modulation and lock-in detection [27, 28].

Broadband frequency dependent FMR measurements were carried out with the external magnetic field applied along the film normal (out-of-plane configuration) and with the field applied in the film plane (in-plane configuration). In order to further investigate the anisotropies of the Co/Ni multilayers FMR measurements at a fixed frequency of 15 GHz were carried out as a function of the polar angle θ_{H} of the applied field with respect to the film normal. For all FMR measurements the field swept spectra were analyzed by fitting the derivative of a Lorentzian peak profile which includes both dispersive and absorptive components to extract the resonance field H_{res} and the peak-to-peak linewidth ΔH [29, 30].

3.3 Ferromagnetic resonance

The magnetization dynamics in ferromagnetic systems can be described by the Landau-Lifshitz-Gilbert equation [31, 32] given by

$$\frac{d\vec{M}}{dt} = \gamma \vec{M} \times \vec{H}_{\mathrm{eff}} - \frac{\alpha}{M_{\mathrm{s}}} \left(\vec{M} \times \frac{d\vec{M}}{dt} \right), \tag{3.1}$$

where $\vec{M}$ is the magnetization vector, M_{s} is the saturation magnetization, $\vec{H}_{\mathrm{eff}}$ is the effective magnetic field containing external, anisotropy, microwave, demagnetization fields, γ is the gyromagnetic ratio and α is the Gilbert damping parameter. The first term of the

above equation represents the presessional motion and the second terms describes the dissipation or damping.

In FMR measurements, the resonance condition can be expressed using the Smit-Beljers relation [33, 34]:

$$\left(\frac{2\pi f}{\gamma}\right)^2 = \frac{1}{M_s^2 \sin^2\theta}\left[\frac{\partial^2 E}{\partial\theta^2}\frac{\partial^2 E}{\partial\phi^2} - \left(\frac{\partial^2 E}{\partial\theta\partial\phi}\right)^2\right], \tag{3.2}$$

where f is the microwave frequency, θ is the polar angle of the magnetization with respect to film normal, ϕ is the azimuth angle of the magnetization, and E is the magnetic free energy density. The above equation is evaluated at the equilibrium (θ_0, ϕ_0) of the magnetization for which

$$\left.\frac{\partial E}{\partial\theta}\right|_{\theta_0} = 0, \text{ and } \left.\frac{\partial E}{\partial\phi}\right|_{\phi_0} = 0 \tag{3.3}$$

In order to accurately describe the dynamic properties of materials having a strong perpendicular anisotropy, the anisotropy energy density E_{aniso} is typically assumed to contain second-order and fourth-order terms in $\cos\theta$ [35, 36].

$$E_{\text{aniso}} = \tilde{K}_{2,\text{eff}} \cos^2\theta + \frac{K_{4,\text{eff}}}{2}\cos^4\theta, \tag{3.4}$$

where $\tilde{K}_{2,\text{eff}}$ is the second-order anisotropy containing both shape and interfacial anisotropy terms and $K_{4,\text{eff}}$ is the fourth-order uniaxial anisotropy. Effective quantities are used to indicate a macrospin representation of the system. Here we use the sign convention for which the film normal is an easy axis of the corresponding anisotropy contributions for negative $K_{\text{i,eff}}(\text{i} = 2, 4)$.

The Kittel equation for in-plane (ip) and out-of-plane (oop) configurations for systems with second- and fourth-order perpendicular anisotropy are given by [37, 38]

$$f^{\text{ip}} = \gamma' \sqrt{H_{\text{res}}\left(H_{\text{res}} + M_{\text{eff}}^{\text{ip}}\right)}, \tag{3.5}$$

$$f^{\mathrm{oop}} = \gamma^{'} \left(H_{\mathrm{res}} - M_{\mathrm{eff}}^{\mathrm{oop}} \right), \tag{3.6}$$

where $\gamma^{'} = \frac{\gamma}{2\pi}$ is the reduced gyromagnetic ratio and the effective magnetizations are given by

$$M_{\mathrm{eff}}^{\mathrm{ip}} = \frac{2\tilde{K}_{2,\mathrm{eff}}}{\mu_0 M_{\mathrm{s}}}, \tag{3.7}$$

$$M_{\mathrm{eff}}^{\mathrm{oop}} = \frac{2\tilde{K}_{2,\mathrm{eff}}}{\mu_0 M_{\mathrm{s}}} + \frac{2K_{4,\mathrm{eff}}}{\mu_0 M_{\mathrm{s}}}. \tag{3.8}$$

We note here that a significant difference of in-plane and out-of-plane effective magnetizations $M_{\mathrm{eff}}^{\mathrm{ip}}$ and $M_{\mathrm{eff}}^{\mathrm{oop}}$ can be seen as a clear indication for the presence of the fourth-order anisotropy term $K_{4,\mathrm{eff}}$.

3.4 Results

3.4.1 Broadband ferromagnetic resonance

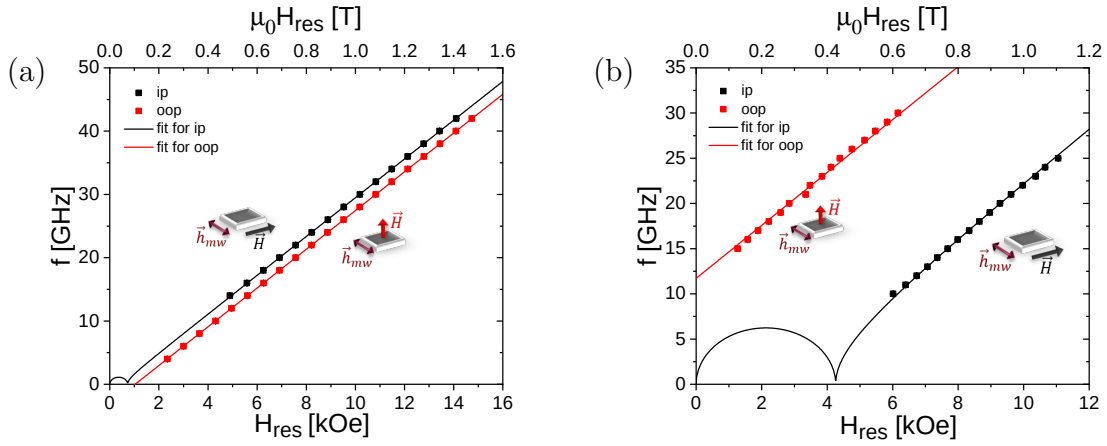

Figure 3.1: Microwave frequency f versus resonance field H_{res} for (a)$[\mathrm{Co/Ni}]_{25}$, (b)$[\mathrm{Co/Ni}]_4$. Red (black) symbols show broadband FMR data with the external magnetic field applied out-of-plane (in-plane) to the sample film. The corresponding solid lines are the result of the fit to the Kittel Eqns. (3.5) and (3.6).

In Fig. 3.1, we have fitted both the in-plane (black symbols) and out-of-plane (red symbols) data simultaneously to obtain a set of fitting parameters that minimizes the sum of the squared residuals. $M_{\mathrm{eff}}^{\mathrm{ip}}$ and $M_{\mathrm{eff}}^{\mathrm{oop}}$ are extracted by fitting the Kittel Eqns. (3.5) and (3.6) simultaneously while sharing the same gyromagnetic ratio. Using these values for the

effective magnetizations and a saturation magnetization of $M_s = 600$ kA/m as determined by VSM the second-order and fourth-order anisotropy constants $\tilde{K}_{2,\text{eff}}$ and $K_{4,\text{eff}}$ are calculated using Eqns. (3.7) and (3.8). We find that in all samples the inclusion of fourth-order anisotropy opposing the second-order ansitropy is needed to obtain a good describtion of the experimental data.

3.4.2 Polar angle dependent ferromagnetic resonance

The broadband ferromagnetic resonance experiments discussed in the previous section strongly suggest the presence of a forth-order anisotropy term. However, these measurements are only carried out along two high symmetry directions of the system, which limits the accuracy with which the anisotropy parameters can be determined. In order to verify the presence of the fourth-order anisotropy and to enable a more precise determination of the anisotropy constants we have carried out ferromagnetic resonance measurements at a fixed frequency of 15 GHz for different polar angles θ_H of the applied field with respect to the film normal. In Fig. 3.2 (a), (b) and (c) the results for measurements of Co/Ni multilayers with 5, 6 and 8 repetitions are shown respectively. Also shown as a solid line is a fit using the full model based on Eqn. (3.2) with both $\tilde{K}_{2,\text{eff}}$ and $K_{4,\text{eff}}$ as free fitting parameters. The iterative fitting procedure determines the values of the free parameters that minimize the sum of squares of the residuals. For this the resonance field at the experimental microwave frequency for a given set of parameters is determined according to Eqn. (3.2). For arbitrary angles there is no analytical expression available for the resonance field. The resonance field can be obtained numerically, by minimizing the free energy expression and evaluating Eqn. (3.2) for all angles of the applied field. This enables calculating the sum of squares of the residuals which is then used by the fitting algorithm to determine the set of parameters for the next iteration. The fit describes the experimental data well for all angles of the applied field and the extracted anisotropy constants agree with those extracted from broadband ferromagnetic resonance measurements (compare table 3.1 in the appendix). In Fig. 3.2 (a), (b), (c) we have also

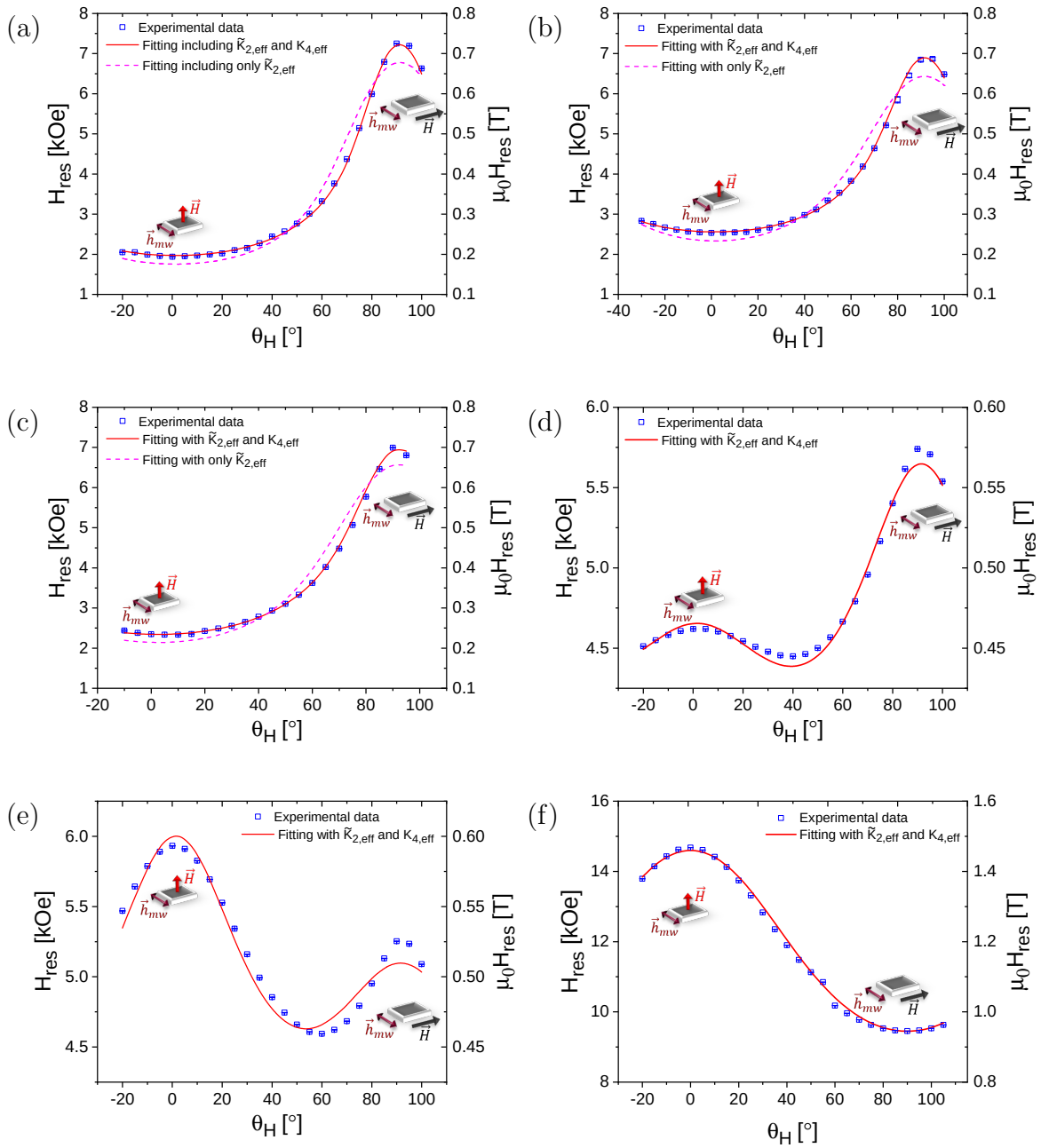

Figure 3.2: Resonance field H_{res} versus polar angle of external magnetic field θ_{H} for (a) $[\text{Co/Ni}]_5$, (b) $[\text{Co/Ni}]_6$, (c) $[\text{Co/Ni}]_8$, (d) $[\text{Co/Ni}]_{12}$, (e) $[\text{Co/Ni}]_{25}$ and (f) $[\text{Co/Ni}]_{100}$. The blue symbols are the polar angle data, dashed magenta line is a constrained fit with $K_{4,\text{eff}} = 0$ and the red line is the fit with both $\tilde{K}_{2,\text{eff}}$ and $K_{4,\text{eff}}$ as free parameters. The polar angle dependent measurements for (a)-(e) were done at 15 GHz whereas for (f) they were done at 34 GHz.

included a constrained fit of the full model for which the fourth-order anisotropy was set to zero, i.e. $K_{4,\mathrm{eff}} = 0$, this is shown as a dashed line. The results clearly show that without the inclusion of fourth-order anisotropy the data is not well described by the macrospin model. The magnitude of the second-order anisotropy decreases with increasing number of repetitions, whereas the magnitude of the fourth-order anisotropy increases. The decrease of the magnitude of $\tilde{K}_{2,\mathrm{eff}}$ with an increase in bilayer repetitions up to 25 could be due to less pronounced effect from the Ta/Pt buffer and/or capping layer but can also be caused by a change in the

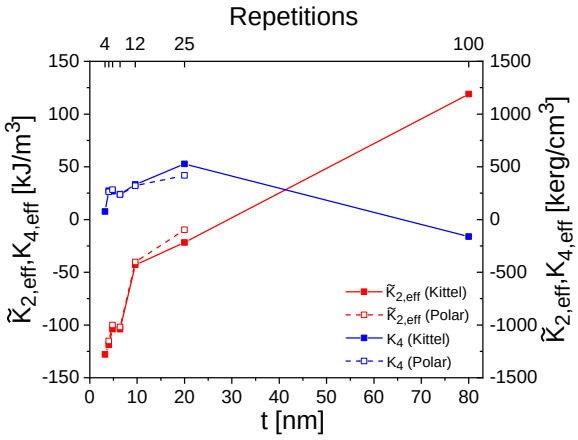

Figure 3.3: Comparision of $\tilde{K}_{2,\mathrm{eff}}$ and $K_{4,\mathrm{eff}}$ obtained from both the Kittel plot and polar angle dependent measurement for all repetitions.

morphology [13, 39–41]. As can be seen in Fig. 3.2 (d) and (e) the competition between the two anisotropies leads to a minimum of the resonance field between in-plane ($\theta_{\mathrm{H}} = 90°$) and out-of-plane ($\theta_{\mathrm{H}} = 0°$) [42, 43] for multilayers with 12 and 25 repetitions. For 12 and 25 repetitions the fit using the model based on Eqn. (3.2) describes the experimental data qualitatively but one notices systematic deviations of the best fit and the data. A quantitative comparision of anisotropies constants is shown in Fig. 3.3. One can see that $\tilde{K}_{2,\mathrm{eff}}$ and $K_{4,\mathrm{eff}}$ are almost of the same order of magnitude for 12 repetitions and $K_{4,\mathrm{eff}}$ is of higher magnitude for 25 repetitions. The data overlayed on the phase diagram (Fig. 3.4) indicate that samples with 8 or less repetitions lie deep inside the region where out-of-plane is the easy direction. The sample with 25 repetitions lies in the region of the easy cone

state, whereas the sample with 12 repetitions is out-of-plane but close to the easy cone phase boundary.

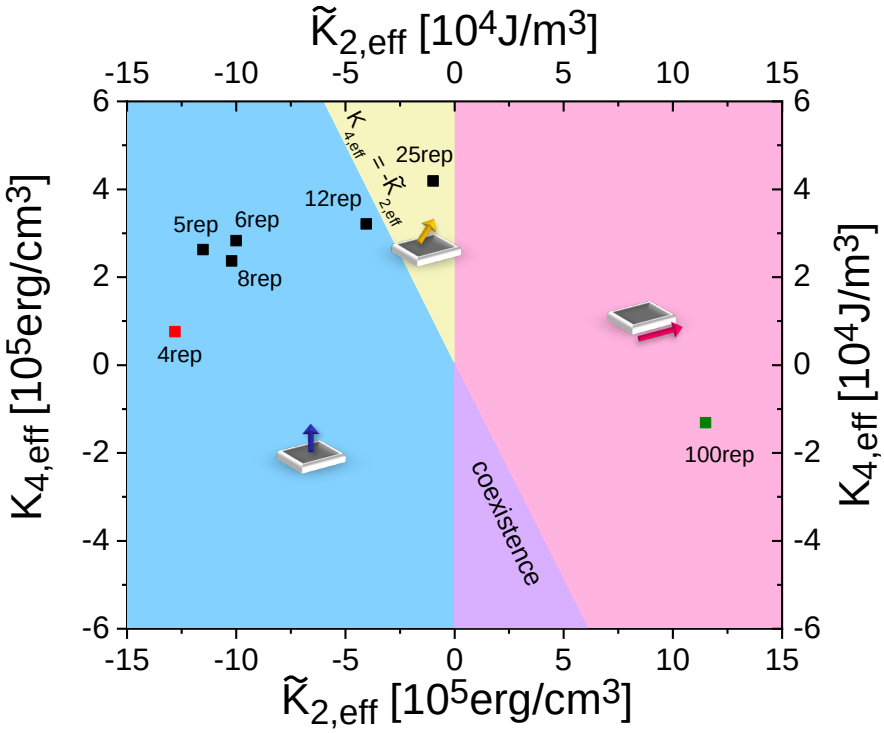

Figure 3.4: Phase diagram of spin orientation as determined by Eq. (3.4). The black squares represent the results from polar angle dependent measurement at 15GHz and the green square represents results from polar angle dependent measurement at 34GHz. The red square represents results from frequency dependent measurements.

For $\tilde{K}_{2,\text{eff}} < 0$ and $K_{4,\text{eff}} > -\tilde{K}_{2,\text{eff}}$ one expects a canted state at zero field defined by the canting angle (θ_c) which can be found my minimizing Eqn. (3.4),

$$cos^2(\theta_c) = \frac{-\tilde{K}_{2,\text{eff}}}{K_{4,\text{eff}}}. \tag{3.9}$$

According to both the fit using the frequency dependent data and the polar angle dependent data this condition is met for the sample with 25 repetitions. It is northworthy to point out that the angle for which the resonance field is minimal (60° for 25 repetitions and 40° for 12 repetitions) is not to be confused with the canting angle ($\theta_c \approx 50°$ for 25 repetitions). Furthermore, the presence of the minimum of the resonance field between

in-plane and out-of-plane does not necessarily indicate that the system will show what is known as the easy cone state, i.e. a canted state at zero field. The reason for this is that the condition for a minimum in the resonance field as described by the Smit-Beljers relation (Eqn. (3.2)) is different from the expression given by Eqn. (3.9) for the easy cone angle. Generally the angle for which the resonance field is minimal can only be calculated numerically, but under the simplifying assumption that the magnetization is aligned with the direction of the applied field one can show the minimum in the resonance field would be located at an angle:

$$\cos^2\theta_{\infty,\mathrm{FMR}} = \frac{3}{8} - \frac{\tilde{K}_{2,\mathrm{eff}}}{4K_{4,\mathrm{eff}}}. \tag{3.10}$$

While this approximation is clearly not valid at finite resonance fields, it still provides a rough estimate for the location of the minimum of the resonance field for 12 repetitions of $\theta_{\infty,\mathrm{FMR}} \approx 34^\circ$ based on the anisotropy values in table 3.1. The 12 repetition sample is a good example showing that a minimum in the resonance field between in-plane and out-of-plane can exist despite the sample not showing an easy cone state. However, one also notices that the fits in Fig. 3.2 (d) and (e) fail to fully describe the angular dependence of the resonance field. While nonlinear fits like this can have difficulties converging, the deviations in this case are not caused by poor convergence but are systematic. One can show this by using the in-plane and out-of-plane resonance fields to determine initial anisotropy values for the fit. These initial anisotropy constants are fully determined by Eqns. (3.5) - (3.8) but fail to capture the angular dependence, as shown for the example of the 25 repetition sample in Fig. 3.2 (e). In particular the initial curve clearly predicts a different location of the minimum in the resonance field than observed experimentally. When trying to reduce the deviations of the fit from the experimental data the fitting algorithm therefore will have to strike a balance between the deviations at all angles, but will never be able to entirely remove these systematic deviations. We therefore conclude that the macrospin model does not fully describe the underlying physics. Similar observations have been made in other Co/Ni multilayers [44]. This is consistent with

models that trace the origin of the fourth-order anisotropy to spatial variations of the second order anisotropy [36].

3.4.3 Exchange stiffness constant

For the $[Co/Ni]_{100}$ sample we observe multiple resonance signals consistent with perpendicular standing spin-wave (PSSW) modes. The ferromagnetic resonance ($n = 0$) signal is located at higher field value, whereas the PSSW modes are located at lower field values as shown in Fig. 3.5. In order to extract the exchange field $\mu_0 H_{ex}$, the resonance fields of higher order PSSW modes $\mu_0 H_{res}(n \neq 0)$ are subtracted from ferromagnetic resonance field $\mu_0 H_{res}(n = 0)$ and plotted as a function of n^2 (see Fig. 3.6). A detailed description of the method, which goes back to the method of Schreiber and Frait [45], can be found in the reference [46]. Using the assumptions of reference [46], the exchange field is given by

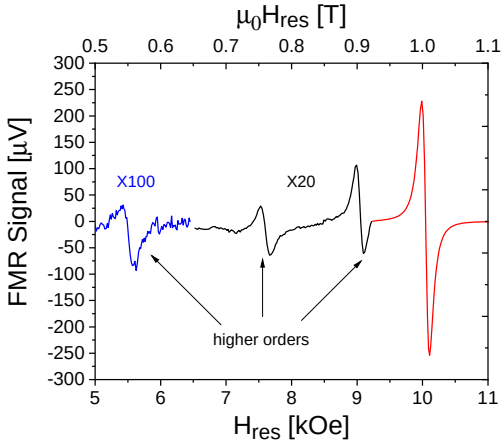

Figure 3.5: Ferromagnetic resonance signal for $[Co/Ni]_{100}$ sample along with higher order PSSW modes.

$$\mu_0 H_{res}(n = 0) - \mu_0 H_{res}(n \neq 0) = \mu_0 H_{ex} = \frac{2A}{M_s} k^2 = \frac{2A}{M_s} \frac{\pi^2}{t^2_{Co/Ni}} n^2, \tag{3.11}$$

where A is the exchange stiffness constant, k is the wave number of the spin wave and n is the order of the standing spinwave modes.

A linear fit based on Eqn. (3.11) is used to extract the exchange stiffness A from the slope. The value of the exchange stiffness constant extracted is

$A = (0.54 \pm 0.01) \times 10^{-11}$J/m which is lower than the weighted average of the exchange stiffness constant for the Co/Ni multilayer $A = (A_{\mathrm{Co}} + 3A_{\mathrm{Ni}})/4$, if one assumes the following values for $A_{\mathrm{Co}} = 1.3 \times 10^{-11}$J/m [47] and $A_{\mathrm{Ni}} = 0.75 \times 10^{-11}$J/m [48]. Further studies are required to determine the exact role the interfacial roughness plays in this regard and to establish the values of the exchange coupling constants in comparable thin films of pure Ni and Co. However, we note that the saturation magnetization of the multilayers is close to the value expected based on the weighted average of the saturation magnetizations of Co [47] and Ni [20]. We note that a significant reduction of exchange stiffness has been previously observed in reference [40] using a different methodology.

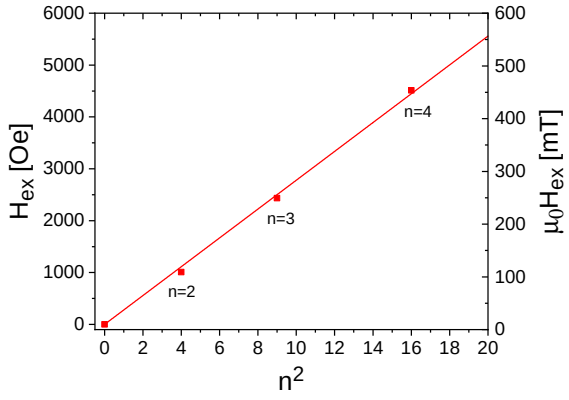

Figure 3.6: Exchange field versus the square of mode number n. The red squares are the data and a black line is a linear fit to the data.

3.5 Damping

The effective Gilbert damping of the Co/Ni multilayers can be determined from the frequency dependence of ferromagnetic resonance linewidth, which contains information about inhomogeneties and magnetization relaxation of the sample. Using Suhl's approach [49] and assuming the magnetization is perfectly alligned with the external magnetic field

and by including a zero frequency offset ΔH_0, characterzing the inhomogeneous broadening, the peak-to-peak linewidth is [33, 50–53]

$$\mu_0 \Delta H = \mu_0 \Delta H_0 + \frac{2}{\sqrt{3}} \frac{\alpha_{\text{eff}}}{\gamma'} f, \tag{3.12}$$

where α_{eff} is the effective Gilbert-type damping parameter. However, In thin films, two-magnon scattering can play a significant role when the magnetic field is applied in the plane of the film [33, 54, 55]. In the following we will therefore rely on the FMR linewidth measured with the magnetic field applied perpendicular to the plane of the film to determine α_{eff} . In the Fig. 3.7, the linewidth for $[\text{Co/Ni}]_{25}$ and $[\text{Co/Ni}]_4$ multilayers are

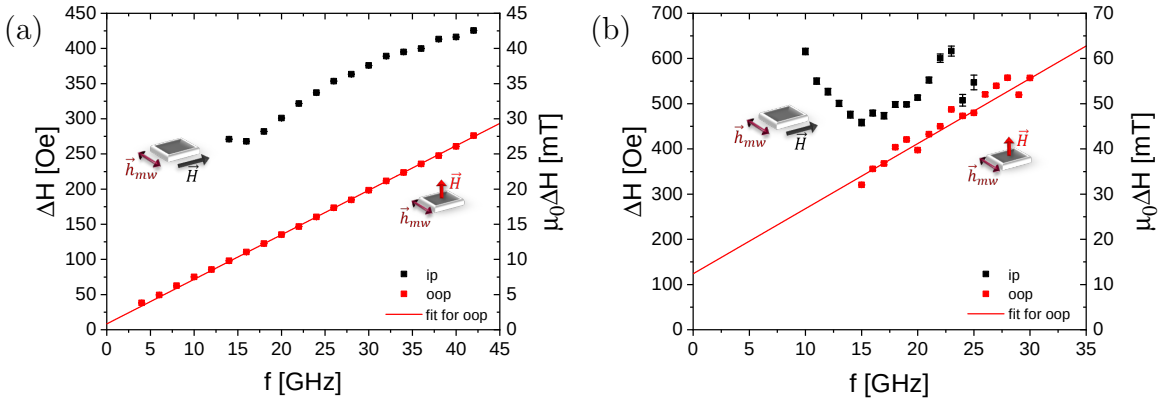

Figure 3.7: Ferromagnetic resonance linewidth ΔH versus the microwave frequency f for (a) $[\text{Co/Ni}]_{25}$ and (b) $[\text{Co/Ni}]_4$. The black (red) symbols represent the data measured with the magnetic field applied in the film plane (perpendicular to the film plane). The solid red line show a fit of the data assuming Eqn. (3.12).

shown. The in-plane measurements of the linewidth are shown for completeness. Both examples in this figure clearly show a non-linear dependence of the linewidth with frequency. The non-linearity for the 25 repetition sample is consistent with a strong two-magnon scattering contribution whereas the increase at low frequencies for the 4 repetition sample likely is caused by the sample not being fully saturated at low fields. The out-of-plane measurement of the linewidth, however, shows a linear dependence and is fitted using Eqn. (3.12) and α_{eff} is determined. The inhomogeneous broadening ΔH_0 (not

shown) measured in the out-of-plane configuration decreases with increasing film thickness.

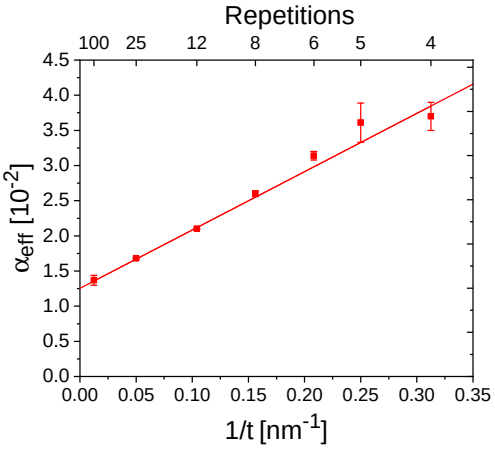

Figure 3.8: Effective Gilbert damping α_{eff} versus the inverse of Co/Ni thickness $t_{\text{Co/Ni}}$ as determined from the ferromagnetic resonance linewidth data measured in the out-of-plane configuration. The red line represents a linear fit.

As shown in the Fig. 3.8, the effective Gilbert damping parameter scales approximately with the inverse ferromagnetic film thickness $t_{\text{Co/Ni}}$, indicating an interfacial contribution to the damping process, as one expects in the case of spin pumping [56]. The slope 0.083 ± 0.004 nm of the fit gives the interfacial Gilbert damping contribution and the y-intercept $\alpha_0 = 0.0125 \pm 0.0003$ gives the bulk Gilbert damping parameter which is close to the value reported for $Ni_{100-x}Co_x$ alloy [57]. One of the important parameters of spin pumping is the spin mixing conductance $g_{\uparrow\downarrow,\text{eff}}$ [56, 58]. With the slope of Fig. 3.8, one can calculate the spin mixing conductance using

$$\alpha_{\text{eff}} = \frac{g_{\uparrow\downarrow,\text{eff}}\hbar\gamma'}{2M_s}\left(\frac{1}{t_{\text{Co/Ni}}}\right) + \alpha_0, \tag{3.13}$$

where $\hbar$ is the reduced Planck constant, α_0 is the bulk Gilbert damping. The calculation using the slope yields $g_{\uparrow\downarrow,\text{eff}} = (3.1 \pm 0.1) \times 10^{19}$ m^{-2}. This value is comparable to the values reported for $Pt/Co_{1-x}Ni_x$ and close to the value reported for Pt/Co [59].

3.6 Summary

Broadband and polar angle dependent ferromagnetic resonance measurements on different repetitions of [Co/Ni] layers were carried out. Both measurements revealed the presence of a strong fourth-order contribution to the perpendicular anisotropy. Fitting the polar angle dependent resonance daBroadband and polar angle dependent ferromagnetic resonance measurements on different repetitions of [Co/Ni] layers were carried out. Both measurements revealed the presence of a strong fourth-order contribution to the perpendicular anisotropy. Fitting the polar angle dependent resonance data using the macrospin model indicates that there are systematic differences between the best fit and the data. This indicates that the macrospin model is not sufficient to explain the polar angle dependence for the samples which are close to or within the easy cone phase. The exchange stiffness for Co/Ni multilayers was calculated to be smaller than the weighted average which could be due to the reduced coupling across the Co/Ni interfaces. The effective Gilbert damping contains a significant interfacial contribution to the damping process that is consistent with spin pumping into the adjacent layers.

3.7 Acknowledgements

A.R. would like to acknowledge support through the Defense Advanced Research Project Agency (DARPA) program on Topological Excitations in Electronics (TEE) under grant number D18AP00011. C.M and A.S would like to acknowledge support through NSF-CAREER Award No. 1452670.

3.8 Appendix:TABLE

Table 3.1: Calculated values of $\tilde{K}_{2,\mathrm{eff}}$ and $K_{4,\mathrm{eff}}$ for different repetitions of [Co/Ni].

Sample	$M_{\mathrm{eff}}^{\mathrm{ip}}$[kA/m]	$M_{\mathrm{eff}}^{\mathrm{oop}}$[kA/m]	$\tilde{K}_{2,\mathrm{eff}}$[kJ/m^3]		$K_{4,\mathrm{eff}}$[kJ/m^3]	
			Kittel	Polar[a]	Kittel	Polar[a]
$[\mathrm{Co/Ni}]_4$	$-(339 \pm 6)$	$-(319 \pm 5)$	$-(128 \pm 2)$		7.5 ± 2.7	
$[\mathrm{Co/Ni}]_5$	$-(317 \pm 4)$	$-(244 \pm 3)$	$-(119 \pm 2)$	-115	27.3 ± 2.3	26.4
$[\mathrm{Co/Ni}]_6$	$-(267 \pm 2)$	$-(196 \pm 2)$	$-(104 \pm 1)$	-100	26.8 ± 1.3	28.3
$[\mathrm{Co/Ni}]_8$	$-(277 \pm 3)$	$-(213 \pm 2)$	$-(104 \pm 1)$	-102	24.1 ± 1.3	23.7
$[\mathrm{Co/Ni}]_{12}$	$-(114 \pm 3)$	$-(26 \pm 2)$	$-(43.0 \pm 1.1)$	-40.3	33.2 ± 1.3	32.0
$[\mathrm{Co/Ni}]_{25}$	$-(58 \pm 1)$	82 ± 1	$-(21.9 \pm 0.4)$	-9.8	52.8 ± 0.9	41.9
$[\mathrm{Co/Ni}]_{100}$	316 ± 5	273 ± 1	119 ± 2	115[b]	16.2 ± 2.1	13.1[b]

[a] Due to the systematic deviations observed for the polar fits the residuals do not follow a normal distribution and therefore no error margins are given.

[b] Polar angle measurement is done at 34 GHz.

3.9 References

[1] S. Mangin, D. Ravelosona, J. Katine, M. Carey, B. Terris, and E. E. Fullerton, Nat. Mater. **5**, 210 (2006).

[2] X. Li, Z. Zhang, Q. Jin, and Y. Liu, Appl. Phys. Lett. **92**, 122502 (2008).

[3] S. Mangin, Y. Henry, D. Ravelosona, J. Katine, and E. E. Fullerton, Appl. Phys. Lett. **94**, 012502 (2009).

[4] W. H. Rippard, A. M. Deac, M. R. Pufall, J. M. Shaw, M. W. Keller, S. E. Russek, G. E. Bauer, and C. Serpico, Phys. Rev. B **81**, 014426 (2010).

[5] P. Carcia, A. Meinhaldt, and A. Suna, Appl. Phys. Lett. **47**, 178 (1985).

[6] P. Carcia, J. Appl. Phys. **63**, 5066 (1988).

[7] F. Den Broeder, D. Kuiper, A. Van de Mosselaer, and W. Hoving, Phys. Rev. Lett. **60**, 2769 (1988).

[8] M. Sakurai, T. Takahata, and I. Moritani, IEEE Transl. J. Magn. Jpn. **7**, 176 (1992).

[9] F. Den Broeder, W. Hoving, and P. Bloemen, J. Magn. Magn. Mater. **93**, 562 (1991).

[10] G. Daalderop, P. Kelly, and F. Den Broeder, Phys. Rev. Lett. **68**, 682 (1992).

[11] J.-M. Beaujour, W. Chen, K. Krycka, C.-C. Kao, J. Sun, and A. Kent, Eur. Phys. J. B **59**, 475 (2007).

[12] S. Girod, M. Gottwald, S. Andrieu, S. Mangin, J. McCord, E. E. Fullerton, J.-M. Beaujour, B. Krishnatreya, and A. Kent, Appl. Phys. Lett. **94**, 262504 (2009).

[13] J. M. Shaw, H. T. Nembach, and T. J. Silva, J. Appl. Phys. **108**, 093922 (2010).

[14] H.-S. Song, K.-D. Lee, J.-W. Sohn, S.-H. Yang, S. S. Parkin, C.-Y. You, and S.-C. Shin, Appl. Phys. Lett. **102**, 102401 (2013).

[15] R. Matsumoto, H. Arai, S. Yuasa, and H. Imamura, Appl. Phys. Express **8**, 063007 (2015).

[16] B. Dieny and A. Vedyayev, EPL **25**, 723 (1994).

[17] J. Z. Sun, Phys. Rev. B **91**, 174429 (2015).

[18] J. B. Mohammadi, K. Cole, T. Mewes, and C. K. A. Mewes, Phys. Rev. B **97**, 014434 (2018).

[19] M. Haertinger, C. Back, S. Yang, S. Parkin, and G. Woltersdorf, J. Phys. D: Appl. Phys. **46**, 175001 (2013).

[20] P. Talagala, P. S. Fodor, D. Haddad, R. Naik, L. Wenger, P. Vaishnava, and V. Naik, Phys. Rev. B **66**, 144426 (2002).

[21] W. Chen, J.-M. Beaujour, G. De Loubens, A. Kent, and J. Sun, Appl. Phys. Lett. **92**, 012507 (2008).

[22] M. Li, D. Lau, M. De Graef, and V. Sokalski, Phys. Rev. Materials **3**, 064409 (2019).

[23] M. Li, A. Rai, A. Pokhrel, A. Sapkota, C. Mewes, T. Mewes, M. D. Graef, and V. Sokalski, Appl. Phys. Lett. **117**, 112403 (2020).

[24] R. Cheng, M. Li, A. Sapkota, A. Rai, A. Pokhrel, T. Mewes, C. Mewes, D. Xiao, M. De Graef, and V. Sokalski, Phys. Rev. B **99**, 184412 (2019).

[25] M. Li, A. Sapkota, A. Rai, A. Pokhrel, T. Mewes, C. Mewes, D. Xiao, M. De Graef, and V. Sokalski, arXiv:2004.07888 (2020).

[26] M. Jaris, D. Lau, V. Sokalski, and H. Schmidt, Journal of Applied Physics **121**, 163903 (2017).

[27] B. Khodadadi, J. B. Mohammadi, C. Mewes, T. Mewes, M. Manno, C. Leighton, and C. W. Miller, Phys. Rev. B **96**, 054436 (2017).

[28] S. Wu, K. Abe, T. Nakano, T. Mewes, C. Mewes, G. Mankey, and T. Suzuki, Phys. Rev. B **99**, 144416 (2019).

[29] C. Oates, F. Ogrin, S. Lee, P. Riedi, G. Smith, and T. Thomson, J. Appl. Phys. **91**, 1417 (2002).

[30] N. Pachauri, B. Khodadadi, M. Althammer, A. V. Singh, B. Loukya, R. Datta, M. Iliev, L. Bezmaternykh, I. Gudim, T. Mewes, et al., J. Appl. Phys. **117**, 233907 (2015).

[31] L. Landau and E. Lifshitz, Phys. Z. Sowjetunion **8**, 101 (1935).

[32] T. L. Gilbert, IEEE Trans. Magn. **40**, 3443 (2004).

[33] C. K. Mewes and T. Mewes, *Relaxation in magnetic materials for spintronics* (Pan Stanford Publishing Singapore, 2015), pp. 71–96.

[34] J. Smit and H. Beljers, Phillips Res. Rep. **10**, 113 (1955).

[35] M. Farle, B. Mirwald-Schulz, A. Anisimov, W. Platow, and K. Baberschke, Phys. Rev. B **55**, 3708 (1997).

[36] J. Mohammadi, K. Cole, T. Mewes, and C. Mewes, Phys. Rev. B **97**, 014434 (2018).

[37] J. M. Shaw, H. T. Nembach, and T. J. Silva, Phys. Rev. B **87**, 054416 (2013).

[38] Z. Tadisina, A. Natarajarathinam, B. Clark, A. Highsmith, T. Mewes, S. Gupta, E. Chen, and S. Wang, J. Appl. Phys. **107**, 09C703 (2010).

[39] P. Bruno, J. Appl. Phys. **64**, 3153 (1988).

[40] O. Posth, C. Hassel, M. Spasova, G. Dumpich, J. Lindner, and S. Mangin, Journal of Applied Physics **106**, 023919 (2009).

[41] S. Fukami, T. Suzuki, H. Tanigawa, N. Ohshima, and N. Ishiwata, Appl. Phys. Express **3**, 113002 (2010).

[42] Y. Millev and J. Kirschner, Phys. Rev. B **54**, 4137 (1996).

[43] J. M. Shaw, H. T. Nembach, M. Weiler, T. J. Silva, M. Schoen, J. Z. Sun, and D. C. Worledge, IEEE Magn. Lett. **6**, 1 (2015).

[44] A. Sapkota, A. Rai, A. Pokhrel, J. Beik Mohammadi, M. Li, D. Lau, M. De Graef, , V. Sokalski, T. Mewes, et al., J. Appl. Phys **128**, 073910 (2020).

[45] F. Schreiber and Z. Frait, Phys. Rev. B **54**, 6473 (1996).

[46] S. Klingler, A. V. Chumak, T. Mewes, B. Khodadadi, C. Mewes, C. Dubs, O. Surzhenko, B. Hillebrands, and A. Conca, J. Phys. D: Appl. Phys. **48**, 015001 (2014).

[47] P. Tannenwald and R. Weber, Phys. Rev. **121**, 715 (1961).

[48] D. H. Martin, *Magnetism in solids* (MIT Press Cambridge, 1967).

[49] H. Suhl, Phys. Rev. **97**, 555 (1955).

[50] B. Heinrich, J. Cochran, and R. Hasegawa, J. Appl. Phys. **57**, 3690 (1985).

[51] Z. Celinski and B. Heinrich, J. Appl. Phys. **70**, 5935 (1991).

[52] Y. V. Goryunov, N. Garif'yanov, G. Khaliullin, I. Garifullin, L. Tagirov, F. Schreiber, T. Mühge, and H. Zabel, Phys. Rev. B **52**, 13450 (1995).

[53] T. D. Rossing, J. Appl. Phys. **34**, 995 (1963).

[54] R. Arias and D. Mills, J. Appl. Phys. **87**, 5455 (2000).

[55] A. Rai, M. Dunz, A. Sapkota, P. Zilske, J. B. Mohammadi, M. Meinert, C. Mewes, and T. Mewes, J. Magn. Magn. Mater. **485**, 374 (2019).

[56] Y. Tserkovnyak, A. Brataas, and G. E. W. Bauer, Phys. Rev. Lett. **88**, 117601 (2002).

[57] N. Inaba, H. Asanuma, S. Igarashi, S. Mori, F. Kirino, K. Koike, and H. Morita, IEEE T. Magn. **42**, 2372 (2006).

[58] Y. Tserkovnyak, A. Brataas, and G. E. W. Bauer, Phys. Rev. B **66**, 224403 (2002).

[59] W. Zhang, W. Han, X. Jiang, S.-H. Yang, and S. S. Parkin, Nat. Phys. **11**, 496 (2015).

4 CONDUCTIVITY-LIKE GILBERT DAMPING DUE TO INTRABAND SCATTERING IN EPITAXIAL IRON

Behrouz Khodadadi,[1] Anish Rai,[2] Arjun Sapkota,[2] Abhishek Srivastava,[2] Bhuwan Nepal,[2] Youngmin Lim,[1] David A. Smith,[1] Claudia Mewes,[2] Sujan Budhathoki ,[2] Adam J. Hauser,[2] Min Gao,[3] Jie-Fang Li,[3] Dwight D. Viehland,[3] Zijian Jiang,[1] Jean J. Heremans,[1] Prasanna V. Balachandran,[4,5] Tim Mewes, [2] and Satoru Emori, [1]

[1]*Department of Physics, Virginia Tech, Blacksburg, VA 24061, USA*

[2]*Department of Physics and Astronomy, The University of Alabama, Tuscaloosa, AL 35487, USA*

[3]*Department of Material Science and Engineering, Virginia Tech, Blacksburg, VA 24061, USA*

[4]*Department of Material Science and Engineering, University of Virginia, Charlottesville, VA 22904, USA*

[5]*Department of Mechanical and Aerospace Engineering, University of Virginia, Charlottesville, VA 22904, USA*

Confirming the origin of Gilbert damping by experiment has remained a challenge for many decades, even for simple ferromagnetic metals. Here, we experimentally identify Gilbert damping that increases with decreasing electronic scattering in epitaxial thin films of pure Fe. This observation of conductivitylike damping, which cannot be accounted for by classical eddy-current loss, is in excellent quantitative agreement with theoretical predictions of Gilbert damping due to intraband scattering. Our results resolve the

*This chapter is a reformatted reprint of the paper that appeared in Phys. Rev. Lett. 124, 157201 (2020).

long-standing question about a fundamental damping mechanism and offer hints for engineering lowloss magnetic metals for cryogenic spintronics and quantum devices.

4.1 Introduction

Damping determines how fast the magnetization relaxes toward the effective magnetic field and plays a central role in many aspects of magnetization dynamics [1, 2]. The magnitude of viscous Gilbert damping governs the threshold current for spin-torque magnetic switching and auto-oscillations [3, 4], mobility of magnetic domain walls [5, 6], and decay lengths of diffusive spin waves and superfluid like spin currents [7, 8]. To enable spintronic technologies with low power dissipation, there is currently much interest in minimizing Gilbert damping in thin films of magnetic materials [9–19], especially ferromagnetic metals [20–32] that are compatible with conventional device fabrication schemes. Despite the fundamental and technological importance of Gilbert damping, its physical mechanisms in various magnetic materials have yet to be confirmed by experiment.

Gilbert damping is generally attributed to spin-orbit coupling that ultimately dissipates the energy of the magnetic system to the lattice [1, 2]. Kambersky's torque correlation model [33] qualitatively captures the temperature dependence of damping in some experiments [34–37] by partitioning Gilbert damping into two mechanisms due to spin-orbit coupling, namely interband and intraband scattering mechanisms, each with a distinct dependence on the electronic momentum scattering time τ_e. For the interband scattering mechanism where magnetization dynamics can excite electron-hole pairs across different bands, the resulting Gilbert damping is "resistivitylike" as its magnitude scales with τ_e^{-1}; i.e., increased electronic scattering results in higher damping [38, 39]. By contrast, the intraband scattering mechanism is typically understood through the breathing Fermi surface model [40], where electron-hole pairs are excited in the same band, yielding "conductivitylike" Gilbert damping that scales with τ_e; i.e., reduced electronic scattering results in higher damping.

Conductivitylike Gilbert damping was reported experimentally more than 40 years ago in bulk crystals of pure Ni and Co at low temperatures, but surprisingly not in pure Fe [34]. The apparent absence of conductivitylike damping in Fe has been at odds with many theoretical predictions that intraband scattering should dominate at low temperatures [41–47], although some theoretical studies have suggested that intraband scattering may be absent altogether in pure metals [48, 49]. To date, no experimental work has conclusively addressed the role of intraband scattering in pure Fe [50]. There thus remains a significant gap in the fundamental understanding of damping in one of the simplest ferromagnetic metals. Intrinsic conductivitylike Gilbert damping in Fe is also technologically relevant, since minimizing damping in ferromagnetic metals at low temperatures is crucial for cryogenic superconducting spintronic memories [51, 52] and quantum information transduction schemes [53, 54].

In this Letter, we experimentally demonstrate the presence of conductivitylike Gilbert damping due to intraband scattering in epitaxial thin films of body-centered-cubic (bcc) Fe. By combining broadband ferromagnetic resonance (FMR) measurements with characterization of structural and transport properties of these model-system thin films, we show that conductivitylike Gilbert damping dominates at low temperatures in epitaxial Fe. These experimental results agree remarkably well with the magnitude of Gilbert damping derived from first-principles calculations [41, 42, 45], thereby providing evidence for intraband scattering as a key mechanism for Gilbert damping in pure bcc Fe. Our experiment thus resolves the longstanding question regarding the origin of damping in the prototypical ferromagnetic metal. Our results also confirm that—somewhat counterintuitively—disorder can partially suppress intrinsic damping at low temperatures in ferromagnetic metals, such that optimally disordered films may be well suited for cryogenic spintronic and quantum applications [51–54].

4.2 Results and Discussion

Epitaxial bcc Fe thin films were sputter deposited on (001)-oriented $MgAl_2O_4$ (MAO) and MgO single crystal substrates. The choices of substrates were inspired by the recent experiment by Lee et al. [27], where epitaxial growth is enabled with the [100] axis of a bcc Fe-rich alloy oriented 45° with respect to the [100] axis of MAO or MgO. MAO with a lattice parameter of $a_{\mathrm{MAO}}/2\sqrt{2} = 0.2858$ nm exhibits a lattice mismatch of less than 0.4% with Fe ($a_{\mathrm{Fe}} \approx 0.287$ nm), whereas the lattice mismatch between MgO ($a_{\mathrm{MgO}}/2\sqrt{2} = 0.2978$ nm) and Fe is of the order 4%. Here, we focus on 25-nm-thick Fe films that were grown simultaneously on MAO and MgO by confocal dc magnetron sputtering [55]. In the Supplemental Material [55], we report on additional films deposited by off-axis magnetron sputtering.

We verified the crystalline quality of the epitaxial Fe films by x-ray diffraction, as shown in Figs. 4.1(a)–(c). Only (00X)-type peaks of the substrate and film are found in each $2\theta - \omega$ scan, consistent with the single-phase epitaxial growth of the Fe films. The $2\theta - \omega$ scans reveal a larger amplitude of film peak for MAO/Fe, suggesting higher crystalline quality than that of MgO/Fe. Pronounced Laue oscillations, indicative of atomically smooth film interfaces, are observed around the film peak of MAO/Fe, whereas they are absent for MgO/Fe. The high crystalline quality of MAO/Fe is also evidenced by its narrow film peak rocking curve with a FWHM of only 0.02°, comparable to the rocking curve FWHM of the substrate. (The angular resolution of the diffractometer is 0.0068°.) By contrast, the film-peak rocking curve of MgO/Fe has a FWHM of 1°, which indicates substantial mosaic spread in the film due to the large lattice mismatch with the MgO substrate.

Results of $2\theta - \omega$ scans for different film thicknesses [55] suggest that the 25-nm-thick Fe film may be coherently strained to the MAO substrate, consistent with the smooth interfaces and minimal mosaic spread of MAO/Fe. By contrast, it is likely that 25-nm-thick Fe on MgO is relaxed to accommodate the large film-substrate lattice

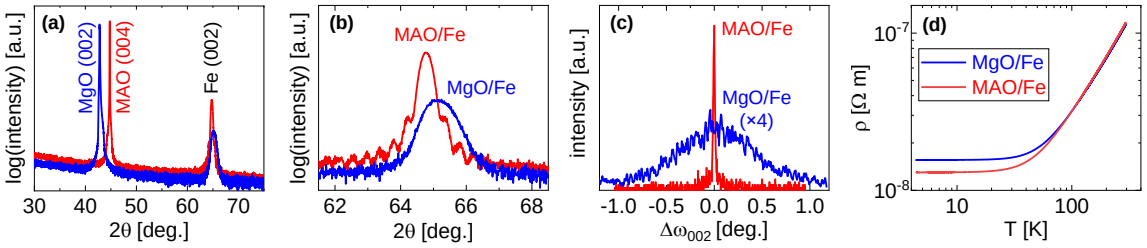

Figure 4.1: (a),(b) $2\theta - \omega$ x-ray diffraction scans of MAO=Fe and MgO=Fe (a) over a wide angle range and (b) near the bcc Fe (002) film peak. (c) Rocking curve scans about the film peak. (d) Temperature dependence of resistivity plotted on a log-log scale

mismatch. Static magnetometry provides further evidence that Fe is strained on MAO and relaxed on MgO [55]. Since strained MAO/Fe and relaxed MgO/Fe exhibit distinct crystalline quality, as evidenced by an approximately 50 times narrower rocking FWHM for MAO/Fe, we have two model systems that enable experimental investigation of the impact of structural disorder on Gilbert damping.

The residual electrical resistivity also reflects the structural quality of metals. As shown in Fig. 4.1(d), the residual resistivity is 20% lower for MAO/Fe compared to MgO/Fe, which corroborates the lower defect density in MAO/Fe. The resistivity increases by nearly an order of magnitude with increasing temperature, reaching 1.1×10^{-7} Ωm for both samples at room temperature, consistent with behavior expected for pure metal thin films. We now examine how the difference in crystalline quality correlates with magnetic damping in MAO/Fe and MgO/Fe. Broadband FMR measurements were performed at room temperature up to 65 GHz with a custom spectrometer that employs a coplanar waveguide (center conductor width 0.4 mm) and an electromagnet (maximum field < 2 T). For each measurement at a fixed excitation frequency, an external bias magnetic field was swept parallel to the film plane along the [110] axis of Fe, unless otherwise noted. In the Supplemental Material [55], we show similar results with the field applied along the [110] and [100] axes of Fe; Gilbert damping is essentially isotropic within the film plane for our epitaxial Fe films, in contrast to a recent report of anisotropic damping in ultrathin epitaxial Fe [29].

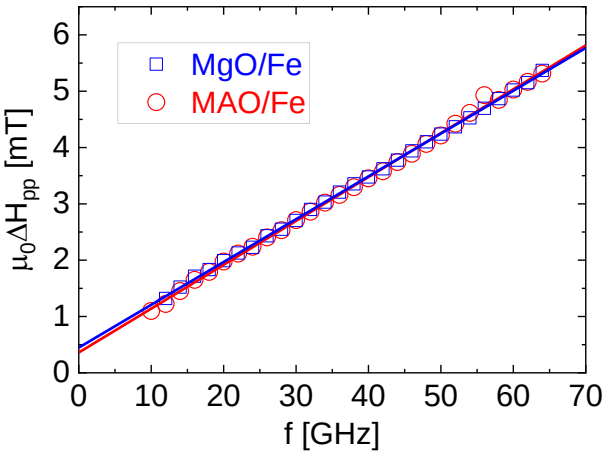

Figure 4.2: Frequency dependence of FMR linewidth $\Delta H_{\rm pp}$ for MAO/Fe and MgO/Fe at room temperature. Linewidths measured under in-plane field are shown as open symbols, whereas those measured under out-of-plane (OP) field are shown as filled symbols

Fig. 4.2 shows that the peak-to-peak FMR linewidth $\Delta H_{\rm pp}$ scales linearly with frequency f, enabling a precise determination of the measured Gilbert damping parameter $\alpha_{\rm meas}$ from the standard equation,

$$\mu_0 \Delta H_{\rm pp} = \mu_0 \Delta H_0 + \frac{2}{\sqrt{3}} \frac{\alpha_{\rm meas}}{\gamma'} f, \tag{4.1}$$

where ΔH_0 is the zero-frequency linewidth and $\gamma' = \gamma/2\pi \approx 29.5$ GHz/T is the reduced gyromagnetic ratio. Despite the difference in crystalline quality, we find essentially the same measured Gilbert damping parameter of $\alpha_{\rm meas} \approx 2.3 \times 10^{-3}$ for MAO/Fe and MgO/Fe. We note that this value of meas is comparable to the lowest damping parameters reported for epitaxial Fe at room temperature [21, 22, 24]. Our results indicate that Gilbert damping at room temperature is insensitive to the strain state or structural disorder in epitaxial Fe [66].

The measured damping parameter $\alpha_{\rm meas}$ from in-plane FMR can generally include a contribution from non-Gilbert relaxation, namely two-magnon scattering driven by defects [67–70]. However, two-magnon scattering is suppressed when the film is magnetized out-of-plane [26, 69]. To isolate any two-magnon scattering contribution to damping, we

performed out-of-plane FMR measurements under a sufficiently large magnetic field (> 4 T) for complete saturation of the Fe film, using a custom W-band shorted waveguide combined with a superconducting magnet. As shown in Fig. 4.2, the out-of-plane and in-plane FMR data yield the same slope and hence α_{meas} (Eqn. (4.1)) to within $< 8\%$. This finding indicates that two-magnon scattering is negligible and that frequency-dependent magnetic relaxation is dominated by Gilbert damping in epitaxial Fe examined here.

The insensitivity of Gilbert damping to disorder found in Fig. 4.2 can be explained by the dominance of the interband (resistivitylike) mechanism at room temperature, with phonon scattering dominating over defect scattering. Indeed, since MAO/Fe and MgO/Fe have the same room-temperature resistivity (Fig. 4.1(d)), any contributions to Gilbert damping from electronic scattering should be identical for both samples at room temperature. Moreover, according to our density functional theory calculations [55], the density of states of bcc Fe at the Fermi energy $D(E_{\mathrm{F}})$ does not depend significantly on the strain state of the crystal. Therefore, in light of the recent reports that Gilbert damping is proportional to $D(E_{\mathrm{F}})$ [23, 25, 71], the different strain states of MAO/Fe and MgO/Fe are not expected to cause a significant difference in Gilbert damping.

However, since MAO/Fe and MgO/Fe exhibit distinct resistivities (electronic scattering times e) at low temperatures, one might expect to observe distinct temperature dependence in Gilbert damping for these two samples. To this end, we performed variable-temperature FMR measurements using a coplanar-waveguide-based spectrometer (maximum frequency 40 GHz, field < 2 T) equipped with a closed-cycle cryostat. (The W-band spectrometer for out-of-plane FMR (Fig. 4.2) could not be cooled below room temperature due to its large thermal mass, limiting us to in plane FMR measurements at low temperatures.) Figs. 4.3(a) and 4.3(b) show that α_{meas} is enhanced for both samples at lower temperatures. Notably, this damping enhancement with decreasing temperature is significantly greater for MAO/Fe (Figs. 4.3(b) and 4.3(c)). Thus, at low temperatures, we find a conductivitylike damping increase that is evidently more pronounced in epitaxial Fe

with less structural disorder. While this increased damping at low temperatures is reminiscent of intrinsic Gilbert damping from intraband scattering [40–47], we first consider other possible contributions. One possibility is two-magnon scattering [67–70], which we have ruled out at room temperature (Fig. 4.2) but could be present in our low-temperature inplane FMR measurements. From Figs. 4.3(a) and 4.3(b), the zero-frequency linewidth ΔH_0 (Eqn. (4.1)) —typically attributed to magnetic inhomogeneity is shown to increase along with α_{meas} at low temperatures [55], which might

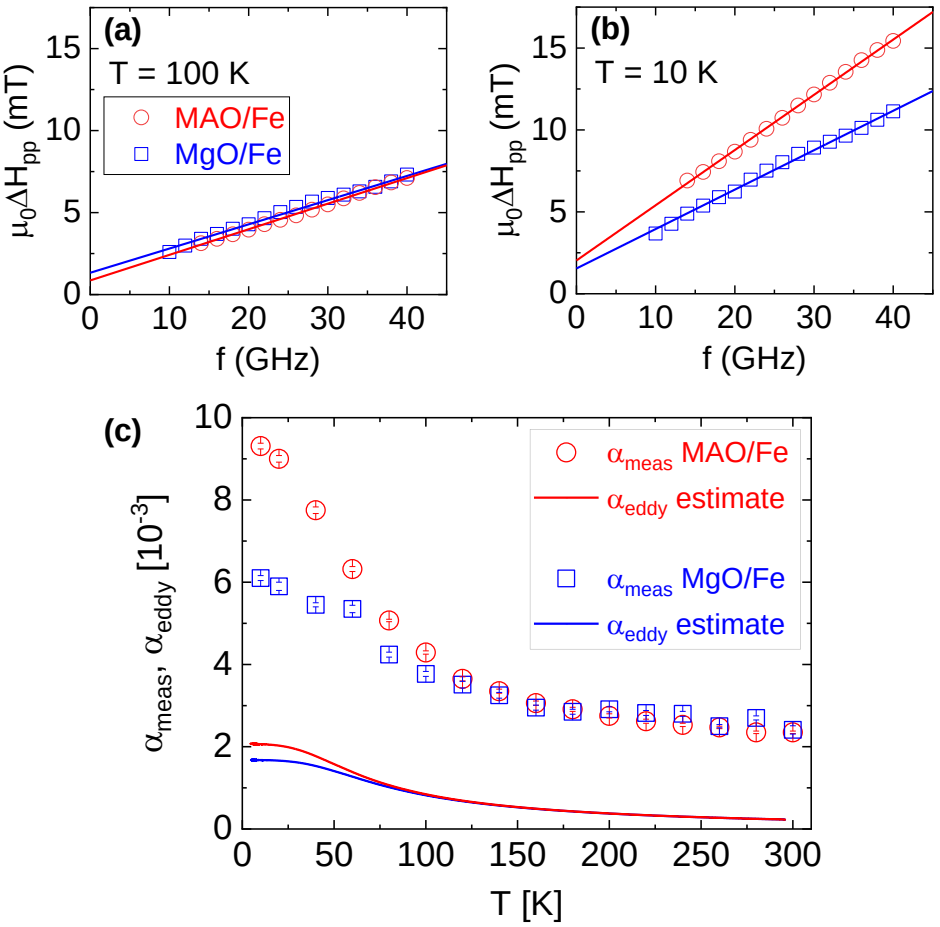

Figure 4.3: (a),(b) Frequency dependence of FMR linewidth for MAO/Fe and MgO/Fe at (a) $T = 100$ K and (b) $T = 10$ K. (c) Temperature dependence of measured Gilbert damping parameter α_{meas} and estimated eddy-current damping parameter α_{eddy}

point to the emergence of two-magnon scattering [69, 70]. However, our mean-field model calculations (see Supplemental Material [55]) show that ΔH_0 correlates with α_{meas} due to

interactions among different regions of the inhomogeneous film [72]. The increase of ΔH_0 at low temperatures is therefore readily accounted for by increased Gilbert damping, rather than two-magnon scattering.

We are also not aware of any mechanism that enhances two-magnon scattering with decreasing temperature, particularly given that the saturation magnetization (i.e., dipolar interactions) is constant across the measured temperature range [55]. Moreover, the isotropic in-plane damping found in our study is inconsistent with typically anisotropic two-magnon scattering tied to the crystal symmetry of epitaxial films [67, 68], and the film thickness in our study (e.g., 25 nm) rules out two-magnon scattering of interfacial origin [70]. As such, we conclude that two magnon scattering does not play any essential role in our experimental observations.

Another possible contribution is dissipation due to classical eddy currents, which increases proportionally with the increasing conductivity at lower temperatures. We estimate the eddy-current contribution to the measured Gilbert damping with [21, 73]

$$\alpha_{\text{eddy}} = \frac{\sigma}{12}\gamma\mu_0^2 M_s t_F^2, \tag{4.2}$$

where $\mu_0 M_{\text{s}} \approx 2.0$ T is the saturation magnetization and t_{F} is the film thickness. We find that eddy-current damping accounts for only $\approx 20\%$ ($\approx 30\%$) of the total measured damping of MAO/Fe (MgO/Fe) even at the lowest measured temperature (Fig. 4.3(c)). Furthermore, as shown in the Supplemental Material [55], thinner MAO/Fe films, e.g., $t_{\text{F}} = 11$ nm, with negligible α_{eddy} still exhibit a significant increase in damping with decreasing temperature. Our results thus indicate a substantial contribution to conductivitylike Gilbert damping that is not accounted for by classical eddy-current damping.

For further discussion, we subtract the eddy-current damping from the measured damping to denote the Gilbert damping parameter attributed to intrinsic spin-orbit coupling as $\alpha_{\text{so}} = \alpha_{\text{meas}} - \alpha_{\text{eddy}}$. To correlate electronic transport and magnetic damping

across the entire measured temperature range, we perform a phenomenological fit of the temperature dependence of Gilbert damping with [35]

$$\alpha_{\mathrm{so}} = c\frac{\sigma(T)}{\sigma(300\ \mathrm{K})} + d\frac{\rho(T)}{\rho(300\ \mathrm{K})}, \tag{4.3}$$

where the conductivitylike (intraband) and resistivitylike (interband) terms are scaled by adjustable parameters c and d, respectively. As shown in Figs. 4.4(a) and (b), this simple phenomenological model using the experimental transport results (Fig. 4.1(d)) agrees remarkably well with the temperature dependence of Gilbert damping for both MAO/Fe and MgO/Fe.

Our findings that Gilbert damping can be phenomenologically partitioned into two distinct contributions (Eqn. (4.3)) are in line with Kambersky's torque correlation model. We compare our experimental results to firstprinciples calculations by Gilmore et al. [41, 42] that relate electronic momentum scattering rate τ_{e}^{-1} and Gilbert damping through Kambersky's torque correlation model. We use the experimentally measured resistivity ρ [Fig. 4.1(d)] to convert the temperature to τ_{e}^{-1} by assuming the constant conversion factor $\rho\tau_{\mathrm{e}} = 1.30 \times 10^{-21}$ Ωms [42]. To account for the difference in electronic scattering time for the minority spin and majority spin $\tau_{\uparrow}$, we take the calculated curve from Gilmore et al. with $\tau_{\downarrow}/\tau_{\uparrow} = 4$ [42], which is close to the ratio of $D(E_{\mathrm{F}})$ of the spin-split bands for bcc Fe, e.g., derived from our density functional theory calculations [55]. For explicit comparison with Refs. [41, 42], the Gilbert damping parameter in Fig. 4.4(c) is converted to the magnetic relaxation rate $\lambda = \gamma\alpha_{\mathrm{so}}\mu_0 M_s$. The calculated prediction is in excellent quantitative agreement with our experimental results for both strained MAO/Fe and relaxed MgO/Fe (Fig. 4.4(c)), providing additional experimental evidence that intraband scattering predominately contributes to Gilbert damping at low temperatures.

We also compare our experimental results to a more recent first-principles calculation study by Mankovsky et al., which utilizes the linear response formalism [45]. This approach does not rely on a phenomenological electronic scattering rate and instead allows for

explicitly incorporating thermal effects and structural disorder. Fig. 4.4(d) shows the calculated temperature dependence of the Gilbert damping parameter for bcc Fe with a small density of defects, i.e., 0.1% vacancies, adapted from Ref. [45]. We again find good quantitative agreement between the calculations and our experimental results for MAO/Fe. On the other hand, the Gilbert damping parameters at low temperatures for relaxed MgO/Fe are significantly below the calculated values. This is consistent with the reduction

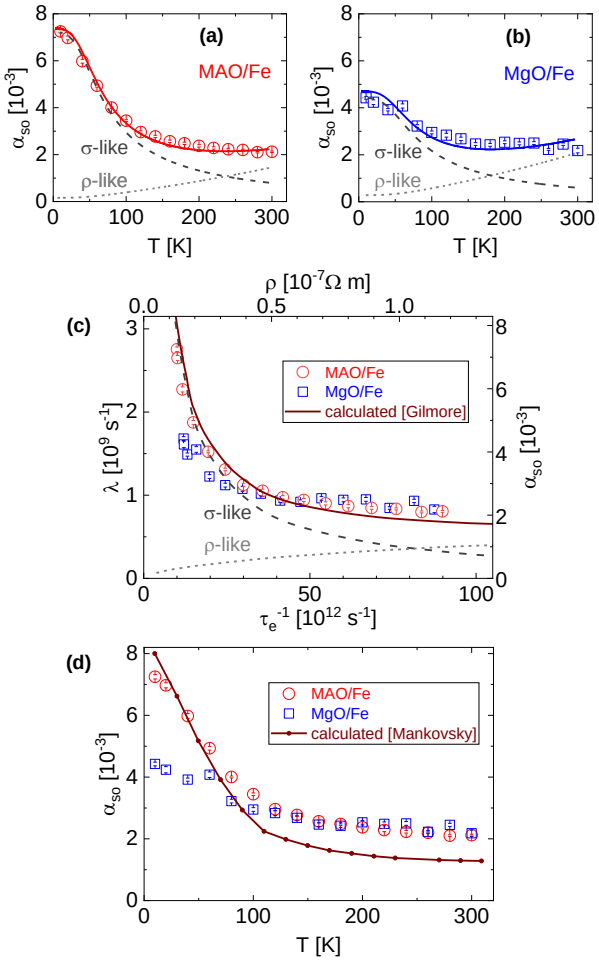

Figure 4.4: (a),(b) Temperature dependence of the spin-orbit-induced Gilbert damping parameter α_{so}, fit phenomenologically with the experimentally measured resistivity for (a) MAO/Fe and (b) MgO/Fe. The dashed and dotted curves indicate the conductivitylike and resistivitylike contributions, respectively; the solid curve represents the fit curve for the total spin-orbit-induced Gilbert damping parameter. (c),(d) Comparison of our experimental results with calculated Gilbert damping parameters by (c) Gilmore et al.[41, 42] and (d) Mankovsky et al. [45].

of intraband scattering due to enhanced electronic scattering (enhanced τ_e^{-1}) from defects in relaxed MgO/Fe.

Indeed, significant defect-mediated electronic scattering may explain the absence of conductivitylike Gilbert damping for crystalline Fe in prior experiments. For example, Ref. [34] reports an upper limit of only a twofold increase of the estimated Gilbert damping parameter from $T = 300$K to 4K. This relatively small damping enhancement is similar to that for MgO/Fe in our study (Fig. 4.4(b)), suggesting that intraband scattering may have been suppressed in Fe in reference [34] due to a similar degree of structural disorder to MgO/Fe. We therefore conclude that conductivitylike Gilbert damping from intraband scattering is highly sensitive to disorder in ferromagnetic metals.

More generally, the presence of defects in all real metals —evidenced by finite residual resistivity—ensures that the Gilbert damping parameter is finite even in the zerotemperature limit. This circumvents the theoretical deficiency of Kambersky's torque correlation model where Gilbert damping would diverge in a perfectly clean ferromagnetic metal at $T \to 0$[48, 49]. We also remark that a fully quantum mechanical many-body theory of magnetization dynamics yields finite Gilbert damping even in the clean $T = 0$ limit [74].

4.3 Summary

we have demonstrated the dominance of conductivitylike Gilbert damping due to intraband scattering at low temperatures in high-quality epitaxial Fe. Our experimental results also validate the long-standing theoretical prediction of intraband scattering as an essential mechanism for Gilbert damping in pure ferromagnetic metals [41–47], thereby advancing the fundamental understanding of magnetic relaxation in real materials. Moreover, we have confirmed that, at low temperatures, a magnetic metal with imperfect crystallinity can exhibit lower Gilbert damping (spin decoherence) than its cleaner counterpart. This somewhat counterintuitive finding suggests that magnetic thin films with

optimal structural or chemical disorder may be useful for cryogenic spintronic memories [51, 52] and spinwave-driven quantum information systems [53, 54].

4.4 Acknowledgements

This research was funded in part by 4-VA, a collaborative partnership for advancing the Commonwealth of Virginia, as well as by the ICTAS Junior Faculty Award. A. Sapkota and C. M. would like to acknowledge support by NSFCAREER Award No. 1452670, A. R. and T. M. would like to acknowledge support by DARPA TEE Award No. D18AP00011, and A. Srivastava would like to acknowledge support by NASA Award No. CAN80NSSC18M0023. We thank M. D. Stiles, B. K. Nikolic, and F. Mahfouzi for helpful discussions on theoretical models for computing Gilbert damping, as well as R. D. McMichael for his input on the mean-field modeling of interactions in inhomogeneous ferromagnetic films.

4.5 References

[1] B. Heinrich, *Spin Relaxation in Magnetic Metallic Layers and Multilayers* (Springer Berlin Heidelberg, Berlin, Heidelberg, 2005), pp. 143–210.

[2] C. K. Mewes and T. Mewes, *Relaxation in magnetic materials for spintronics* (Pan Stanford Publishing Singapore, 2015), pp. 71–96.

[3] D. Ralph and M. Stiles, J. Magn. Magn. Mater. **320**, 1190 (2008).

[4] A. Brataas and A. D. Kent, Nat. Mater. **11**, 1476 (2012).

[5] A. Mougin, M. Cormier, J. P. Adam, P. J. Metaxas, and J. Ferré, EPL **78**, 57007 (2007).

[6] T. Weindler, H. G. Bauer, R. Islinger, B. Boehm, J.-Y. Chauleau, and C. H. Back, Phys. Rev. Lett. **113**, 237204 (2014).

[7] A. V. Chumak, V. I. Vasyuchka, A. A. Serga, and B. Hillebrands, Nat. Mater. **11**, 1745 (2015).

[8] E. Sonin, Adv. Phys. **59**, 181 (2010).

[9] O. d'Allivy Kelly, A. Anane, R. Bernard, J. Ben Youssef, C. Hahn, A. H. Molpeceres, C. Carrétéro, E. Jacquet, C. Deranlot, P. Bortolotti, et al., Appl. Phys. Lett. **103**, 082408 (2013).

[10] H. Chang, P. Li, W. Zhang, T. Liu, A. Hoffmann, L. Deng, and M. Wu, IEEE Magn. Lett. **5**, 1 (2014).

[11] M. C. Onbasli, A. Kehlberger, D. H. Kim, G. Jakob, M. Kläui, A. V. Chumak, B. Hillebrands, and C. A. Ross, APL Mater. **2**, 106102 (2014).

[12] C. Du, H. Wang, P. C. Hammel, and F. Yang, J. Appl. Phys. **117**, 172603 (2015).

[13] C. Tang, M. Aldosary, Z. Jiang, H. Chang, B. Madon, K. Chan, M. Wu, J. E. Garay, and J. Shi, Appl. Phys. Lett. **108**, 102403 (2016).

[14] C. Hauser, T. Richter, N. Homonnay, C. Eisenschmidt, M. Qaid, H. Deniz, D. Hesse, M. Sawicki, S. G. Ebbinghaus, and G. Schmidt, Sci. Rep. **6**, 20827 (2016).

[15] C. Dubs, O. Surzhenko, R. Linke, A. Danilewsky, U. Brückner, and J. Dellith, J. Phys. D Appl. Phys. **50**, 204005 (2017).

[16] L. Soumah, N. Beaulieu, L. Qassym, C. Carrétéro, E. Jacquet, R. Lebourgeois, J. Ben Youssef, P. Bortolotti, V. Cros, and A. Anane, Nat. Commun. **9**, 3355 (2018).

[17] A. V. Singh, B. Khodadadi, J. B. Mohammadi, S. Keshavarz, T. Mewes, D. S. Negi, R. Datta, Z. Galazka, R. Uecker, and A. Gupta, Adv. Mater. **29**, 1701222 (2017).

[18] S. Emori, D. Yi, S. Crossley, J. J. Wisser, P. P. Balakrishnan, B. Khodadadi, P. Shafer, C. Klewe, A. T. N'Diaye, B. T. Urwin, et al., Nano Lett. **18**, 4273 (2018), ISSN 1530-6984.

[19] H. Liu, C. Zhang, H. Malissa, M. Groesbeck, M. Kavand, R. McLaughlin, S. Jamali, J. Hao, D. Sun, R. A. Davidson, et al., Nat. Mater. **17**, 308 (2018).

[20] M. Oogane, T. Wakitani, S. Yakata, R. Yilgin, Y. Ando, A. Sakuma, and T. Miyazaki, Jpn. J. Appl. Phys. **45**, 3889 (2006).

[21] C. Scheck, L. Cheng, and W. E. Bailey, Appl. Phys. Lett. **88**, 252510 (2006).

[22] C. Scheck, L. Cheng, I. Barsukov, Z. Frait, and W. E. Bailey, Phys. Rev. Lett. **98**, 117601 (2007).

[23] S. Mizukami, D. Watanabe, M. Oogane, Y. Ando, Y. Miura, M. Shirai, and T. Miyazaki, J. Appl. Phys. **105**, 07D306 (2009).

[24] B. Kardasz, E. A. Montoya, C. Eyrich, E. Girt, and B. Heinrich, J. Appl. Phys. **109**, 07D337 (2011).

[25] M. A. W. Schoen, D. Thonig, M. L. Schneider, T. J. Silva, H. T. Nembach, O. Eriksson, O. Karis, and J. M. Shaw, Nat. Phys. **12**, 839 (2016).

[26] M. A. W. Schoen, J. Lucassen, H. T. Nembach, B. Koopmans, T. J. Silva, C. H. Back, and J. M. Shaw, Phys. Rev. B **95**, 134411 (2017).

[27] A. J. Lee, J. T. Brangham, Y. Cheng, S. P. White, W. T. Ruane, B. D. Esser, D. W. McComb, P. C. Hammel, and F. Yang, Nat. Commun. **8**, 234 (2017).

[28] H. S. Körner, M. A. W. Schoen, T. Mayer, M. M. Decker, J. Stigloher, T. Weindler, T. N. G. Meier, M. Kronseder, and C. H. Back, Appl. Phys. Lett. **111**, 132406 (2017).

[29] L. Chen, S. Mankovsky, S. Wimmer, M. A. W. Schoen, H. S. Körner, M. Kronseder, D. Schuh, D. Bougeard, H. Ebert, D. Weiss, et al., Nat. Phys. **14**, 1745 (2018).

[30] Y. Li, F. Zeng, S. S.-L. Zhang, H. Shin, H. Saglam, V. Karakas, O. Ozatay, J. E. Pearson, O. G. Heinonen, Y. Wu, et al., Phys. Rev. Lett. **122**, 117203 (2019).

[31] C. Guillemard, S. Petit-Watelot, L. Pasquier, D. Pierre, J. Ghanbaja, J.-C. Rojas-Sánchez, A. Bataille, J. Rault, P. Le Fèvre, F. Bertran, et al., Phys. Rev. Appl. **11**, 064009 (2019).

[32] C. Guillemard, S. Petit-Watelot, J.-C. Rojas-Sánchez, J. Hohlfeld, J. Ghanbaja, A. Bataille, P. Le Fèvre, F. Bertran, and S. Andrieu, Appl. Phys. Lett. **115**, 172401 (2019).

[33] V. Kamberský, Czechoslov. J. Phys. **26**, 1366 (1976).

[34] S. M. Bhagat and P. Lubitz, Phys. Rev. B **10**, 179 (1974).

[35] B. Heinrich, D. J. Meredith, and J. F. Cochran, J. Appl. Phys. **50**, 7726 (1979).

[36] J. M. Rudd, J. F. Cochran, K. B. Urquhart, K. Myrtle, and B. Heinrich, J. Appl. Phys. **63**, 3811 (1988).

[37] J. F. Cochran, J. M. Rudd, W. B. Muir, G. Trayling, and B. Heinrich, J. Appl. Phys. **70**, 6545 (1991).

[38] X. Ma, L. Ma, P. He, H. B. Zhao, S. M. Zhou, and G. Lüpke, Phys. Rev. B **91**, 014438 (2015).

[39] B. Heinrich and Z. Frait, Phys. Status Solidi B **16**, K11 (1966).

[40] V. Kamberský, Can. J. Phys. **48**, 2906 (1970).

[41] K. Gilmore, Y. U. Idzerda, and M. D. Stiles, Phys. Rev. Lett. **99**, 027204 (2007).

[42] K. Gilmore, *Precession damping in itinerant ferromagnets,* Montana State University (2007).

[43] A. A. Starikov, P. J. Kelly, A. Brataas, Y. Tserkovnyak, and G. E. W. Bauer, Phys. Rev. Lett. **105**, 236601 (2010).

[44] Y. Liu, A. A. Starikov, Z. Yuan, and P. J. Kelly, Phys. Rev. B **84**, 014412 (2011).

[45] S. Mankovsky, D. Ködderitzsch, G. Woltersdorf, and H. Ebert, Phys. Rev. B **87**, 014430 (2013).

[46] Barati, E., Cinal, M., Edwards, D. M., and Umerski, A., EPJ Web Conf. **40**, 18003 (2013).

[47] T. Qu and R. H. Victora, J. Appl. Phys. **115**, 17C506 (2014).

[48] A. T. Costa and R. B. Muniz, Phys. Rev. B **92**, 014419 (2015).

[49] D. M. Edwards, J. Condens. Matter Phys. **28**, 086004 (2016).

[50] Reference [45] includes experimental data that suggest the presence of conductivitylike Gilbert damping in an ultrathin Fe film, although no detailed information is given about the sample and the experimental results deviate considerably from the calculations. An earlier study by Rudd et al. also suggests an increase in Gilbert damping with decreasing temperature [36], but quantification of the Gilbert damping parameter in this experiment is difficult.

[51] G. E. Rowlands, C. A. Ryan, L. Ye, L. Rehm, D. Pinna, A. D. Kent, and T. A. Ohki, Sci. Rep. **9**, 803 (2019).

[52] M.-H. Nguyen, G. J. Ribeill, M. V. Gustafsson, S. Shi, S. V. Aradhya, A. P. Wagner, L. M. Ranzani, L. Zhu, R. Baghdadi, B. Butters, et al., Sci. Rep. **10**, 248 (2020).

[53] Y. Li, T. Polakovic, Y.-L. Wang, J. Xu, S. Lendinez, Z. Zhang, J. Ding, T. Khaire, H. Saglam, R. Divan, et al., Phys. Rev. Lett. **123**, 107701 (2019).

[54] J. T. Hou and L. Liu, Phys. Rev. Lett. **123**, 107702 (2019).

[55] See Supplemental Material for additional information on film growth and structure, angular dependence of static magnetic properties and damping, density of states calculations, eddy-current damping estimation, film thickness dependence of resistivity and damping, and temperature dependence of zero-frequency linewidth and spectroscopic parameters, which includes Refs. [56–65].

[56] R. C. O'Handley, *Magnetoelastic effects* (Wiley Interscience New York, 2000), pp. 218—-273.

[57] K. Gilmore, M. D. Stiles, J. Seib, D. Steiauf, and M. Fähnle, Phys. Rev. B **81**, 174414 (2010).

[58] P. Giannozzi, S. Baroni, N. Bonini, M. Calandra, R. Car, C. Cavazzoni, D. Ceresoli, G. L. Chiarotti, M. Cococcioni, I. Dabo, et al., J. Condens. Matter Phys. **21**, 395502 (2009).

[59] J. P. Perdew, A. Ruzsinszky, G. I. Csonka, O. A. Vydrov, G. E. Scuseria, L. A. Constantin, X. Zhou, and K. Burke, Phys. Rev. Lett. **100**, 136406 (2008).

[60] D. Vanderbilt, Phys. Rev. B **41**, 7892 (1990).

[61] H. J. Monkhorst and J. D. Pack, Phys. Rev. B **13**, 5188 (1976).

[62] A. Dal Corso, Comput. Mater. Sci. **95**, 337 (2014).

[63] R. Schad, P. Beliën, G. Verbanck, C. Potter, K. Temst, V. Moshchalkov, and Y. Bruynseraede, J. Magn. Magn. Mater. **182**, 65 (1998).

[64] E. Schlömann, Phys. Rev. **182**, 632 (1969).

[65] M. Farle, Rep. Prog. Phys. **61**, 755 (1998).

[66] However, the crystallographic texture of Fe has significant impact on damping; for example, nonepitaxial Fe films deposited directly on amorphous SiO2 substrates exhibit an order of magnitude wider linewidths, due to much more pronounced non-Gilbert damping (e.g., two-magnon scattering), compared to (001)-oriented epitaxial Fe films.

[67] G. Woltersdorf and B. Heinrich, Phys. Rev. B **69**, 184417 (2004).

[68] K. Lenz, H. Wende, W. Kuch, K. Baberschke, K. Nagy, and A. Jánossy, Phys. Rev. B **73**, 144424 (2006).

[69] R. McMichael and P. Krivosik, IEEE Trans. Magn. **40**, 2 (2004).

[70] R. Arias and D. L. Mills, Phys. Rev. B **60**, 7395 (1999).

[71] C. Liu, C. K. A. Mewes, M. Chshiev, T. Mewes, and W. H. Butler, Appl. Phys. Lett. **95**, 022509 (2009).

[72] R. D. McMichael, J. Appl. Phys. **103**, 07B114 (2008).

[73] J. M. Lock, Br. J. Appl. Phys. **17**, 1645 (1966).

[74] F. Mahfouzi, J. Kim, and N. Kioussis, Phys. Rev. B **96**, 214421 (2017).

5 SUPPLEMENTAL MATERIAL:CONDUCTIVITY-LIKE GILBERT DAMPING DUE TO INTRABAND SCATTERING IN EPITAXIAL IRON

Behrouz Khodadadi,[1] Anish Rai,[2] Arjun Sapkota,[2] Abhishek Srivastava,[2] Bhuwan Nepal,[2] Youngmin Lim,[1] David A. Smith,[1] Claudia Mewes,[2] Sujan Budhathoki ,[2] Adam J. Hauser,[2] Min Gao,[3] Jie-Fang Li,[3] Dwight D. Viehland,[3] Zijian Jiang,[1] Jean J. Heremans,[1] Prasanna V. Balachandran,[4,5] Tim Mewes, [2] and Satoru Emori, [1]

[1]*Department of Physics, Virginia Tech, Blacksburg, VA 24061, USA*

[2]*Department of Physics and Astronomy, The University of Alabama, Tuscaloosa, AL 35487, USA*

[3]*Department of Material Science and Engineering, Virginia Tech, Blacksburg, VA 24061, USA*

[4]*Department of Material Science and Engineering, University of Virginia, Charlottesville, VA 22904, USA*

[5]*Department of Mechanical and Aerospace Engineering, University of Virginia, Charlottesville, VA 22904, USA*

*This chapter is a reformatted reprint of the supplementary materials of the paper that appeared in Phys. Rev. Lett. 124, 157201 (2020).

5.1 Film Growth

Epitaxial BCC Fe films (including the 25-nm-thick films shown in the main text) were grown on MAO and MgO by confocal DC magnetron sputtering in a deposition chamber with a base pressure of $< 5 \times 10^{-8}$ Torr. The substrates were annealed at 600°C for 2 hours prior to film deposition. The films were deposited at a rate of 0.035 nm/s by sputtering a 2"-diameter, 99.99%-pure Fe target at an Ar pressure of 3 mTorr, target-to-substrate distance of 12 cm, and a substrate temperature of 200°C. A 3-nm-thick Ti capping layer was deposited at room temperature to protect the films from oxidization.

Epitaxial BCC Fe thin films of thicknesses 11 nm and 19 nm were deposited on (001)-oriented $MgAl_2O_4$ (MAO) single crystal substrates by off-axis DC magnetron sputtering in an ultra-high vacuum chamber with base pressure 5×10^{-9} Torr. The films were deposited by sputtering a 1.5"-diameter, 99.99%-pure Fe target. The substrates were located at an off-axis angle of 70°C with respect to target normal direction and subject to sample rotation during preheating and deposition. The substrates were annealed at 500°C for 30 minutes followed by film deposition at a substrate temperature of 200°C in a pure Ar environment of pressure 10 mTorr. A 3-nm-thick Al capping layer was deposited at < 100°C to prevent film oxidation.

5.2 Structural Characterization of Epitaxial Fe Films of Different Thicknesses

As shown in Fig. 5.1, the out-of-plane lattice parameter (derived from symmetric $2\theta - \omega$ XRD scans) of MAO/Fe is constant up to a film thickness t_F of at least ≈ 40 nm. This suggests that the MAO/Fe film ($t_F = 25$ nm) shown in the main text is coherently strained to the substrate. From the out-of-plane lattice parameter $c = 0.2876$ nm and assuming the in-plane lattice parameter $a = a_{MAO}/(2\sqrt{2})$, Fe on MAO is compressively strained in the film plane with a tetragonal distortion of $c/a = 1.006$. We also note that the film-peak rocking curve FWHMs for all MAO/Fe films were substrate limited. By contrast, the out-of-plane lattice parameter of MgO/Fe with $t_F = 25$ nm is essentially at the bulk value, suggesting that the MgO/Fe film shown in the main text is relaxed.

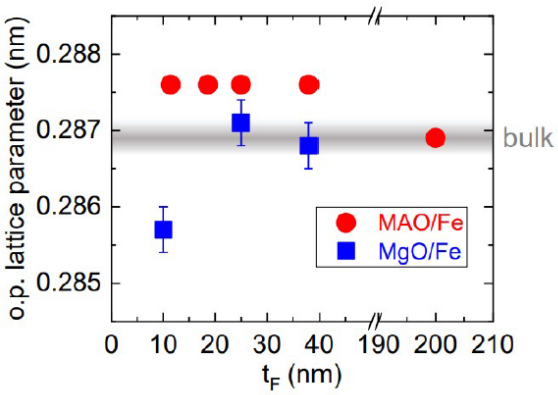

Figure 5.1: Thickness dependence of the out-of-plane lattice parameter. The error bars for MgO/Fe take into account the $\approx 0.05°$ uncertainty in the position of the broad Fe (002) film peak.

5.3 Static Magnetization Curves

Fig. 5.2 shows in-plane magnetic hysteresis curves of the MAO/Fe and MgO/Fe samples shown in the main text, measured at room temperature with a vibrating sample magnetometer (MicroSense EZ9). While for both films the easy axis is along $< 100 >$ of Fe ($< 110 >$ of MAO and MgO), the higher coercivity for MgO/Fe suggests a higher density of defects that impede the expansion of reversed magnetic domains.

We also remark that MAO/Fe shows a gradual approach to saturation, appearing as vertical openings in the hysteresis loop; such openings are less pronounced for MgO/Fe. We attribute this unique feature in strained MAO/Fe to magnetoelastic anisotropy that arises from the in-plane biaxial compressive strain, $\varepsilon < 0$, coupled to the magnetostriction coefficient of Fe, $\lambda_{100} > 0$; in particular, with $\lambda_{100}\varepsilon > 0$, it is known that the magnetic saturation process along the strain axes becomes harder [1]. The absence of this pronounced magnetoelastic effect in MgO/Fe is additional evidence that Fe on MgO is mostly relaxed, i.e., free of strain, consistent with our structural characterization results in Fig. 5.1.

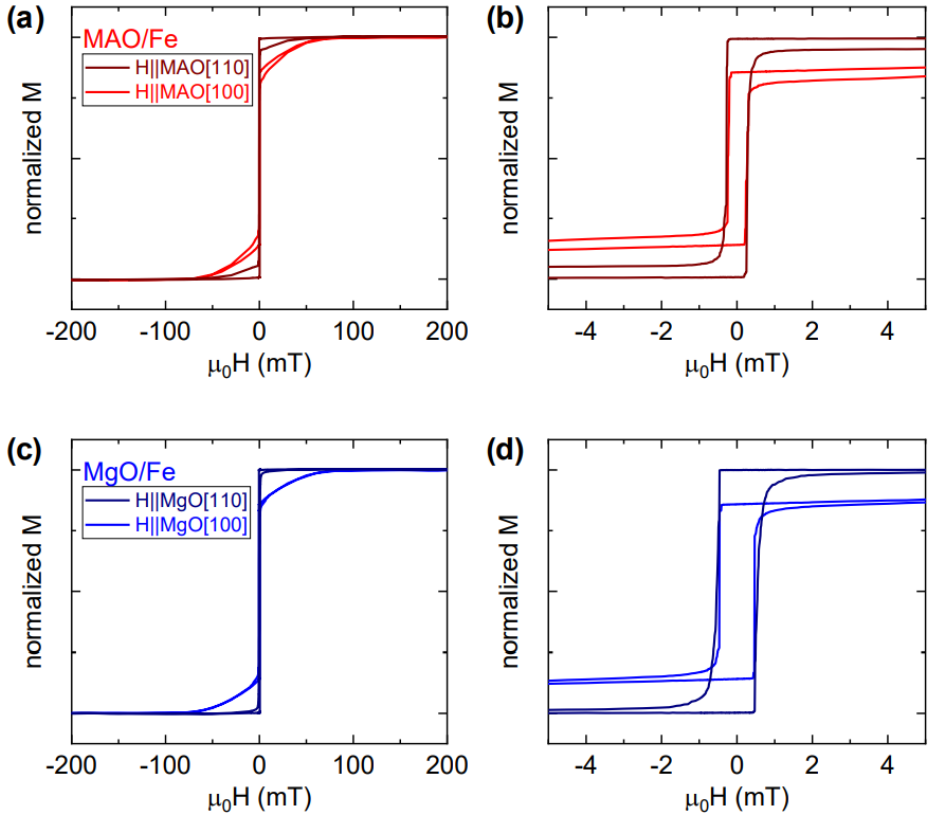

Figure 5.2: In-plane magnetization curves at room temperature for (a,b) MAO/Fe(25 nm) and (c,d) MgO/Fe(25 nm) measured at room temperature. (b) and (d) are close-up plots to highlight the difference in coercivity between MAO/Fe and MgO/Fe.

5.4 Angular Independence of Gilbert Damping

While Fe films on (001)-oriented MAO and MgO exhibit clear in-plane cubic magnetic anisotropy, as evidenced by static magnetometry (Fig. 5.2) and ferromagnetic resonance (Fig. 5.3(a,b)), we find that Gilbert damping is mostly isotropic in the film plane. For instance, the FMR linewidth at room temperature is essentially independent of in-plane magnetization orientation (Fig. 5.3(c,d)).

Theoretical studies have reported that spin-orbit-induced Gilbert damping in Fe may be anisotropic in the clean, low-temperature limit [2, 3], e.g., approximately 20% higher damping for magnetization precessing about $< 110 >$ compared to $< 100 >$ of BCC Fe [2]. To test this prediction, we performed broadband FMR on MAO/Fe with magnetic field

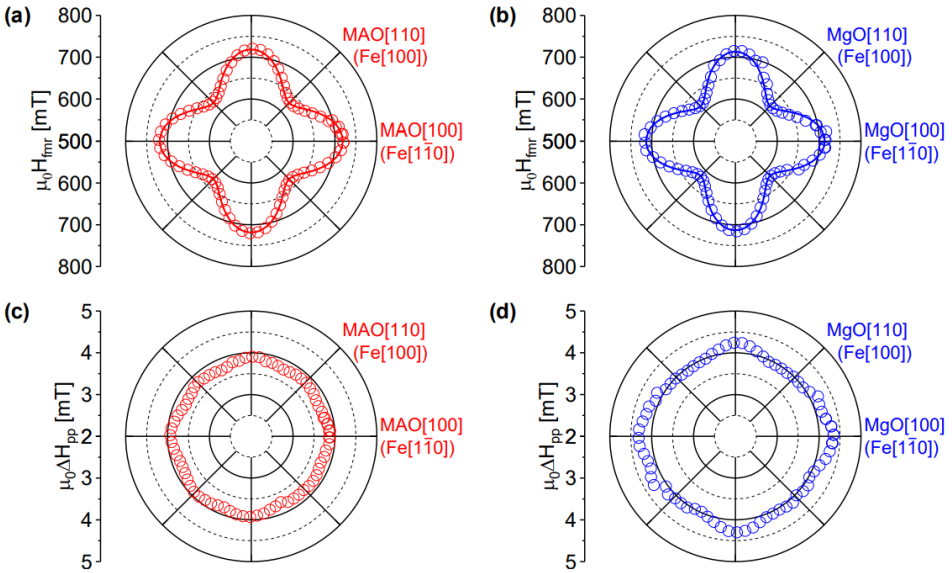

Figure 5.3: In-plane angular dependence of (a,b) resonance field $H_{\rm fmr}$ and (c,d) peak-to-peak FMR linewidth $\Delta H_{\rm pp}$ for (a,c) MAO/Fe(25 nm) and (b,d) MgO/Fe(25 nm) measured at 40 GHz and room temperature. .

applied along Fe$<110>$ and Fe$<100>$. As shown in Fig. 5.4, we find that the measured Gilbert damping parameter is similar for those two magnetization directions, with the damping parameter for Fe$<110>$ higher than Fe$<100>$ by at most only $\approx 10\%$. Our results therefore suggest that anisotropic spin-orbit-induced Gilbert damping, if present, is small in clean epitaxial BCC Fe.

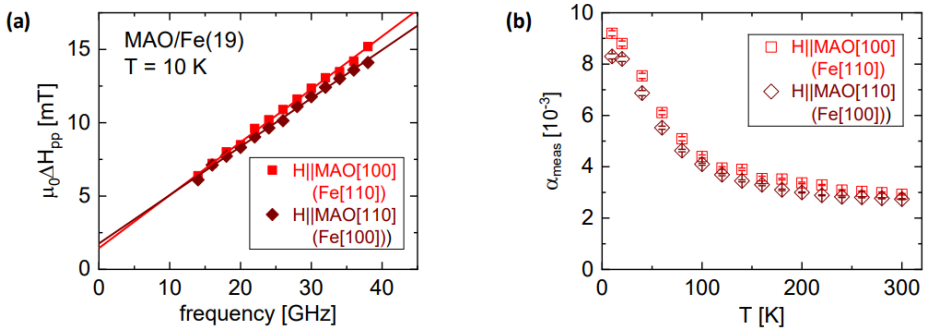

Figure 5.4: Frequency dependence of FMR linewidth for MAO/Fe(19 nm) magnetized along the two principal inplane crystallographic axes at $T = 10$ K. (b) Temperature dependence of the measured Gilbert damping parameter for Fe magnetized along the two principal axes.

5.5 Electronic Band Structure of Strained BCC Fe

Density functional theory (DFT) calculations were performed within the generalized gradient approximation (GGA) as implemented in the planewave pseudopotential code, Quantum ESPRESSO [4]. Initially, a unit cell of BCC-Fe was considered for the calculations. The PBEsol exchange-correlation functional was used [5]. The core and valence electrons were treated with ultrasoft pseudopotentials [6]. Collinear ferromagnetic spin-order was imposed on the Fe-atoms. The Brillouin zone integration was performed using a Monkhorst-Pack [7] k-point mesh centered at $\mathbf{\Gamma}$ and 60 Ry plane-wave cutoff for wavefunctions (600 Ry kinetic energy cutoff for charge density and potential). The scalar relativistic pseudopotentials were taken from the PSLibrary [8]. The atomic positions and the cell volume were allowed to relax until an energy convergence threshold of 10^{-8} eV and Hellmann-Feynman forces less than 2 meV/Å, respectively, were achieved. The non-self-consistent field calculations were performed using a dense $24 \times 24 \times 24$ k-mesh centered at $\mathbf{\Gamma}$-point. A sequence of 1-5% tensile and compressive epitaxial strains (in a step size of 1%) were imposed on the in-plane lattice constants. The out-of-plane lattice constant was allowed to relax. In addition to the unit cell, we also considered a $2 \times 2 \times 2$ supercell. In this case, we also constrained the lattice constants to 0, 2 and 4% epitaxial tensile strain. The non-self-consistent field calculations were performed using a dense $16 \times 16 \times 16$ k-mesh centered at $\mathbf{\Gamma}$-point. The computed electronic band structure for strained BCC Fe (unit cell) is shown in Figure S5. The density of states near the Fermi energy E_F ($D(E_F)$) is insensitive to strain, even at values (≈ 5 %) that are an order of magnitude larger than that of strained MAO/Fe films in our experiment. This finding suggests that $D(E_F)$ should be approximately the same for strained MAO/Fe and relaxed MgO/Fe; $D(E_F)$ alone is not expected to contribute to any difference in Gilbert damping between MAO/Fe and MgO/Fe. The $D(E_F)$ for the epitaxially tensile strained $2 \times 2 \times 2$ supercell also followed the same trend as that of the unit cell.

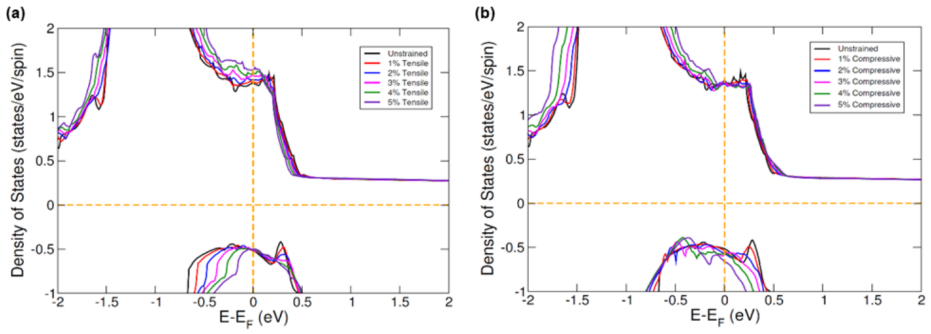

Figure 5.5: Calculated electronic density of states for (a) tensile strained and (b) compressive strained BCC Fe unit cell. The Fermi energy E_F is set to zero.

5.6 Estimation of Eddy Current Damping

To estimate the eddy current contribution to Gilbert damping, we start with the model used in Scheck et al. [9] (adapted from an earlier study by Lock [10]) for computing the magnetic relaxation rate λ_{eddy} , which is in CGS units,

$$\lambda_{eddy}^{CGS} = \frac{1}{12}\sigma \left(4\pi\gamma M_s\right)^2 \left(\frac{t_F}{c}\right)^2. \tag{5.1}$$

We note that the definitions of the relaxation rate are different in the CGS and SI unit systems (see for example references [11, 12]),

$$\lambda_{eddy}^{SI} = 4\pi\lambda_{eddy}^{CGS}. \tag{5.2}$$

while the Gilbert damping parameter is identical in CGS and SI units,

$$\alpha_{eddy} = \alpha_{eddy}^{SI} = \alpha_{eddy}^{CGS}. \tag{5.3}$$

To obtain the relaxation rate in SI units, we combine Eqns. (5.1) and (5.2) and then transform $\sigma \to \sigma/\left(4\pi\epsilon_0\right), c \to 1/\sqrt{\epsilon_0\mu_0}$, and $4\pi M_s \to \mu_0 M_s$

$$\lambda_{eddy}^{SI} = \frac{1}{12}\sigma\mu_0 \left(\gamma\mu_0 M_s\right)^2 t_F^2. \tag{5.4}$$

Finally, from $\lambda_{\text{eddy}}^{SI} = \gamma\alpha_{\text{eddy}}\,\mu_0 M_s$, we arrive at Eq. 2 in the main text, which is reproduced below:

$$\alpha_{eddy} = \frac{\sigma}{12}\gamma\mu_0^2 M_s t_F^2, \tag{5.5}$$

where $\gamma \approx 2\pi \times 29.5 \times 10^9$ T^{-1} s^{-1} and $\mu_0 M_s \approx 2.0$ T for epitaxial Fe films studied here.

5.7 Electronic Scattering in Epitaxial Fe Films with Different Thicknesses

Fig. 5.6 summarizes the transport properties of epitaxial Fe with different thicknesses. Thinner films exhibit higher room-temperature resistivity (Fig. 5.6(b)) and higher residual resistivity (Fig. 5.6(c)). This trend can be attributed to surface scattering. For a given Fe film thickness, relaxed MgO/Fe (poorer crystalline quality) exhibits $\approx 20\%$ greater residual resistivity than strained MAO/Fe (better crystalline quality), as shown in Fig. 5.6(c). This trend can be attributed to scattering by defects (e.g., dislocations) in the film bulk. At room temperature, this bulk defect scattering plays a minor role compared to phonon scattering, as evidenced by the nearly same room-temperature resistivity for MAO/Fe and MgO/Fe (Fig. 5.6(b)).

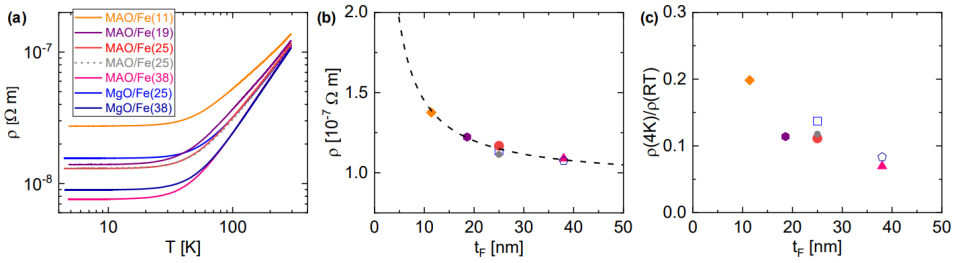

Figure 5.6: (a)Temperature dependence of resistivity for MAO/Fe and MgO/Fe with different Fe film thicknesses. (b) Film thickness dependence of room-temperature resistivity. The dashed curve indicates the fit using a simplified Fuchs-Sondheimer model. (c) Ratio of residual resistivity to room-temperature resistivity versus film thickness. In (b) and (c), the closed symbols represent MAO/Fe and the open symbols represent MgO/Fe.

The fit curve in Fig. 5.6(b) was obtained with the simplified Fuchs-Sondheimer model,

$$\rho = \rho_\infty \left(1 + \frac{3}{8}(1-p)l/t_F\right), \tag{5.6}$$

where ρ_∞ is the resistivity in the bulk limit, p is the specularity parameter, and l is the mean free path in the bulk. We set $p = 0$ to minimize the number of free parameters and quantify the lower bound of l. We find $\rho_\infty = 0.95 \times 10^{-7}$ m and $l = 14$ nm at room temperature, close to values reported previously for epitaxial Fe films grown by molecular beam epitaxy [13].

5.8 Gilbert Damping in Epitaxial Fe Films with Different Thicknesses

Fig. 5.7 shows the temperature dependence of the measured Gilbert damping parameter, along with the estimated eddy current Gilbert damping (using the experimentally measured resistivity from Fig. 5.6(a), for MAO/Fe films with thicknesses smaller than that shown in the main text. The eddy current contribution to Gilbert damping is negligible in MAO/Fe(11 nm) (Fig. 5.7(a)). The increase of Gilbert damping with decreasing temperature in this sample is therefore dominated by spin-orbit-induced Gilbert damping, i.e., mediated by intraband scattering. The temperature dependence of Gilbert damping for MAO/Fe(19 nm) shown in Fig. 5.7(b) is similar to that of MAO/Fe(25 nm) shown in the main text. We note that the MAO/Fe(11, 19 nm) samples in Fig. 5.7 were grown in a different deposition system from the MAO/Fe(25 nm) samples in the main text. The fact that these films exhibit similar results corroborates the universal nature of spin-orbit-induced conductivity-like Gilbert damping in epitaxial pure Fe.

The significantly smaller Gilbert damping at low temperature for MAO/Fe(11 nm), compared to its thicker counterparts, is due to the higher residual resistivity of this thinner film. This is readily seen in Fig. 5.8, where the spin-orbit-induced Gilbert damping parameter (or magnetic relaxation rate) is plotted against resistivity (or electronic momentum relaxation rate). To within a factor of ≈ 1.5, all samples of epitaxial Fe fall on top of the same curve computationally derived by Gilmore et al. [11, 12].

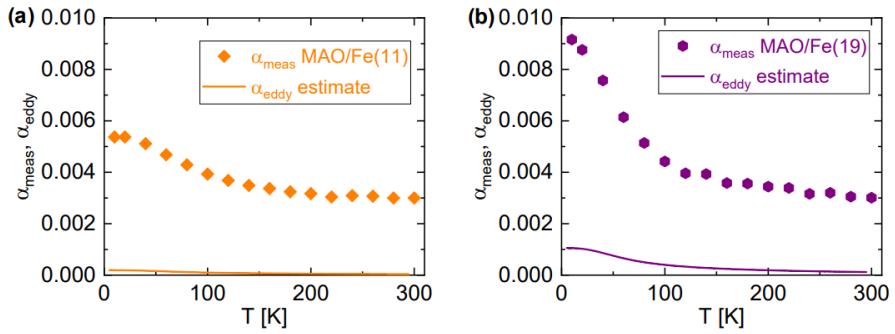

Figure 5.7: Temperature dependence of resistivity for MAO/Fe and MgO/Fe with different Fe film thicknesses. (b) Film thickness dependence of room-temperature resistivity. The dashed curve indicates the fit using a simplified Fuchs-Sondheimer model. (c) Ratio of residual resistivity to room-temperature resistivity versus film thickness. In (b) and (c), the closed symbols represent MAO/Fe and the open symbols represent MgO/Fe.

5.9 Temperature Dependence of Zero-Frequency Linewidth

The dependence of FMR linewidth $\Delta H_{\rm pp}$ on microwave excitation frequency f is fit with the simple linear equation,

$$\mu_0 \Delta H_{\rm pp} = \mu_0 \Delta H_0 + \frac{2}{\sqrt{3}} \frac{\alpha_{\rm meas}}{\gamma'} f. \tag{5.7}$$

Along with the measured Gilbert damping parameter $\alpha_{\rm meas}$, another key quantity extracted from the fit is the zero-frequency linewidth ΔH_0, which is typically attributed to broadening from magnetic inhomogeneity [14, 15]. As shown in Fig. 5.9, ΔH_0 increases with $\alpha_{\rm meas}$ at low temperatures in our in-plane FMR measurements.

If there are no interactions among different regions in an inhomogeneous film, the FMR spectrum at a fixed frequency is simply a superposition of local resonances with a distribution of resonance fields [15, 16]. In this case, the FMR linewidth extrapolated to $f = 0$ (ΔH_0 from Eqn. (5.7)) is expected to be constant with Gilbert damping (i.e., with temperature), as long as the magnetic inhomogeneity itself remains constant (which is a good approximation here, considering the weak temperature dependence of key properties of our epitaxial Fe films – see Section 5.11). However, when interactions in an

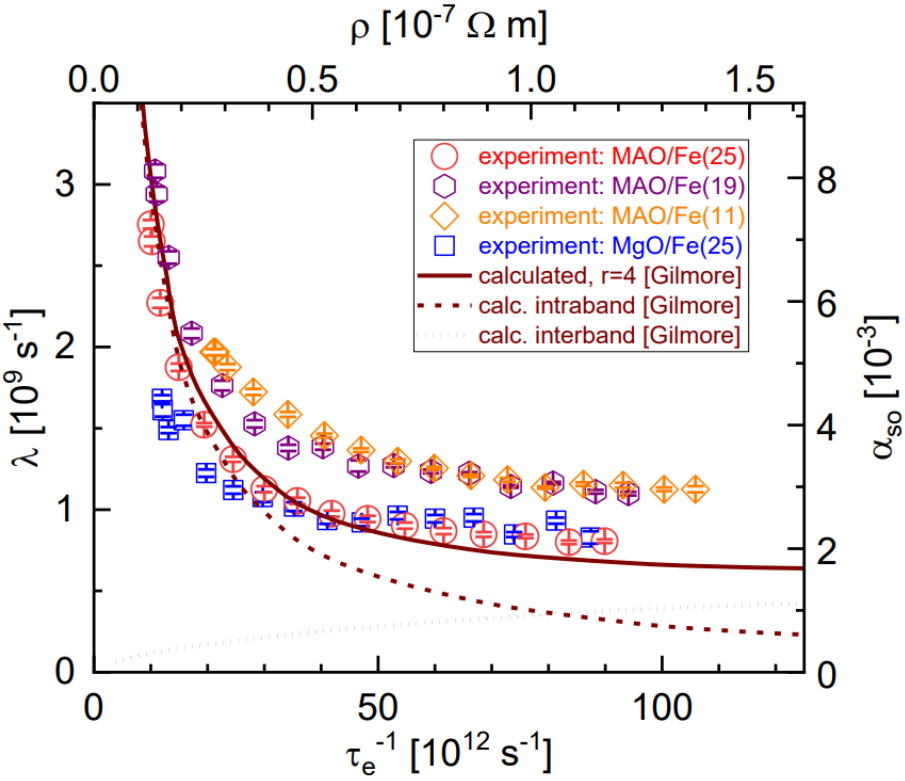

Figure 5.8: Comparison of experimentally derived and computationally predicted spin-orbit-induced magnetic relaxation rate (proportional to the Gilbert damping parameter α_{so}) plotted against electronic relaxation rate τ_e^{-1} (proportional to resistivity). The computational results are adapted from reference [12].

inhomogeneous film are not negligible, the FMR spectrum is no longer a simple superposition of local resonances [17]. We hypothesize that, in the presence of such interactions, ΔH_0 derived from the linear fit (Eqn. (5.7)) could vary with Gilbert damping and hence temperature, even while magnetic inhomogeneity remains invariant with temperature.

To test this hypothesis that ΔH_0 correlates with Gilbert damping, we have performed numerical calculations using the mean-field model developed by McMichael [17]. The inhomogeneous film is sectioned into blocks of lateral dimensions D and thickness t having different internal effective fields H_k. The distribution of H_k is Gaussian with standard deviation σ. The field experienced by each block is the sum of the external applied field $H_{ext}\hat{x}$, microwave field $\vec{h} = h_y\hat{y} + h_z\hat{z}$, and the field from interactions with all other blocks

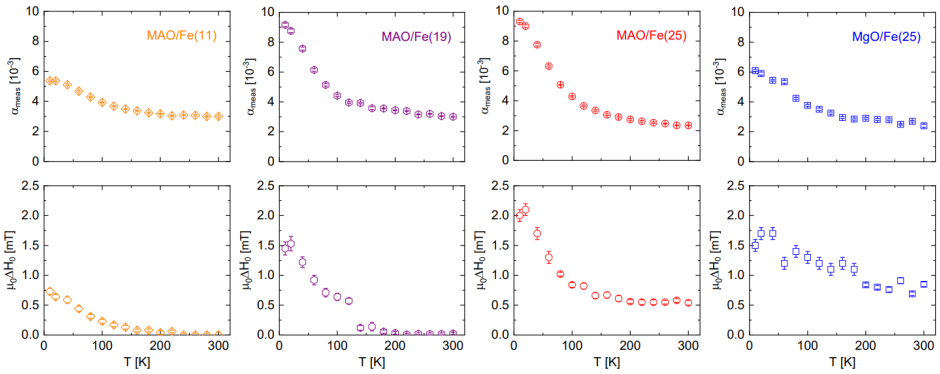

Figure 5.9: Comparison of experimentally derived and computationally predicted spin-orbit-induced magnetic relaxation rate λ (proportional to the Gilbert damping parameter α_{so}) plotted against electronic relaxation rate τ_{e}^{-1} (proportional to resistivity ρ). The computational results are adapted from reference [12].

that are lumped into the mean field $\vec{H}_{int}$ the form

$$\vec{H}_{int} = J_x M_s \hat{x} + \bar{J}_{yz} \overline{\overline{\chi}}_{eff} \vec{h}, \tag{5.8}$$

where J_x and $\bar{J}_{yz}$ are x and y-z portions of the interaction tensor $\bar{J}$ respectively. In Eqn. (5.8), $\overline{\overline{\chi}}_{eff}$ is the effective susceptibility tensor that relates the microwave field $\vec{h}$ and the average transverse magnetization over the whole film, $\langle \vec{m} \rangle = \bar{\chi}_{eff} \vec{h}$. It should be noted that $\overline{\overline{\chi}}_{eff}$ is dependent on the "intrinsic" Gilbert damping parameter α (which in general can be different from α_{meas}). We refer the reader to reference [17] for the expressions for $\overline{\overline{J}}$ and $\overline{\overline{\chi}}_{eff}$.

This modeling allows us to simulate FMR spectra by computing the absorptive component of $\overline{\overline{\chi}}_{eff}$ (i.e.,Im($\chi_{eff,yy}$)) (versus H_{res} at several fixed frequencies f, as shown in Fig. 5.10(a). Figure 5.10(b) shows examples of simulated f dependence of FMR spectral linewidth, carried out for results computed for an Fe film with $t = 19$ nm, $D = 16$ m and $\sigma = 2.5$mT and two different values of intrinsic damping, $\alpha = 0.004$ and 0.008. We fit the simulated linewidth versus frequency with Eqn. (5.7), omitting data at low frequencies where the film is not saturated in our experimental measurements (see Section 5.10). We thus extract ΔH_0 and α_{meas} for the modeling data in a similar way as in our experimental

measurements. The slight nonlinearity in linewidth versus frequency (Fig. 5.10(b)) is a key consequence of interactions in an inhomogeneous film, as reported in reference [17].

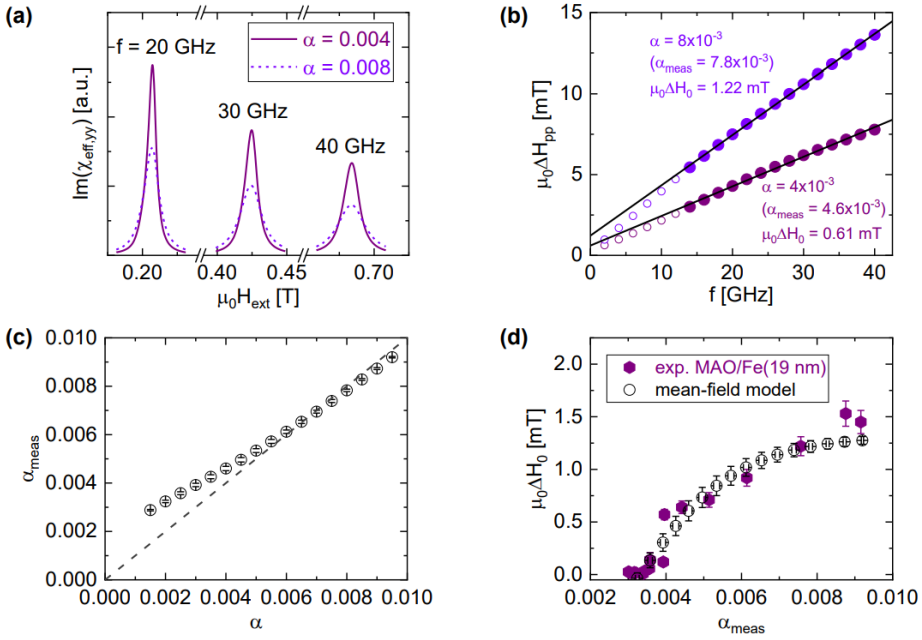

Figure 5.10: Examples of simulation results with McMichael's mean-field model [17] for inhomogeneous Fe thin films. The parameters used are: $t = 19$ nm, $D = 16$ m, $\sigma = 2.5$ mT, 0Ms = 2.1 T, $\gamma' = 29$ GHz/T, and exchange length $L_{\text{ex}} = 2.3$ nm. (a) Simulated FMR spectra of inhomogeneous films with intrinsic Gilbert damping parameters of $\alpha = 0.004$ and 0.008. (b) Frequency dependence of FMR linewidth for the same films as shown in (a). The linear fit is carried out for data at $f \geq 14$ GHz. Note that linewidth ΔH_{pp} plotted here is "peak-to-peak," consistent with the linewidth used for our experimental results, and that ΔH_{pp} is related to the FWHM linewidth of a simulated spectrum (e.g. (a)) via $\Delta H_{\text{pp}} = \Delta H_{\text{FWHM}}/\sqrt{3}$. (c) Relationship between α_{meas} obtained from the linear fit (e.g. (b)) and the intrinsic Gilbert damping parameter α. (d) Comparison of ΔH_0 versus α_{meas} for experimental and simulation results.

As seen in Fig. 5.10(c), α_{meas} derived from the linear fit (Fig. 5.10(b)) deviates from a by only 10 % particularly in the high damping regime (e.g., $\alpha > 0.005$), corresponding to measurements at low temperatures where conductivity-like Gilbert becomes dominant. We thus conclude that α_{meas} is indeed a good experimental measure of intrinsic Gilbert damping dominated by intraband scattering at low temperatures. Another key conclusion is that ΔH_0 from the linear fit (Eqn. (5.7)) scales with α_{meas} (or α) – in a way that is similar to our experimental observation – as shown in Fig. 5.10(d). In other words, our

modeling results indicate that the increased ΔH_0 at lower temperatures is due to increased conductivity-like Gilbert damping, rather than two-magnon scattering.

5.10 FMR Linewidths at Low Frequencies

In fitting the frequency dependence of FMR linewidth, we have excluded data from low frequencies to ensure the sample is uniformly magnetized. For example, at frequencies below ≈ 10 GHz, corresponding to in-plane fields below ≈ 100 mT, the Fe film is not completely saturated along the in-plane hard axis ([110] of Fe). The linewidth therefore becomes wider at these low frequencies, due to increased effective inhomogeneous broadening, as shown Fig. 5.11. This upturn of linewidth at low frequencies is similar to what has been observed for epitaxial CoFe [18, 19]. We note that when magnetized along its easy axis, epitaxial Fe exhibits higher resonance frequencies, thereby also preventing measurement at low frequencies.

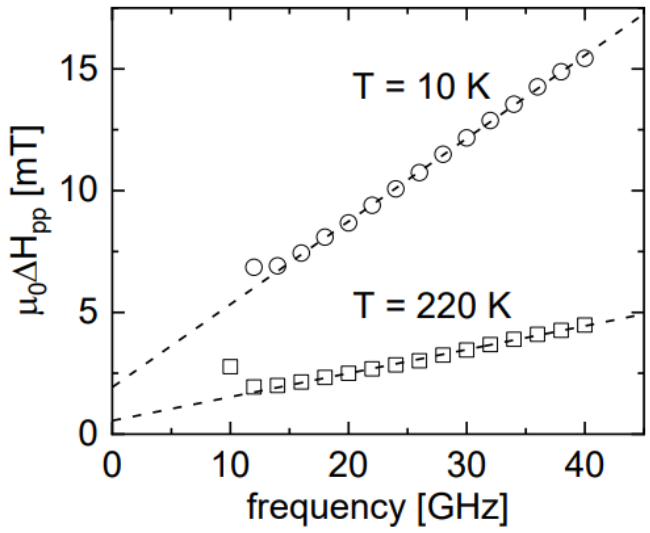

Figure 5.11: Frequency dependence of linewidth at $T = 10$ and 220 K for MAO/Fe (25 nm). The dotted lines indicate linear fits performed by excluding data < 16 GHz for $T = 10$ K and < 14 GHz for $T = 220$ K.

5.11 Temperature Dependence of Spectroscopic Parameters

Since the Curie temperature of bulk Fe is ≈ 1000 K, the static magnetic properties (or spectroscopic parameters extracted from broadband FMR measurements) of our > 10-nm-thick epitaxial Fe films are expected to be essentially constant over the temperature range studied here ($10 - 300$ K). Fig. 5.11 shows the three spectroscopic parameters – gyromagnetic ratio $\gamma^{'} = \gamma/(2\pi)$, effective magnetization M_{eff}, and in-plane cubic magnetocrystalline anisotropy field H_4–derived by simultaneously fitting the frequency f dependence of resonance field H_{res} along the inplane easy and hard axes of a MAO/Fe film (i.e., the same FMR measurements as shown in Fig. 5.4). Specifically, we use the Kittel equation of the form [20]:

$$f = \mu_0\gamma'\sqrt{(H_{res} + H_4\cos(4\phi))\left(H_{res} + \frac{1}{4}H_4(3 + \cos(4\phi)) + M_{eff}\right)}, \tag{5.9}$$

where $\phi = 0°$ corresponds to the hard axis and $\phi = 45°$ the easy axis. The results (e.g., Fig. 5.12) confirm that these key parameters for epitaxial Fe are indeed essentially temperature independent.

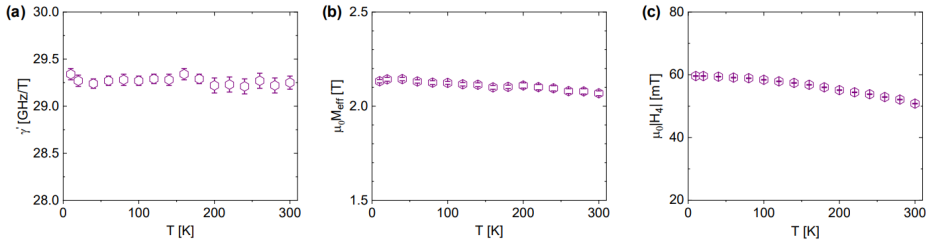

Figure 5.12: Temperature dependence of the (a) gyromagnetic ratio $\gamma^{'} = \gamma/(2\pi)$, (b) effective magnetization M_{eff}, and (c) in-plane cubic magnetocrystalline anisotropy field H_4 for for MAO/Fe(19 nm).

5.12 References

[1] R. C. O'Handley, *Magnetoelastic effects* (Wiley Interscience New York, 2000), pp. 218—-273.

[2] K. Gilmore, M. D. Stiles, J. Seib, D. Steiauf, and M. Fähnle, Phys. Rev. B **81**, 174414 (2010).

[3] S. Mankovsky, D. Ködderitzsch, G. Woltersdorf, and H. Ebert, Phys. Rev. B **87**, 014430 (2013).

[4] P. Giannozzi, S. Baroni, N. Bonini, M. Calandra, R. Car, C. Cavazzoni, D. Ceresoli, G. L. Chiarotti, M. Cococcioni, I. Dabo, et al., J. Condens. Matter Phys. **21**, 395502 (2009).

[5] J. P. Perdew, A. Ruzsinszky, G. I. Csonka, O. A. Vydrov, G. E. Scuseria, L. A. Constantin, X. Zhou, and K. Burke, Phys. Rev. Lett. **100**, 136406 (2008).

[6] D. Vanderbilt, Phys. Rev. B **41**, 7892 (1990).

[7] H. J. Monkhorst and J. D. Pack, Phys. Rev. B **13**, 5188 (1976).

[8] A. Dal Corso, Comput. Mater. Sci. **95**, 337 (2014).

[9] C. Scheck, L. Cheng, and W. E. Bailey, Appl. Phys. Lett. **88**, 252510 (2006).

[10] J. Lock, Br. J. Appl. Phys. **17**, 1645 (1966).

[11] K. Gilmore, Y. U. Idzerda, and M. D. Stiles, Phys. Rev. Lett. **99**, 027204 (2007).

[12] K. Gilmore, *Precession damping in itinerant ferromagnets,* Montana State University (2007).

[13] R. Schad, P. Beliën, G. Verbanck, C. Potter, K. Temst, V. Moshchalkov, and Y. Bruynseraede, J. Magn. Magn. Mater. **182**, 65 (1998).

[14] B. Heinrich, *Spin Relaxation in Magnetic Metallic Layers and Multilayers* (Springer Berlin Heidelberg, Berlin, Heidelberg, 2005), pp. 143–210.

[15] R. McMichael and P. Krivosik, IEEE Trans. Magn. **40**, 2 (2004).

[16] E. Schlömann, Phys. Rev. **182**, 632 (1969).

[17] R. D. McMichael, J. Appl. Phys. **103**, 07B114 (2008).

[18] A. J. Lee, J. T. Brangham, Y. Cheng, S. P. White, W. T. Ruane, B. D. Esser, D. W. McComb, P. C. Hammel, and F. Yang, Nat. Commun. **8**, 234 (2017).

[19] Y. Li, F. Zeng, S. S.-L. Zhang, H. Shin, H. Saglam, V. Karakas, O. Ozatay, J. E. Pearson, O. G. Heinonen, Y. Wu, et al., Phys. Rev. Lett. **122**, 117203 (2019).

[20] M. Farle, Rep. Prog. Phys. **61**, 755 (1998).

6 CONCLUSION

In this dissertation broadband FMR techniques were used to investigate the magnetization dynamics of different multilayer systems. These studies were aimed at determining a detailed description of the magnetic anisotropies, the exchange stiffness, and relaxation in these systems.

The FMR investigation of MnN/CoFeB exchange bias films with CoFeB thicknesses ranging from 5 to 20 nm revealed a strong contribution of a uniaxial anisotropy in addition to the unidirectional anisotropy associated with the exchange bias effect. Angle dependent FMR measurements further revealed that the easy directions of both anisotropies are very close to each other. The linewidth data also showed contributions with unidirectional and unaxial symmetry. The influence of the reduced symmetry on the damping in these systems are very critical for spintronic applications. The FMR investigation of Co/Ni multilayers indicated a strong higher order contribution to the PMA. Polar angle dependent measurement revealed the presence of canted states for 12 and 25 repetitions of Co/Ni bilayers. Fitting of the polar angle dependent data indicates that the macrospin approximation is not sufficient to explain the canted states seen in these Co/Ni bilayers. Linewidth data revealed a strong interfacial contribution to damping through spin pumping. Thickness dependent FMR data enabled us to estimate the exchange stiffness constant A. Low temperature FMR investigation of Fe grown on MAO and MgO substrates resulted in the first experimental observation of conductivity-like Gilbert damping in Fe. Furthermore, the FMR results confirmed that disorder can be beneficial for low temperature applications that require low damping.

REFERENCES

[1] L. Landau and E. Lifshitz, Phys. Z. Sowjetunion **8**, 101 (1935).

[2] T. L. Gilbert, IEEE Trans. Magn. **40**, 3443 (2004).

[3] J. H. Griffiths, Nature **158**, 670 (1946).

[4] C. Kittel, Phys. Rev. **71**, 270 (1947).

[5] C. L. Dennis, R. P. Borges, L. D. Buda, U. Ebels, J. F. Gregg, M. Hehn, E. Jouguelet, K. Ounadjela, I. Petej, I. L. Prejbeanu, et al., J. Condens. Matter Phys. **14**, R1175 (2002).

[6] G. S. Abo, Y.-K. Hong, J. Park, J. Lee, W. Lee, and B.-C. Choi, IEEE Trans. Magn. **49**, 4937 (2013).

[7] C. K. Mewes and T. Mewes, *Relaxation in magnetic materials for spintronics* (Pan Stanford Publishing Singapore, 2015), pp. 71–96.

[8] J. Smit and H. Beljers, Phillips Res. Rep. **10**, 113 (1955).

[9] P. G. Barreto, M. A. Sousa, F. Pelegrini, W. Alayo, F. J. Litterst, and E. Baggio-Saitovitch, Appl. Phys. Lett. **104**, 202403 (2014).

[10] C. Kittel, Phys. Rev. **110**, 1295 (1958).

[11] M. H. Seavey and P. E. Tannenwald, Phys. Rev. Lett. **1**, 168 (1958).

[12] R. M. Bozorth, *Ferromagnetism* (1993).

[13] H. Draaisma, W. de Jonge, and F. den Broeder, J. Magn. Magn. Mater. **66**, 351 (1987).

[14] W. H. Meiklejohn and C. P. Bean, Phys. Rev. **102**, 1413 (1956).

[15] W. H. Meiklejohn and C. P. Bean, Phys. Rev. **105**, 904 (1957).

[16] J. Nogués and I. K. Schuller, J. Magn. Magn. Mater. **192**, 203 (1999).

[17] H. Suhl, Phys. Rev. **97**, 555 (1955).

[18] Y. Li and W. E. Bailey, Phys. Rev. Lett. **116**, 117602 (2016).

[19] A. Kumar, F. Pan, S. Husain, S. Akansel, R. Brucas, L. Bergqvist, S. Chaudhary, and P. Svedlindh, Phys. Rev. B **96**, 224425 (2017).

[20] R. Arias and D. L. Mills, Phys. Rev. B **60**, 7395 (1999).

[21] R. Arias and D. Mills, J. Appl. Phys.s **87**, 5455 (2000).

[22] A. Rai, M. Dunz, A. Sapkota, P. Zilske, J. B. Mohammadi, M. Meinert, C. Mewes, and T. Mewes, J. Magn. Magn. Mater. **485**, 374 (2019).

[23] M. A. W. Schoen, J. M. Shaw, H. T. Nembach, M. Weiler, and T. J. Silva, Phys. Rev. B **92**, 184417 (2015).

[24] C. J. Oates, F. Y. Ogrin, S. L. Lee, P. C. Riedi, G. M. Smith, and T. Thomson, J. Appl. Phys. **91**, 1417 (2002).

[25] C. P. Poole (1996).

[26] A. G. Gurevich, *Ferrites at microwave frequencies* (Consultants Bureau, 1963).

[27] S. V. Von Sovskii, *Ferromagnetic resonance: the phenomenon of resonant absorption of a high-frequency magnetic field in ferromagnetic substances* (Elsevier, 2016).

[28] W. C. Michels and N. L. Curtis, Rev. Sci. Instrum. **12**, 444 (1941).

[29] R. Wolfson, Am. J. Phys. **59**, 569 (1991).

[30] J. H. Scofield, Am. J. Phys. **62**, 129 (1994).

[31] T. Mewes, C. K. A. Mewes, E. Nazaretski, J. Kim, K. C. Fong, Y. Obukhov, D. V. Pelekhov, P. E. Wigen, and P. C. Hammel, J. Appl. Phys. **102**, 033911 (2007).

[32] L. Kraus and G. Ababei, Acta Phys. Pol. A **127**, 359 (2015).

[33] S. Dushenko, Y. Ando, T. Shinjo, and M. Shiraishi, J. Appl. Phys. **126**, 203904 (2019).

[34] S. Mangin, D. Ravelosona, J. Katine, M. Carey, B. Terris, and E. E. Fullerton, Nat. Mater. **5**, 210 (2006).

[35] X. Li, Z. Zhang, Q. Jin, and Y. Liu, Appl. Phys. Lett. **92**, 122502 (2008).

[36] S. Mangin, Y. Henry, D. Ravelosona, J. Katine, and E. E. Fullerton, Appl. Phys. Lett. **94**, 012502 (2009).

[37] W. H. Rippard, A. M. Deac, M. R. Pufall, J. M. Shaw, M. W. Keller, S. E. Russek, G. E. Bauer, and C. Serpico, Phys. Rev. B **81**, 014426 (2010).

[38] A. Rai, A. Sapkota, A. Pokhrel, M. Li, M. De Graef, C. Mewes, V. Sokalski, and T. Mewes, Phys. Rev. B **102**, 174421 (2020).

[39] B. Khodadadi, A. Rai, A. Sapkota, A. Srivastava, B. Nepal, Y. Lim, D. A. Smith, C. Mewes, S. Budhathoki, A. J. Hauser, et al., Phys. Rev. Lett. **124**, 157201 (2020).

[40] P. Zilske, D. Graulich, M. Dunz, and M. Meinert, Appl. Phys. Lett. **110**, 192402 (2017).

[41] K. Lee, J. J. Sapan, S. H. Kang, and E. E. Fullerton, J. Appl. Phys. **109**, 123910 (2011).

[42] R. Matsumoto, H. Arai, S. Yuasa, and H. Imamura, Appl. Phys. Express **8**, 063007 (2015).

[43] A. Sapkota, A. Rai, A. Pokhrel, J. B. Mohammadi, M. Li, D. Lau, M. De Graef, V. Sokalski, T. Mewes, and C. Mewes, J. Appl. Phys. **128**, 073910 (2020).

[44] D. A. Smith, , Y. Lim, T. Q. Hartnett, A. Sapkota, A. Srivastava, C. Mewes, Z. Jiang, M. Clavel, M. K. Hudait, et al., Phys. Rev. Appl. **14**, 034042 (2020).

[45] S. Wu, D. A. Smith, P. Nakarmi, A. Rai, M. Clavel, M. K. Hudait, J. Zhao, M. F. Michel, C. Mewes, T. Mewes, et al., arXiv:2109.03684 (2021).

[46] R. Cheng, M. Li, A. Sapkota, A. Rai, A. Pokhrel, T. Mewes, C. Mewes, D. Xiao, M. De Graef, and V. Sokalski, Phys. Rev. B **99**, 184412 (2019).

[47] M. Li, A. Rai, A. Pokhrel, A. Sapkota, C. Mewes, T. Mewes, M. D. Graef, and V. Sokalski, Appl. Phys. Lett. **117**, 112403 (2020).

[48] S. Mansur, A. Rai, R. A. Holler, T. Mewes, and Y. Bao, J. Magn. Magn. Mater. **515**, 167265 (2020).